UNIVERSITÀ
DEGLI STUDI
DI PADOVA

Università degli Studi di Padova
Dipartimento di Scienze Chimiche

SCUOLA DI DOTTORATO DI RICERCA IN SCIENZA E INGEGNERIA DEI MATERIALI
CICLO XXVII

LIQUID CRYSTALS OF BENT-SHAPED MOLECULES: MODELLING THEIR UNCONVENTIONAL PROPERTIES AND PHASE BEHAVIOUR

Direttore della Scuola : Ch.mo Prof. Gaetano Granozzi

Supervisore : Prof. Alberta Ferrarini

Dottorando : Cristina Greco

Contents

Abstract

The fascinating behaviour of liquid crystals is a consequence of the shape anisotropy of their constituent molecules. Conventional mesogens have a rod-like or disc-like shape: their simplest and most common mode of liquid crystalline organization is the nematic phase (N), where the molecules preferentially align along a common axis, called the director **n**. Recently a new class of thermotropic liquid crystals has emerged, made of achiral molecules with a bent (banana-like) shape. From a chemical point of view, two molecular architectures can be distinguished: bent-core compounds and odd liquid crystal dimers. The first are characterized by a fairly rigid aromatic core and terminal flexible chains; the second are made of two terminal mesogenic units connected by a flexible spacer having an odd number of atoms. Liquid crystals of bent molecules are unconventional materials, in that they exhibit remarkable physical properties and new phase organizations, different from those of conventional liquid crystals.

In particular, unusually low values of the bend elastic constant K_{33} and relatively high flexoelectric couplings were measured for both bent-core compounds and odd liquid crystal dimers in their N phase. The origin of this behaviour is not clear and different hypotheses have been proposed. Its understanding is important both for fundamental reasons and also for applications, including the design of materials optimized for new display modes or for electromechanical energy conversion.

For what regards the phase organization, there is currently considerable interest for a new kind of nematic phase, which has been discovered only a few years ago in odd liquid crystals dimers, at temperatures below the common N phase. ^{2}H-NMR experiments, which provide information on the molecular order, demonstrated that this phase is chiral, despite the molecules being achiral, and a twist-bend nematic organization was proposed (N_{TB}). This is characterized by a modulated director **n** which precesses in space around an axis forming a conical helix, with conical angle θ_0 and pitch p, thus featuring spontaneous local bend distorsions and local polar order. This discovery has given rise to an intense debate, in relation to both the phase structure and origin. Either flexoelectric couplings or an elastic instability have been proposed as possible driving mechanisms of the N_{TB}-N transition. Segregation of chiral molecular

conformations has also been invoked to explain the phase chirality. Another aspect which needs clarification is the strong sensitivity of the N_{TB} phase formation to small changes in the molecular structure.

In this thesis the phase and material properties of liquid crystals of bent molecules have been investigated using theoretical and computational methods, with the aim to establish a connection between the macroscopic behaviour and the molecular structure. This is a challenging task: computational methods such as quantum mechanical calculations and atomistic Molecular Dynamics simulations are in many cases insufficient and alternatives routes must be found. In this work different methods have been used and developed, suitable to cover or connect the different length scales involved.

(***i***) To investigate the molecular origin of the N_{TB}-N phase transition, and to obtain qualitative information on the structure of the N_{TB} phase, a molecular field model was developed, by generalizing the Maier-Saupe theory to apolar rigid V-shaped molecules in an N or N_{TB} environment. Our findings show that the key molecular feature at the origin of the N_{TB} phase is the bent molecular shape, indicating that flexoelectric couplings are not essential. We showed that the phase behaviour is extremely sensitive to the molecular bend angle, with the N_{TB}-N phase transition occurring only for a limited range of values. This result allowed us to elucidate the experimentally observed sensitivity of the N_{TB} phase formation to small changes in the molecular structure. The model also allowed us to make some general predictions about the elastic behaviour and to clarify the relationship between the N_{TB}-N phase transition and the elastic properties of the nematic phase, showing that transition is accompanied by softening of the bend elastic mode in the N phase.

To get insight into the molecular organization in the N_{TB} phase, Molecular Dynamics simulations of rigid, apolar, achiral, purely repulsive bent-shaped particles were performed. In this way we could explicitly take into account the possible effects of intermolecular correlations and further check the relationship between the molecular features and the phase behaviour. Our results are in line with the formation of an N_{TB} organization, and, given the molecular model used, point to the crucial role of the bent shape, in agreement with the conclusions of our generalized Maier-Saupe model. In particular, the observation of a chiral organization in a system of achiral rigid particles

clearly indicates that conformational chirality is not essential for the formation of the N_{TB} organization.

(***ii***) An Integrated Methodology (IM), which couples an atomistic representation of the molecular structure with a molecular field model of orientational order, was set up to obtain quantitative information about the phase and material properties, and their dependence on the chemical structure. In this context quantum mechanical DFT calculations were performed to obtain accurate values of the relevant molecular structural parameters (geometry, torsional potentials and atomic charges) and Monte Carlo conformational sampling was used to take into account the molecular flexibility. Much of the work has been dedicated to understanding the elastic and flexoelectric behaviour of bent-core compounds and liquid crystals dimers in their nematic (N) phase. Collaboration with experimental groups allowed us to validate the methodology on a large number of systems with different molecular structures. Very good agreement was obtained between our predictions and the experimental findings, showing the sensitivity of our methodology to details of the chemical structure and thus its usefulness as a tool for materials design for applications. The variety of chemical structures investigated allowed us to build a library of molecular parameters for the most common mesogenic groups, which can be reused and incremented in the future.

Modelling allowed us to identify the molecular origin of the small bend elastic constant K_{33} exhibited by nematics of bent molecules and also to explain apparent exceptions to this behaviour. In particular we showed that the main parameter governing the elasticity of these systems is the molecular bend angle.

The IM approach appears promising also for the development of a molecular-based understanding of flexoelectricity in liquid crystals. We could identify some general features in the flexoelectric properties of bent-core compounds and connect them to the molecular structure, offering a consistent interpretation of different experimental results.

The molecular field model at the basis of the IM methodology has been extended to describe the orientational order in the N_{TB} phase. In this way it was possible to analyse the detailed information provided by ^{2}H-NMR experiments. By combining the theoretical predictions with the experimental data we could obtain quantitative estimates of the pitch and conical angle of the N_{TB} phase on the basis of the molecular structure. We also investigated the origin of the strong enantiotopic discrimination observed in the

N_{TB} phase. Our results indicate that this is not related to presence of chiral molecular conformations, but it is a direct consequence of the high chirality of the N_{TB} environment, resulting from its extremely small pitch.

The thesis is organized as follows. The *Introduction* is intended as an overview on liquid crystalline order (Chapter 1) and on the unconventional phase and material properties of liquid crystals of bent-shaped molecules (Chapter 2). *Part I* (Chapter 3) presents the generalized Maier-Saupe model and its results. *Part II* (Chapter 4) is devoted to the Molecular Dynamics simulations. *Part III* illustrates the IM methodology (Chapter 5), its applications to the investigation of phase and materials properties of bent-shape molecules in their nematic phase (Chapters 6-8), and finally its extension to the twist-bend nematic phase (Chapter 9).

Sommario

L'affascinante comportamento dei cristalli liquidi è una conseguenza della forma anisotropa delle molecole che li costituiscono. I mesogeni convenzionali hanno la forma di una bacchetta o di un disco: la loro più semplice e più comune organizzazione liquido-cristallina è la fase nematica (N), in cui le molecole sono preferenzialmente allineate lungo un asse, chiamato direttore **n**. Recentemente è emersa una nuova classe di cristalli liquidi termotropici, costituiti da molecole non chirali aventi una forma curva ("bent"), come quella di una banana. Dal punto di vista chimico, si possono distinguere due architetture molecolari: i composti "bent-core" e i "dimeri dispari". I primi sono caratterizzati da un cuore aromatico relativamente rigido e catene terminali flessibili; i secondi sono costituiti da due unità mesogeniche terminali connesse da uno spaziatore flessibile avente un numero dispari di atomi. I cristalli liquidi di molecole curve sono materiali non convenzionali, in quanto presentano proprietà fisiche notevoli e nuove organizzazioni di fase, diverse da quelle dei cristalli liquidi convenzionali.

In particolare, valori insolitamente piccoli della costante elastica di bend K_{33} e accoppiamenti flessoelettrici relativamente grandi sono stati misurati per la fase nematica (N) sia di composti bent-core che di dimeri dispari. L'origine di questo comportamento non è chiara e sono state avanzate varie ipotesi. La sua comprensione è importante sia da un punto di vista fondamentale che ai fini delle applicazioni, tra cui la progettazione di materiali ottimizzati per nuovi display o per la conversione elettromeccanica dell'energia.

Per quanto riguarda l'organizzazione di fase, c'è attualmente grande interesse per un nuovo tipo di fase nematica, scoperta solo qualche anno fa in cristalli liquidi formati da dimeri dispari, a temperature inferiori a quelle della comune fase N. Esperimenti ^{2}H-NMR, fornendo informazioni sull'ordine molecolare, hanno dimostrato che questa fase è chirale, nonostante sia costituita da molecole non chirali, ed è stata proposto che essa abbia un'organizzazione di tipo nematico "twist-bend" (N_{TB}). Nella fase N_{TB} il direttore **n** non è uniforme ma "modulato": esso precede nello spazio attorno a un'asse, formando un'elica con angolo di cono θ_0 ripetto all'asse e passo p. Localmente, questa struttura è caratterizzata dalla presenza di deformazioni di bend spontanee e da ordine polare. La

scoperta di questa fase ha dato origine a un intenso dibattito, in merito sia alla sua struttura che alla sua origine. È stato suggerito che la transizione N_{TB}-N possa essere guidata da accoppiamenti flessoelettrici o da una instabilità elastica. È stata anche avanzata l'idea che la chiralità della fase derivi dalla segregazione di conformazioni molecolari chirali. La formazione della fase N_{TB} appare estremamente sensibile a piccoli cambiamenti della struttura molecolare: questo è un altro aspetto che necessita spiegazione.

In questa tesi le proprietà di fase e del materiale di cristalli liquidi costituiti da molecole curve sono state indagate mediante metodi teorici e computazionali, allo scopo di stabilire una relazione tra il comportamento macroscopico e la struttura molecolare. Questo è un obiettivo non banale: metodi computazionali come i calcoli quantomeccanici e le simulazioni di Dinamica Molecolare atomistiche sono in molti casi insufficienti ed è necessario trovare strade alternative. In questo lavoro di tesi sono stati usati e sviluppati vari metodi, adatti a coprire o connettere le diverse scale di lunghezza coinvolte.

(***i***) Per indagare l'origine molecolare della transizione di fase N_{TB}-N, e per ottenere informazioni qualitative sulla struttura della fase N_{TB}, è stato sviluppato un modello di campo molecolare, generalizzando la teoria di Maier-Saupe a molecole rigide non-polari a forma di "V", in un intorno N o N_{TB}. I risultati ottenuti dimostrano che la forma curva delle molecole è la caratteristica essenziale per spiegare l'origine della fase N_{TB}, indicando che gli accoppiamenti flessoelettrici non sono necessari. Abbiamo evidenziato come il comportamento di fase sia estremamente sensibile all'angolo molecolare ("angolo di bend"): la transizione N_{TB}-N avviene solo in corrispondenza di un intervallo limitato di valori. Questo risultato ci ha permesso di chiarire l'osservazione sperimentale per cui la formazione della fase N_{TB} è particolarmente sensibile a cambiamenti della struttura molecolare. Il modello ci ha permesso anche di fare alcune predizioni generali relativamente al comportamento elastico e di chiarire la relazione tra la transizione di fase N_{TB}-N e le proprietà elastiche della fase nematica, mostrando che la transizione è accompagnata da una progressiva riduzione della costante elastica di bend nella fase N.

Per caratterizzare l'organizzazione molecolare nella fase N_{TB}, sono state condotte simulazioni di Dinamica Molecolare di particelle curve, rigide, non polari, non chirali e

con interazioni puramente repulsive. Abbiamo così potuto tenere conto esplicitamente dei possibili effetti delle correlazioni intermolecolari e verificare ulteriormente la relazione tra le caratteristiche molecolari e il comportameto di fase. I risultati ottenuti sono coerenti con la formazione di un'organizzazione N_{TB} e, dato il modello molecolare usato, indicano il ruolo cruciale della forma molecolare curva, in accordo con le conclusioni del modello di Maier-Saupe generalizzato. In particolare, l'osservazione di un'organizzazione chirale in un sistema di particelle rigide non chirali indica chiaramente che la chiralità conformazionale non è essenziale per la formazione dell'organizzazione N_{TB}.

(***ii***) È stata messa a punto una Metodologia Integrata (IM), che combina una rappresentazione atomistica della struttura molecolare con un modello di campo molecolare per l'ordine orientazionale, allo scopo di ottenere informazioni quantitative sulle proprietà di fase e del materiale, e sulla loro dipendenza dalla struttura chimica. In questo contesto sono stati condotti calcoli quantomeccanici DFT per ottenere valori accurati dei parametri strutturali rilevanti della molecola (geometria, potenziali torsionali e cariche atomiche); tecniche di campionamento conformazionale Monte Carlo sono state utilizzate per tenere conto della flessibilità molecolare.

La maggior parte del lavoro di ricerca è stato dedicato alla comprensione del comportamento elastico e flessoelettrico della fase nematica (N) di composti bent-core e di dimeri liquido-cristallini. La collaborazione con gruppi di ricerca sperimentali ci ha permesso di validare la metodologia rispetto a una varietà di sistemi con diversa struttura molecolare. Il buon accordo tra le nostre predizioni e i risultati sperimentali dimostra che la metodologia è sensibile ai dettagli della struttura chimica, e rappresenta quindi un utile strumento per il design di materiali per fini applicativi. La varietà di strutture chimiche investigate ci ha permesso di costruire una libreria di parametri molecolari per i più comuni gruppi mesogenici che potrà essere riutilizzata e ampliata in futuro.

L'attività di modellizzazione ci ha permessso di identificare l'origine molecolare della piccola costante elastica di bend K_{33} mostrata da cristalli liquidi nematici di molecole curve e anche di spiegare apparenti eccezioni questo comportamento. In particolare abbiamo dimostrato che l'angolo di bend molecolare è la principale caratteristica che determina l'elasticità di questi sistemi.

L’approccio IM appare promettente anche ai fini dello sviluppo di una comprensione su base molecolare della flessoelettricità nei cristalli liquidi. Abbiamo potuto identificare alcune caratteristiche generali nelle proprietà flessoelettriche di composti bent-core e collegarle alla struttura molecolare, e questo ci ha permesso di fornire un’interpretazione coerente di vari risultati sperimentali.
Il modello di campo molecolare alla base della metodologia IM è stato esteso per descrivere l’ordine orientazionale nella fase N_{TB}. In questo modo è stato possibile analizzare le informazioni dettagliate fornite dagli esperimenti ^{2}H-NMR. Combinando le predizioni teoriche con i dati sperimentali è stato possibile ottenere stime quantitative del passo e dell’angolo di cono della fase N_{TB} sulla base della struttura molecolare. Abbiamo anche esaminato l’origine della grande discriminazione enantiotopica osservata nella fase N_{TB}. I risultati ottenuti indicano che essa non è dovuta alla presenza di conformazioni molecolari chirali, ma è una conseguenza diretta dell’elevata chiralità dell’intorno N_{TB}, derivante dal suo passo estremamente piccolo.

La tesi è organizzata come segue. L’*Introduzione* è da intendersi come una panoramica sull’ordine in fasi di cristallo liquido (Capitolo 1) e sulle proprietà non convenzionali, di fase e del materiale, di cristalli liquidi costituiti da molecole curve (Capitolo 2). La *Parte I* (Capitolo 3) presenta il modello di Maier-Saupe generalizzato e i suoi risultati. La *Parte II* (Capitolo 4) è dedicata alle simulazioni di Dinamica Molecolare. La *Parte III* illustra la metodologia IM (Capitolo 5), le sue applicazioni allo studio delle proprietà di fase e del materiale della fase nematica di molecole curve (Capitoli 6-8), e infine la sua estensione alla fase nematica twist-bend (Capitolo 9).

Introduction

Chapter 1

Liquid crystals: an overview

1.1 Conventional liquid crystal phases

Liquid crystals (LCs) are intermediate phases (*mesophases*) between isotropic liquids (I) and crystalline solids (Cr): they are fluid, like liquids, but at the same time they exhibit anisotropic physical properties, like crystals [1,2]. Liquid crystals are divided into two main groups, according to the driving force for their formation: *thermotropic* LCs are formed from the isotropic liquid on decreasing the temperature, *lyotropic* LCs are formed from solutions on increasing the concentration. The systems investigated in this thesis belong to the first group.

The macroscopic properties of LCs are a consequence of the properties and organization of their constituent molecules (*mesogens*). In order to form a LC phase, molecules must have an anisotropic shape, like that of an elongated rod (*calamitic* LCs) or of a flat disc (*discotic* LCs) (Figure 1.1). From a chemical point of view, this is obtained by introducing in the molecular structure a fairly rigid anisometric unit (*mesogenic* group), usually made by aromatic rings; in order to promote the formation of a fluid phase,

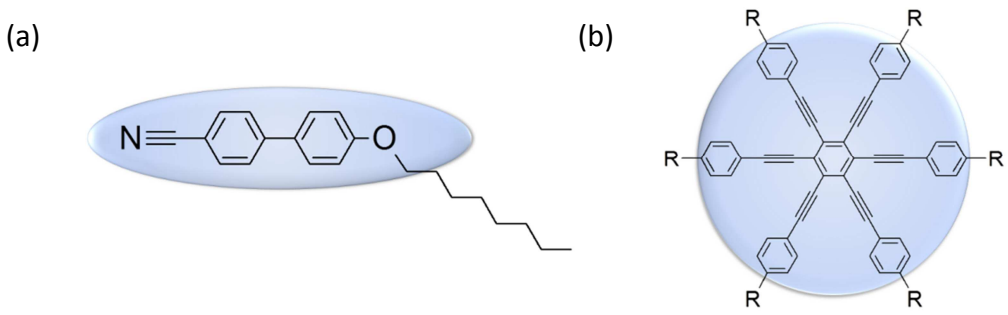

Figure 1.1. Molecular structure of (a) 8OCB, a rod-like mesogen, (b) a discotic mesogen.

instead of a crystal, flexible units, such as alkyl chains, are attached to the mesogenic groups [3]. The anisotropy of intermolecular interactions promotes mutual alignment of the molecules along a common direction, called the director and indicated by the unit vector **n**. Liquid crystals phases are generally apolar, *i.e.* the directions **n** and –**n** are equivalent. Orientational order is the distinctive feature defining LC phases; mesophases with only this kind of order are called *nematics*; if, in addition, some degree of positional order is present, the phases are classified as *smectics*.

Figure 1.2 shows the most important LC phases formed by achiral, rod-like mesogens [1,2]. In all these phases the director **n** is uniform, *i.e.* its orientation does not change in space. The simplest, most symmetric organization is the uniaxial nematic phase (N), of point group symmetry $D_{\infty h}$, with the C_∞ symmetry axis parallel to **n** (Figure 1.2(a)). Macroscopically the C_∞ axis is the main principal direction common to all second-rank tensor physical properties (*macroscopic principal director* or *optical axis*).

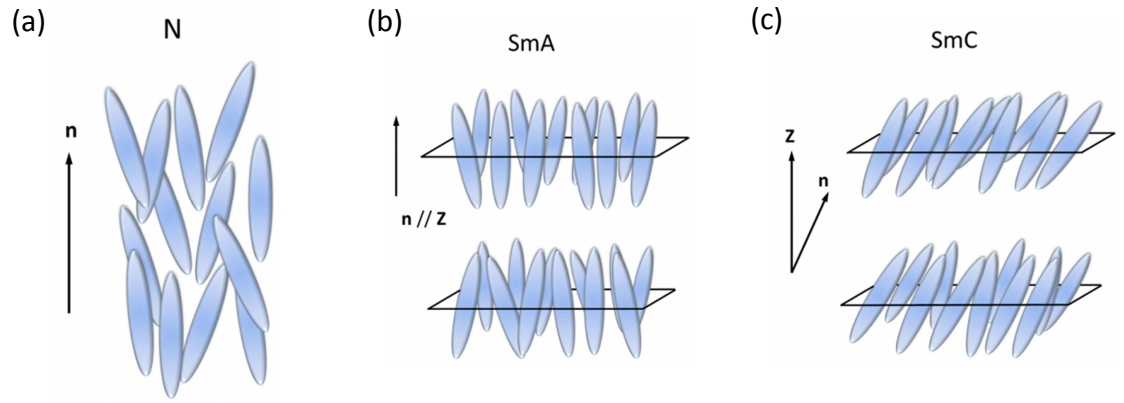

Figure 1.2. Examples of liquid crystal phases made of achiral molecules: (a) nematic (N), (b) smectic A (SmA), (c) smectic C (SmC). **n** is the director and **Z** is the normal to the smectic layers.

The smectic A (SmA) and smectic C (SmC) phases possess long-range translational order in one dimension: the molecular centres of mass are arranged in layers, with no correlations between the molecular positions inside the layers. In the SmA phase (Figure 1.2(b)) the layer normal (**Z**) and the director **n** are parallel to each other and the phase has uniaxial $D_{\infty h}$ symmetry, with C_∞ // **Z** . In the SmC phase (Figure 1.2(c)) the director **n** is tilted with respect to the layer normal **Z**, and the phase has C_{2h} point symmetry. The symmetry plane coincides with the plane defined by **Z** and **n** (the *tilt*

plane) and the twofold symmetry axis is perpendicular to this plane. The C_2 axis is the only principal axis common to all second rank tensor properties; the other two principal directions must lie on the symmetry plane, but their orientation can be different for different properties.

Chirality at the molecular level gives rise to chiral phases, where the director **n** is not uniform, but spatially modulated [1,2,4]. The most common organization of chiral rod-like molecules is the cholesteric phase (Ch, Figure 1.3(a)). The Ch phase is a nematic phase where the director **n** rotates about an axis **Z**, the helix axis, remaining always perpendicular to **Z**. The rotation angle is given by $\phi = 2\pi Z / p$ where p is the helical pitch. By convention, $p < 0$ for a left-handed helix and $p > 0$ for a right-handed helix. The cholesteric phase has global D_∞ symmetry, with the C_∞ axis parallel to the helix axis, and local D_2 symmetry; of the three twofold symmetry axes, one is parallel to **n**, another to the helix axis **Z** and the third is perpendicular to both **n** and **Z**. The helical pitch p is much larger than the molecular dimensions, with typical values in the range 100 nm–1μm, so that the local biaxiality is very small [1]. The smectic C* phase (SmC*, Figure 1.3(b)) is a chiral variant of SmC: the director **n** precesses around the layer normal **Z**, forming a conical helix with the helix axis parallel to **Z**. Because of this chiral arrangement, the local symmetry is reduced to C_2, with the twofold axis perpendicular to the tilt plane. The global symmetry is D_∞ [5].

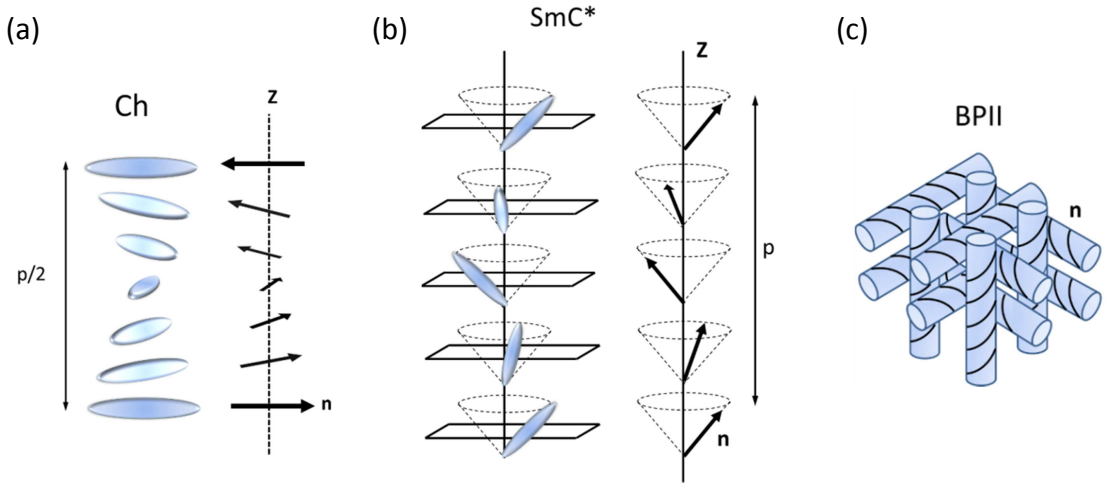

Figure 1.3. Examples of liquid crystal phases made of chiral molecules: (a) cholesteric (Ch), (b) chiral smectic C (SmC*), (c) blue phase II (BPII). **n** represents the director, **Z** the helix axis and p the helical pitch.

Blue phases are LC phases spatially periodic in three dimensions: at variance with crystals, the translational order is not that of the constituent molecules, which are positionally disordered, but arises from a 3D network of defects. Blue phases are usually stable in a very narrow temperature range between the isotropic and cholesteric phases, but recently blue phases with a wide temperature range have been found (see next Chapter). Figure 1.3(c) shows the structure of one kind of blue phase (BPII): this is described as a regular 3D assembly of so-called double-twist cylinders.
A summary of the phases described above and of their symmetry is reported in Table 1.1.

Liquid Crystal Phase	**Symmetry**
Nematic (N)	$D_{\infty h} \times T(3)$
Cholesteric (Ch)	$D_{\infty} \times T(3)$ $[D_2]$
Smectic A (SmA)	$D_{\infty h} \times T(2)$
Smectic C (SmC)	$C_{2h} \times T(2)$
Chiral Smectic C (SmC*)	$D_{\infty} \times T(2)$ $[C_2]$
Blue Phase II (BPII)	O^2

Table 1.1. Common liquid crystals phases and their symmetry. T(*n*) indicates continuous translational symmetry in *n* dimension. For helical phases (Ch and SmC*) both the global and the local point groups are indicated (the latter between square brackets) [2,4,5].

1.2 Orientational order parameters

The orientational order characterizing the liquid crystalline state is quantified by a set of order parameters. The latter can be defined starting from two different, though related, perspectives [1,6]: (i) considering the anisotropy of the molecular orientational distribution function (microscopic approach); (ii) looking at the anisotropy of tensorial physical properties of the material (macroscopic approach).

1.2.1 Microscopic approach

1.2.1.1 Definition of molecular order parameters

From a molecular point of view, order parameters are defined as moments of the single particle orientational distribution function $p(\Omega)$, which gives the probability density of

finding a molecule in a given orientation between Ω and Ω+$d\Omega$, and is normalized as [7,8]:

$$\int p(\Omega)d\Omega = 1 \tag{1.1}$$

The nth moments of $p(\Omega)$ are called order parameters of rank n. The number of non-vanishing, independent order parameters is determined by the molecular and phase symmetry. For example, for a rigid rod-like molecule (uniaxial $D_{\infty h}$ symmetry) in a conventional nematic N phase (uniaxial $D_{\infty h}$ symmetry), the distribution function depends only on the angle β between the rod long-axis and the director **n**: $p = p(\beta)$ (see Figure 1.4(a)). Moreover, since the phase is non-polar, only even moments of $p(\beta)$ are different from zero.

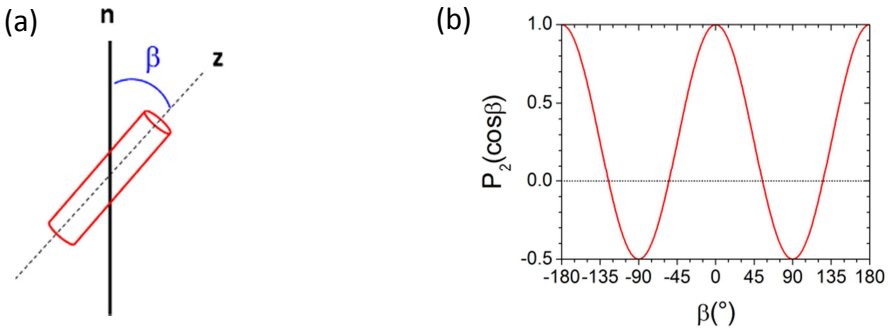

Figure 1.4. (a) Orientation of a rod-like molecule in a uniaxial nematic phase. **n** is the nematic director and z is the rod long-axis. (b) The second Legendre polynomial $P_2(\cos\beta)$.

Therefore, up to second moments, the orientational distribution function is given by:

$$p(\beta) = \frac{1}{2} + \frac{5}{2}\langle P_2 \rangle P_2(\cos\beta) + \ldots \,, \tag{1.2}$$

where $P_2(\cos\beta)$ is the second Legendre polynomial (Figure 1.4(b)):

$$P_2(\cos\beta) = \frac{3}{2}\cos^2\beta - \frac{1}{2} \,, \tag{1.3}$$

and $\langle P_2 \rangle$ is the second rank order parameter characterizing the degree of alignment of the molecular z axis with respect to the nematic director **n**:

$$\langle P_2 \rangle = \int_0^{\pi} P_2(\cos\beta) p(\beta) \sin\beta \, d\beta \ . \tag{1.4}$$

In the isotropic phase, where all orientations have the same probability, $\langle P_2 \rangle = 0$, whereas in a perfectly order phase, where $\beta = 0$ for all molecules, $\langle P_2 \rangle = 1$.

Order parameters can also be expressed using a Cartesian tensor representation [6-8]. At the second-rank level, the orientational order of a rigid molecule is described by the tensor **Q**:

$$Q_{ij}^{IJ} = \left\langle \frac{3}{2} l_{i,I} l_{j,J} - \frac{1}{2} \delta_{ij} \delta_{IJ} \right\rangle, \qquad \begin{cases} i, j = x, y, z \\ I, J = X, Y, Z \end{cases} , \tag{1.5}$$

where $\{x, y, z\}$ is a set of arbitrary molecular axes, $\{X, Y, Z\}$ is a set of arbitrary laboratory axes, $l_{i,I}$ is the cosine of the angle between the molecular axis i and the laboratory axis I, δ_{ij} is the Kronecker delta, and the angular brackets denote an orientational average:

$$\langle ... \rangle = \int ... \, p(\Omega) d\Omega \quad . \tag{1.6}$$

From the definition of the Q tensor, it follows that $\sum_I Q_{ii}^{II} = 0$ and $\sum_i Q_{ii}^{II} = 0$.

For a rod-like molecule in a conventional uniaxial nematic phase, taking the laboratory Z axis parallel to the nematic director **n** and the molecular z axis parallel to the rod long-axis, the ordering tensor **Q** is diagonal, with $Q_{xx}^{ZZ} = Q_{yy}^{ZZ} = -Q_{zz}^{ZZ} / 2$. So there is a single independent order parameter:

$$Q_{zz}^{ZZ} = \left\langle \frac{3}{2} \cos^2\beta - \frac{1}{2} \right\rangle \ , \tag{1.7}$$

which is also indicated as S_{zz} and is identical to $\langle P_2 \rangle$ in Eq. (1.4).

If the phase is uniaxial but the molecules are not, the ordering tensor, Eq. (1.5), is given by:

$$Q_{ij}^{ZZ} = S_{ij} = \begin{pmatrix} S_{xx} & S_{xy} & S_{xz} \\ S_{yx} & S_{yy} & S_{yz} \\ S_{zx} & S_{zy} & S_{zz} \end{pmatrix} \quad , \tag{1.8}$$

with

$$S_{ij} = S_{ji} = \left\langle \frac{3}{2} l_{i,Z} l_{j,Z} - \frac{1}{2} \delta_{i,j} \right\rangle \ , \tag{1.9}$$

and is called the Saupe ordering matrix **S**.

Real mesogens are not rigid molecules, but invariably possess some degree of conformational flexibility. Let's denote with $\boldsymbol{\chi}$ the set of molecular torsional angles; then the distribution function becomes dependent on the molecular conformation as well as orientation. It can be expressed as [8]:

$$p(\Omega, \boldsymbol{\chi}) = w(\boldsymbol{\chi})\, p_{\boldsymbol{\chi}}(\Omega) \ , \tag{1.10}$$

where $p_{\boldsymbol{\chi}}(\Omega)$ gives the probability density of finding a molecule with orientation between Ω and $\Omega+d\Omega$, given that it is in the conformation state defined by the set of torsional angles $\boldsymbol{\chi}$, and $w(\boldsymbol{\chi})$ is the conformational distribution function in the orientationally ordered phase. Order parameters are then obtained by averaging the contributions of all conformations:

$$Q_{ij}^{IJ} = \int d\boldsymbol{\chi}\, w(\boldsymbol{\chi}) \left(Q_{ij}^{IJ} \right)_{\boldsymbol{\chi}} \quad , \tag{1.11}$$

where $\left(Q_{ij}^{IJ} \right)_{\boldsymbol{\chi}}$ is the order parameter for the conformation specified by the angles $\boldsymbol{\chi}$:

$$\left(Q_{ij}^{IJ} \right)_{\boldsymbol{\chi}} = \int \left(\frac{3}{2} l_{i,I} l_{j,J} - \frac{1}{2} \delta_{ij} \delta_{IJ} \right) p_{\boldsymbol{\chi}}(\Omega)\, d\Omega \quad . \tag{1.12}$$

1.2.1.2 Molecular order parameters from NMR spectra

In principle microscopic order parameters can be experimentally determined using techniques capable of accessing information on a molecular scale. One of the most important is Nuclear Magnetic Resonance (NMR) spectroscopy [9,10]. The NMR

spectrum of a molecule is the result of different kinds of interactions, between its nuclear spins and the external magnetic field and among the nuclear spins themselves. These magnetic interactions are anisotropic, since they depend on molecular tensors **T**: the chemical shielding tensor **σ**, the direct dipolar coupling tensor **D**, the indirect coupling tensor **J**, and, for nuclei with spin number $I \geq 1$, the quadrupolar coupling tensor **q** (see Table 1.2). If molecular motions are sufficiently fast on the NMR timescale, the spectral observables are determined by the average values of these tensors according to the orientational distribution function appropriate for the molecule in the phase. Therefore NMR can provide information on the order parameters of different molecular sites.

Technique	Nucleus	T
Proton NMR	^{1}H	**D**
Deuterium NMR	^{2}H	**q**
Carbon-13 NMR	^{13}C	**σ**

Table 1.2. NMR techniques mostly used to determine order parameters of liquid crystals. The last column specifies the relevant molecular tensor **T** (direct dipolar coupling tensor **D**, quadrupolar tensor **q**, chemical shielding tensor **σ**).

In particular, the spin Hamiltonian (and therefore the spectral features) depends on $\langle T^{ZZ} \rangle$, the average component of the molecular tensor **T** resolved along the direction (Z) of the static magnetic field. The relation between $\langle T^{ZZ} \rangle$ and the order parameters is given by [9,10]:

$$\begin{aligned} \langle T^{ZZ} \rangle &= T_{iso} + \langle T^{ZZ}_{aniso} \rangle \\ &= T_{iso} + \frac{2}{3} \sum_{i,j=x,y,z} S_{ij} T_{ij} \end{aligned} \quad , \tag{1.13}$$

where T_{ij} are the cartesian components of the tensor **T** in the molecular frame and $T_{iso} = Tr(\mathbf{T})/3,$ with the symbol Tr indicating the trace of the tensor. S_{ij} are molecular order parameters; they are defined as in Eq. (1.9) with the Z axis parallel to the direction of the magnetic field.

As an example, let's consider the case of deuterium NMR (^{2}H-NMR), where the

relevant coupling tensor is **q**. This tensor is traceless and for deuterons it is approximately axially symmetric in a molecular frame having the *z* axis parallel to the carbon-deuterium (C–D) bond. Therefore with this choice $q_{xx} = q_{yy} = -q_{zz}/2$ and Eq. (1.13) takes the form:

$$\left\langle q^{ZZ} \right\rangle = \left\langle q_{aniso}^{ZZ} \right\rangle = q_{CD} S_{CD} \quad , \tag{1.14}$$

where $q_{CD}=q_{zz}$ and $S_{CD}=S_{zz}$. Because of the quadrupolar interaction, each non-equivalent deuteron in a molecule gives rise to a doublet of lines in the spectrum, with a splitting $\Delta\nu$ given by [10,11]:

$$\Delta\nu = \frac{3}{2}\left\langle q_{ZZ}^{aniso} \right\rangle = \frac{3}{2} q_{CD} S_{CD} \quad . \tag{1.15}$$

Therefore, measurement of quadrupolar splittings provides direct information on the order parameters of the C-D bonds with respect to the direction of the magnetic field.

1.2.2 Macroscopic approach

Let **κ** indicate a second rank tensorial physical properties of the material, such as the magnetic susceptibility, the static dielectric permittivity or the optical dielectric tensor. In order to define an order parameter that vanishes in the isotropic phase, the anisotropic part of tensor, $\boldsymbol{\kappa}_{aniso}$, is considered:

$$\kappa_{aniso}^{IJ} = \kappa^{IJ} - \kappa_{iso}\delta^{IJ} , \tag{1.16}$$

where *I*, $J = X, Y, Z$ are the axes of a laboratory frame, δ is the Kronecker delta, and $\kappa_{iso} = Tr(\boldsymbol{\kappa})/3$ is the (scalar) value of the physical property in the isotropic phase. A macroscopic order parameter **Q** is then defined as [1,6]:

$$Q^{IJ} = \frac{1}{C}\kappa_{aniso}^{IJ} \quad , \tag{1.17}$$

where *C* is a normalization constant, with the same unit of **κ**, chosen in such a way that the major principal component of **Q** is equal to 1 for a perfectly ordered phase. For example, in the nematic (N) phase the tensor **κ** is diagonal in a frame with the *Z* axis

parallel to the director **n**: denoting by $\kappa_{\parallel}$ and $\kappa_{\perp}$ the components of **κ** parallel and perpendicular to the director, the following form is obtained the ordering tensor **Q**:

$$\mathbf{Q} = \begin{pmatrix} -S/2 & 0 & 0 \\ 0 & -S/2 & 0 \\ 0 & 0 & S \end{pmatrix} \quad , \tag{1.18}$$

where

$$S = \frac{\kappa_{\parallel} - \kappa_{\perp}}{\left(\kappa_{\parallel} - \kappa_{\perp}\right)_0} \quad , \tag{1.19}$$

with the zero in the subscript indicating perfect orientational order. As an example we can consider the macroscopic order parameter obtained from the optical dielectric tensor, that is from measurement of the birefringence Δn, which is one of the most common techniques used to determine order parameters. Here S can be obtained as [12]:

$$S = \frac{\Delta n}{\Delta n_0} \quad , \tag{1.20}$$

where Δn_0 corresponds to the value of the birefringence extrapolated at temperature T=0 K.

1.3 The Maier-Saupe theory

Maier and Saupe developed a seminal molecular field theory predicting the transition from the isotropic (I) to the nematic (N) phase in thermotropic liquid crystals made of rod-like molecules [13]. The Maier-Saupe (MS) approach is based on a mean-field approximation: direct intermolecular correlations are neglected, and the many-body potential describing the interactions of a given molecule with all other molecules is replaced by an effective single-particle potential, also called molecular field potential [2,8,14]. The orientationally dependent part of the molecular field potential, *i.e.* the part which depends on the anisotropy of the intermolecular interactions, takes the following form for a system of rigid rods:

$$U_{MS}^{or}(\beta) = -c\langle P_2 \rangle P_2(\cos\beta) \ , \tag{1.21}$$

where β is the angle between the rod long-axis and the director **n** (Figure 1.4(a)), P_2 is the second Legendre polynomial, and $\langle P_2 \rangle$ is the order parameter (see Eqs. (1.3) and (1.4)). The parameter *c*, having the dimension of energy, scales the interaction potential. According to Eq. (1.21), rod-like molecules preferentially align their long axis parallel to the director. In their original derivation [13], Maier and Saupe assumed dispersion interactions between molecules, and *c* was therefore related to the anisotropy of the molecular polarizability. This restriction is however not necessary: the form of the potential in Eq. (1.21) is quite general, being the simplest expression that accounts for both the molecular and the phase symmetry. The single particle orientational distribution function is related to the Maier-Saupe potential according to:

$$p(\beta) = \frac{\exp\left[-U_{MS}^{or}(\beta)/k_B T\right]}{\int \exp\left[-U_{MS}^{or}(\beta)/k_B T\right]\sin\beta d\beta} \ , \tag{1.22}$$

where k_B is the Boltzmann constant and T is the temperature. In the MS theory $\langle P_2 \rangle$ is found to be a universal function of the reduced temperature T/T_{NI}, where T_{NI} is the nematic-isotropic (N-I) transition temperature. The solid line in Figure 1.5 shows the predicted temperature dependence of the order parameter. A first order N-I transition is evident from the discontinuous change of $\langle P_2 \rangle$ at T_{NI}.

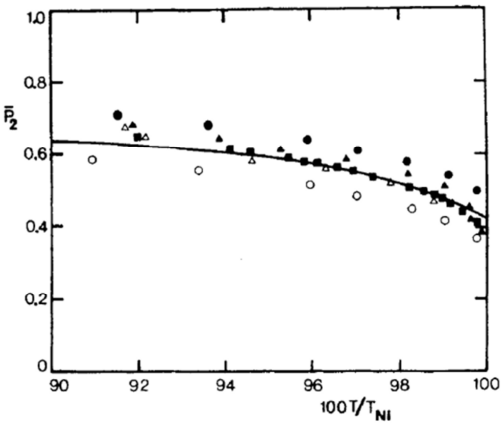

Figure 1.5. Order parameter as a function of the reduced temperature T/T_{NI}: Maier-Saupe prediction (solid line) and experimental data for some rod-like nematic liquid crystals [14].

1.4 References

1 P. G. de Gennes and J. Prost, *The Physics of Liquid Crystals*, Clarendon Press, Oxford, 1993.

2 L. M. Blinov, *Structure and Properties of Liquid Crystals*, Springer, Dordrecht, 2011, ch. 4 .

3 D. Demus, in *Handbook of Liquid Crystals*, ed. D. Demus, J. Goodby, G. W. Gray, H.-W. Spiess and V. Vill, 1998, Wiley-VCH, Weinheim, vol. 1, ch 6.

4 P. Oswald and P. Pieranski, *Nematic and Cholesteric Liquid Crystals*, Taylor & Francis, Boca Raton, 2005, ch. B.VII-B.VIII.

5 S.T. Lagerwall, *Ferroelectric and Antiferroelectirc Liquid Crystals*, Wiley VCH, Weinheim, 1999, ch. 3.

6 D. Dunmur and K. Toriyama, in *Handbook of Liquid Crystals*, ed. D. Demus, J. Goodby, G. W. Gray, H.-W. Spiess and V. Vill, 1998, Wiley-VCH, Weinheim, vol. 1, ch.7.

7 C. Zannoni, in *The Molecular Physics of Liquid Crystals*, ed. G. R. Luckhurst and G. W. Gray, Academic Press, 1979, ch. 3.

8 G. R. Luckhurst, in *Physical Properties of Liquid Crystals*, ed. D. Dunmur, A. Fukuda and G. R. Luckhurst, Inspec, London, 2001, ch. 2.

9 P. L. Nordio and U. Segre, in *The Molecular Physics of Liquid Crystals*, ed. G. R. Luckhurst and G. W. Gray, Academic Press, 1979, ch. 16.

10 *Nuclear Magnetic Resonance of Liquid Crystals*, ed. J. W. Emsley, Kluwer, Dordrecht, 1985.

11 P. Lesot and J. Courtieu, *Prog. Nucl. Mag. Res. Sp.*, 2009, **55**, 128-159.

12 S. J. Picken, in *Physical Properties of Liquid Crystals*, ed. D. Dunmur, A. Fukuda and G. R. Luckhurst, Inspec, London, 2001, ch. 2.

13 W. Maier and A. Saupe, *Z. Naturforsch. A*, 1958, **13**, 564–566. (b) W. Maier and A. Saupe, *Z. Naturforsch. A.*, 1959, **14**, 882–889. (c) W. Maier and A. Saupe, *Z. Naturforsch. A* , 1960, **15**, 287–292.

14 M. A. Osipov, in in *Handbook of Liquid Crystals*, ed. D. Demus, J. Goodby, G. W. Gray, H.-W. Spiess and V. Vill, 1998, Wiley-VCH, Weinheim, vol. 1, ch.3.

Chapter 2

Liquid crystals of bent-shaped molecules

2.1 Bent-shaped mesogens: the chemistry

Bent mesogens are molecules with a banana-like shape. From a chemical point of view, two molecular architectures can be distinguished: bent-core compounds and odd liquid crystals dimers (Figure 2.1).

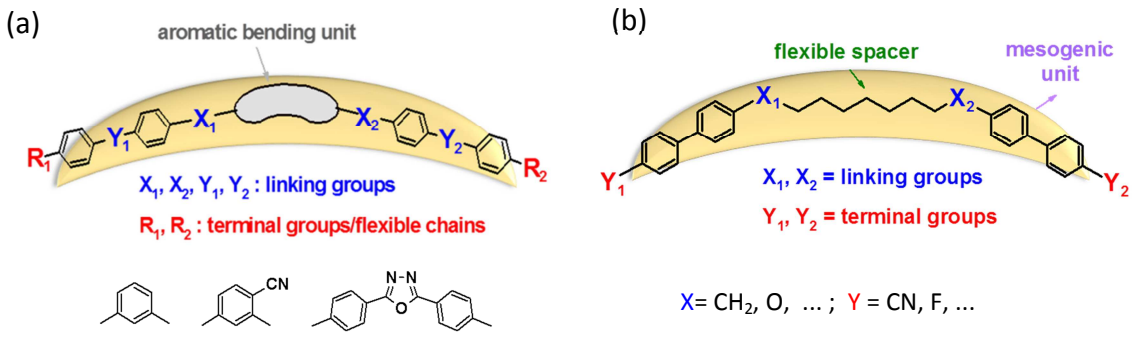

Figure 2.1. Chemical structure of: (a) bent-core compounds, with examples of popular bending units shown at the bottom; (b) odd liquid crystal dimers.

Bent-core molecules are characterized by a fairly rigid aromatic core and terminal flexible chains [1,2]. The aromatic bending unit can be a 1,3-phenylene group, with or without substituents, or an oxadiazole group, just to give some examples.

Liquid crystal dimers are made of two terminal mesogenic units connected by a flexible spacer, usually an alkyl chain, of variable length [3]. According to the parity of the spacer, dimers are classified as odd or even. Odd dimers usually have a bent shape, whereas even dimers are generally elongated. Cyanobiphenyl mesogenic groups (Y=CN

in Figure 2.1(b)) are extensively used, but other aromatic units can be found. The group joining the mesogenic unit and the spacer is called linking group: common examples are the methylene (–CH_2–) and the ether (–O–) groups.

2.2 Conventional and unconventional phase organizations of bent-shaped mesogens

Bent core compounds have a strong tendency to form smectic phases; indeed, the first bent-core compounds that were synthesised did not exhibit a nematic phase. These smectic phases have attracted considerable attention because of their unique organization, which has no analogue in conventional rod-like liquid crystals: they show polar order and, despite being made from achiral molecule, also chiral superstructures [1,4] (Figure 2.2(a)).

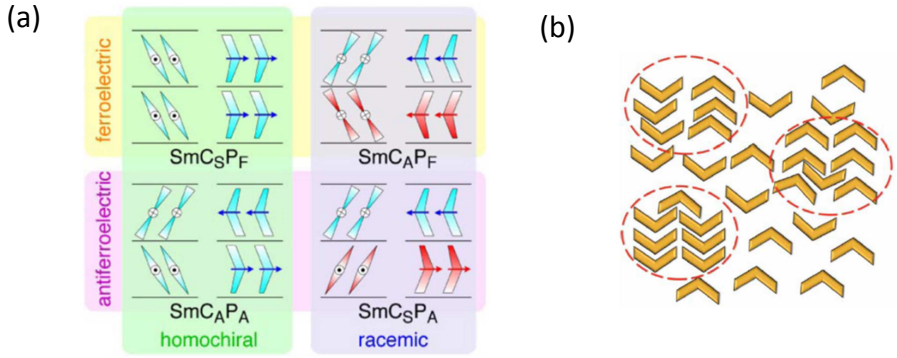

Figure 2.2. (a) Tilted smectic (SmC) phases of bent-core molecules. Reprinted with permission from [4], Copyright 2006 The Japan Society of Applied Physics. (b) Cartoon representing a uniaxial nematic arrangement of smectic clusters of bent-core molecules. Reprinted with permission from [2] Copyright 2013 Taylor & Francis.

Subtle tuning of the molecular structure was required to stabilize nematic phases, including choice of the aromatic bending unit, introduction of substituents in certain positions on this unit, and modifications involving the flexible chains [5-9]. It became soon apparent that the nematic phase of bent-core mesogens also has distinctive features, different from those of conventional rod-like systems. Some bent-core systems have been claimed to form the long sought-after biaxial nematic phase [10,11]. However the characterization of biaxial order is delicate [6,12], and at present there is

no conclusive proof of the existence of a biaxial phase in thermotropic nematics. It has been proposed that some properties of nematics of bent-core mesogens could result from the macroscopic uniaxial arrangement of smectic-like clusters of molecules [2,6,13] (Figure 2.2(b)). Evidence for the formation of chiral domains in nematic liquid crystals of achiral bent-core mesogens has also been reported [2,14]. Moreover, upon chiral doping, achiral bent-core nematics have been shown to form blue phases stable of over a wide temperature range [15,16].

Liquid crystal dimers have been known to organize into a conventional nematic (N) phase since a long time [3]. The initial interest for these systems was related to the discovery of a characteristic odd-even effect in the properties of their nematic-isotropic (N-I) phase transition: the temperature and other transitional properties were found to depend strongly on the parity (even or odd) of the spacer. Odd liquid crystal dimers are now arousing a renewed interest, especially after the discovery of a new chiral nematic organization, denoted as twist-bend nematic (N_{TB}) [17]. The following section illustrates the structure of the N_{TB} phase and summarizes some of the experimental evidences which have led to its identification.

2.2.1 The Twist-Bend Nematic phase (N_{TB})

Certain odd liquid crystal dimers have been found to undergo a transition from the conventional nematic phase (N) to a second unknown nematic phase (N_X) on cooling [17-22]. The CB7CB dimer (Figure 2.3(b)) was the first compound for which the N_X phase was identified as a twist-bend nematic (N_{TB}), by Cestari *et al.* [17].

The N_{TB} organization is sketched in Figure 2.3(a). It is characterized by a heliconical director precessing about an axis (Z) with conical angle θ_0 and helical pitch p. This organization has global D_∞ and local C_2 point group symmetry. In addition to its chirality, another characteristic feature of this structure is the presence of local bend deformations of the director, $\mathbf{B} = (\nabla \times \mathbf{n}) \times \mathbf{n}$. The possibility that achiral bent-shaped molecules could form an N_{TB} organization had been theoretically predicted many years before its experimental observation [23-24], and was suggested also by Monte Carlo simulations of a small system of V-shaped particles formed from Gay-Berne units [25].

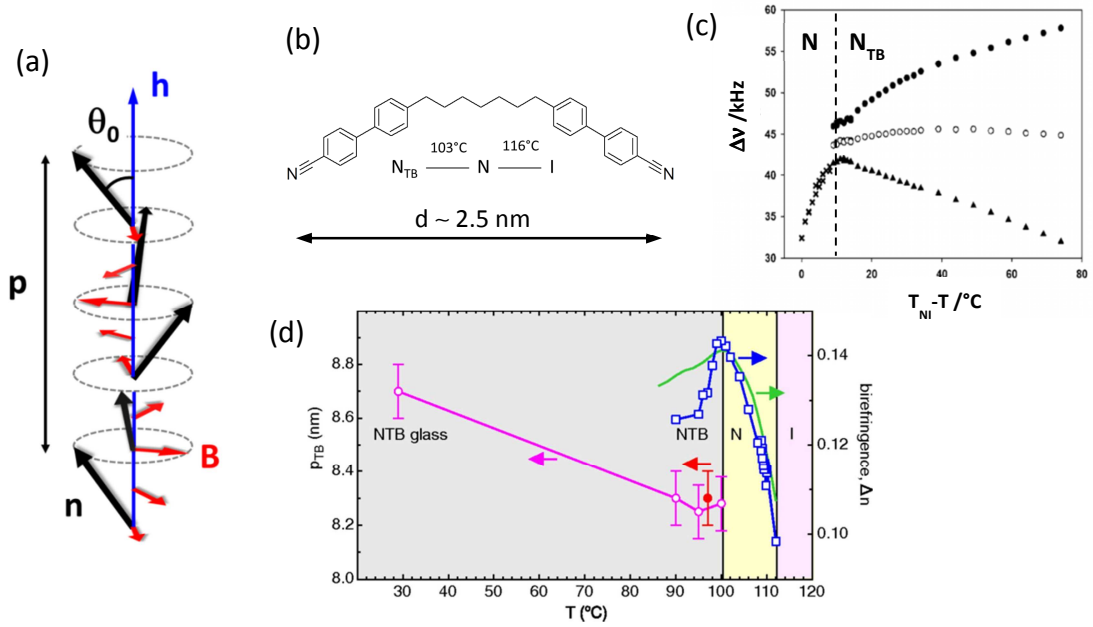

Figure 2.3 (a) The N_{TB} phase organization (one of the two degenerate helicoidal domains), with θ_0 the conical angle and p the helical pitch; $\mathbf{n}$ and $\mathbf{h}$ are unit vectors parallel to the local director and to the helix axis, respectively, and $\mathbf{B} = (\nabla \times \mathbf{n}) \times \mathbf{n}$. (b) Molecular structure and phase transitions of the liquid crystal dimer CB7CB. The average molecular length of CB7CB is about 2.5 nm. (c) Temperature dependence of the quadrupolar splittings $\Delta\nu$ for the deuterated probe 8CB-d_2, dissolved in CB7CB. The dashed vertical line indicates the N_{TB}-N phase transition. Adapted with permission from [18] Copyright 2012 American Chemical Society. (d) Temperature dependence of the helical pitch p (empty circles and pink line) and of the birefringence Δn (empty squares and blue line) for CB7CB. Reproduced with permission from [26] Copyright 2013 National Academy of Sciences, USA.

In their work, Cestari *et al.* [17] used a variety of different experimental techniques to characterize the N_X phase, including differential scanning calorimetry (DSC), X-ray diffraction (XRD), polarized optical microscopy (POM), and deuterium nuclear magnetic resonance (^{2}H-NMR). DSC indicated that in CB7CB the N_X-N transition is weakly first order. The absence of sharp reflections in the XRD diffraction pattern proved that N_X is a nematic, rather than smectic, phase. Samples contained in planar cells exhibited a characteristic striped texture when observed by POM, with a periodicity of a few microns. The birefringence colours of consecutive stripes reversed on rotation of the microscope stage, suggesting the existence of chiral domains with opposite handedness. Important information on the phase structure have been provided by ^{2}H-NMR: bifurcation of the quadrupolar splitting on entering the N_X phase (Figure 2.3(c)) unequivocally demonstrated that in this phase the director has a chiral organization. This result was striking, since CB7CB is an achiral molecule; inspired by Dozov's predictions [24], the authors assigned the N_X phase to an N_{TB} organization. A

more detailed discussion of the ^{2}H-NMR experiments will be presented in Chapter 9. The existence of an N_{TB} organization, both in CB7CB and in other odd methylene-linked dimers, is being progressively confirmed by different experimental techniques. Valuable insights have been reached by freeze-fracture transmission electron microscopy (FFTEM) [26,27] and birefringence measurements [26-29] (Figure 2.3(d)). FFTEM experiments have shown that the N_{TB} phase is characterized by a remarkably short periodicity, of the order of a few molecular lengths. The birefringence typically exhibits a decrease on entering the N_{TB} phase, which was ascribed to a tilt of the director.

The N_{TB}-N phase transition appears to be very sensitive to details of the molecular structure: it has been detected mainly in methylene-linked dimers, whereas it appears to be less common in ether-linked dimers [22,30,31].

2.3 Unconventional physical properties in the N phase

In addition to their phase behaviour, liquid crystals of bent-shaped molecules are arousing considerable interest also because of the outstanding physical properties of their N phase. Many of these properties exhibit distinctive features, different from those of conventional rod-like nematics, whose origin is not fully understood. Bent-core compounds have been shown to possess unusual flexoelectric [32-34] and elastic properties [32,33,35-38], large viscosity [35,39], as well as nonstandard dielectric relaxation [40] and electroconvection regimes [41]. Unconventional flexoelectric and elastic properties have been reported also for odd liquid crystals dimers [22,27,42,43].

Elasticity and flexoelectricity are properties of fundamental interest, both on their own and for other basic phenomena, such as the formation of topological defects and the possible role played in stabilizing modulated phase, such as the blue phases [16,44] or the recently discovered twist-bend nematic phase [23,24]. They are also relevant for applications, including the development of materials optimized for new display modes [42,43] or for electromechanical energy harvesting and conversion [45,46].

In the following sections, elasticity and flexoelectricity in liquid crystals are defined, and a brief summary of the unconventional behaviour of bent-shaped mesogens is presented.

2.3.1 Elastic constants

Liquid crystals are elastic fluids: they oppose a torque to distorsions of the director with respect to the equilibrium state (*curvature elasticity*) [47]. The fundamental modes of deformations and the associated elastic constants are defined by the phase symmetry. The elastic continuum theory of the nematic (N) phase is due to Oseen and Frank [48,49]: three independent bulk deformation modes are allowed, splay $\mathbf{S} = \hat{\mathbf{n}}\left(\nabla \cdot \hat{\mathbf{n}}\right)$, twist $T = \hat{\mathbf{n}} \cdot \left(\nabla \times \hat{\mathbf{n}}\right)$, and bend $\mathbf{B} = \left(\nabla \times \hat{\mathbf{n}}\right) \times \hat{\mathbf{n}}$ (Figure 2.4), and the bulk elastic free energy density is given by:

$$f_{\text{def}} = \frac{1}{2}\left(K_{11}\mathbf{S}^2 + K_{22}T^2 + K_{33}\mathbf{B}^2\right) \quad , \tag{2.1}$$

where K_{11}, K_{22} and K_{33} are respectively the splay, twist and bend elastic constants.
The elastic constants are material parameters, which depend on the molecular structure of the mesogen and on the orientational order in the mesophase. The relationship between the molecular structure and deformations on length scales much longer than the molecular dimensions is however not obvious. Various molecular theories of liquid crystalline elasticity have been developed, usually for systems of simple idealized particles, such as rigid rods. A review of these theories can be found in Ref. [50, 51].

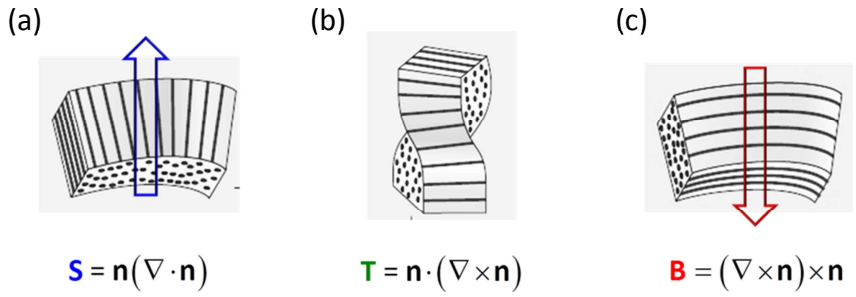

Figure 2.4 Principal modes of director deformations in the nematic (N) phase : (a) splay, (b) twist, (c) bend.

Here we focus on the experimental evidences. The elastic moduli of nematics have a magnitude of the order of some piconewtons. In conventional rod-like nematics $K_{33} > K_{11} > K_{22}$ is generally found, and the elastic constants increase with decreasing temperature (increasing order parameter): K_{11} and K_{22} are approximately proportional to

S_{zz}^2 (S_{zz} being the major order parameter), whereas this is not always true for K_{33} [51, 52].

Quite different features have been detected in nematics of bent-shaped molecules. An increasing number of experimental observations on bent-core compounds indicate that these systems are characterized by a low bending stiffness. Lowering of the bend elastic constant has been evidenced upon doping conventional nematics with bent-core mesogens [53-55]. More recently, the elastic behaviour in pure bent-core compounds has been characterized and $K_{11} > K_{33}$ has been found, at variance with rod-like liquid crystals [32,33,35-38]. Moreover, the bend elastic constant appears to be only weakly dependent on temperature. Measurements of the elastic constants of odd liquid crystal dimers are scarcer, but even for these systems K_{33} has been found to be lower than K_{11} and unusually small [22,27,43]. The origin of the small K_{33} values is not completely clear. It was proposed that the bent molecular shape could be responsible for this behaviour [36], but this interpretation has been questioned and it was instead suggested that smectic clusters could be the cause of the small K_{33} [35].

2.3.2 Flexoelectric coefficients

Flexoelectricity in liquid crystals bears some analogy to piezoelectricity in crystalline solids [56]: it consists in the appearance of an electric polarization in response to splay or bend deformations of the director (*direct flexoelectric effect*). Conversely, splay and bend distortions of the director can be induced upon application of an external electric field (*converse flexoelectric effect*). Flexoelectricity was discovered by Meyer [57]; according to his derivation the flexoelectric polarization is given by:

$$\mathbf{P}_{\text{flexo}} = e_1\mathbf{S} + e_3\mathbf{B} \quad , \tag{2.2}$$

where **S** and bend **B** are the splay and bend deformation vectors (see Figure 2.4) and e_1, e_3 are respectively the splay and bend flexoelectric coefficients of the liquid crystalline material. The sign of the flexoelectric coefficients determines the relative orientation of the polarization and deformation vectors (Figure 2.5).

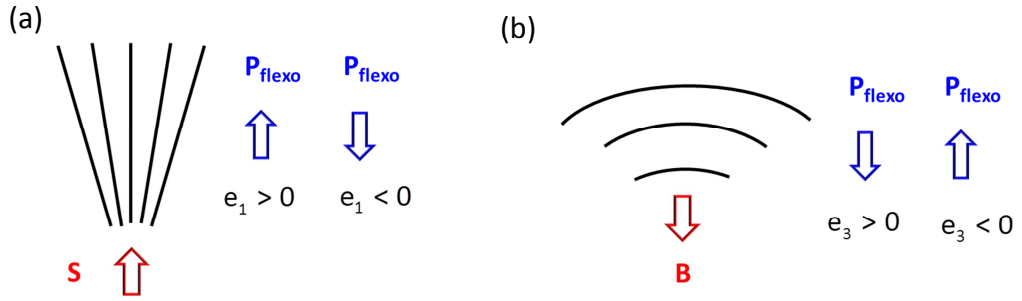

Figure 2.5 Flexoelectric effect: (a) splay, (b) bend. The relative orientation of the polarization and deformation vectors depends on the sign of the flexoelectric coefficients.

Meyer also provided a first molecular interpretation of flexoelectricity, in terms of the combination of shape asymmetry and electric polarity in molecules (*dipolar flexolectricity*, Figure 2.6(a)). In an undeformed nematic phase, the molecular distribution is non-polar: thus a banana-shaped molecule will preferentially align its long axis along the director **n**, but its short axis will assume with equal probability any orientation in the plane perpendicular to **n**. However, if the liquid crystal is subjected to a bend deformation the orientational distribution function of the short axis will become polar: molecules can pack better if their curvature follows that of the bent director field. If the banana-shaped molecules possess a transverse dipole moment, an electric polarization will be induced. Similarly, wedge-shaped molecules having a longitudinal dipole will couple effectively to a splay deformation.

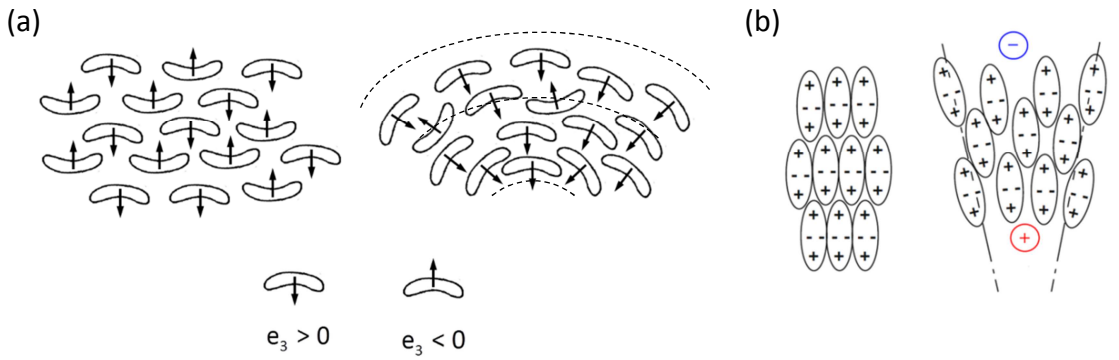

Figure 2.6 Simple molecular interpretations of the flexoelectric effect. (a) The dipolar model of Meyer (only the case of banana-shaped molecules is shown). The arrows represent the molecular electric dipole moments. (b) The quadrupolar model of Prost and Marcerou. In the deformed state, the overall density of positive charges is higher in the lower part than in the upper part of the picture, and a polarization is produced.

Later, Prost and Marcerou [58] suggested that flexoelectricity can be observed even in nematics made of apolar, rod-like molecules: this happens because splay and bend deformations can induce gradients in the electric quadrupolar density (*quadrupolar flexoelectricity*, Figure 2.5 (b)).

Flexoelectric coefficients of rod-like nematics are quite small, typically of the order of a few picocoulombs per meter [56,59,60]. This fact, coupled to the experimental difficulties involved in the determination of the flexoelectric coefficients, resulted in different values being reported for the same compound [56,59]. Bent-core compounds and liquid crystal dimers have been found to exhibit higher flexoelectric couplings than rod-like liquid crystals [32-34,43,61]. However, even for these systems controversial results were obtained: a giant value of the bend flexoelectric coefficients was reported for a bent-core system [34], which was not confirmed by a later investigation [62]. More in general it is still not clear what are the limits of the flexoelectric coupling strengths that can be achieved [2,63].

Models of flexoelectricity developed for simple particles have been useful to get a general understanding of this phenomenon. However real molecules are not rigid objects, nor simple dipoles and quadrupoles: proper account of molecular flexibility and of the molecular charge distribution is required to capture the interplay between the molecular shape and the molecular electric properties [64].

2.3.3 Display applications: the flexoelectrooptic effect

Conventional twisted-nematic liquid crystal displays (TN-LCD) exhibit some shortcomings, such as narrow viewing angles and relatively long response times. Therefore the development of new high-performance LCD modes and of liquid crystal materials optimized for these modes is still an active area of research. Possible new technologies which have attracted much interest in the last years include displays based on the flexoelectrooptic effect [65].

The flexoelectrooptic effect consists in the rotation of the helix axis of a chiral nematic liquid crystal[*] around an electric field perpendicular the helix axis. The most common cell configuration is the ULH (uniform lying helix) geometry, where the liquid crystal is

[*] Here chiral nematic indicates a nematic liquid crystal doped with a chiral additive and having a cholesteric-like organization.

aligned with the helix axis parallel to the cell surfaces (Figure 2.7). The rotation angle ϕ is given by [42]:

$$\phi = \frac{\bar{e}}{\bar{K}} \frac{p}{2\pi} E \quad , \tag{2.3}$$

where $\bar{e}$ is the effective flexoelectric coefficient, $\bar{e} = (e_1 - e_3)/2$, $\bar{K}$ is the effective elastic constant, $\bar{K} = (K_{11} + K_{33})/2$, p is the helical pitch and E is the electric field (magnitude and sign). The ratio $\bar{e}/\bar{K}$ is called flexoelastic ratio.

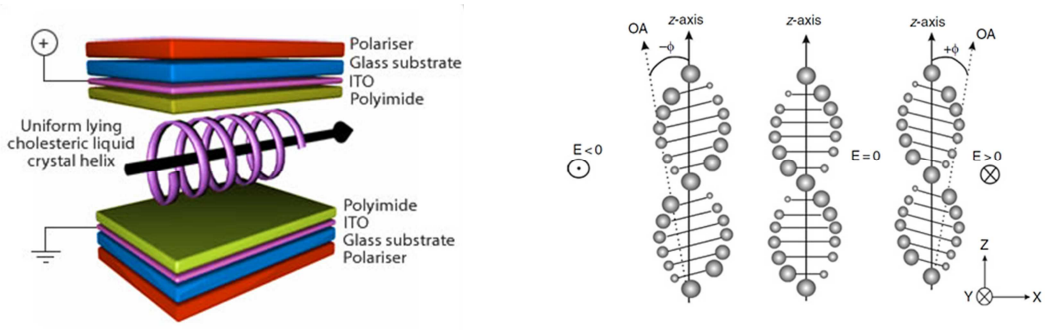

Figure 2.7. Schematic representation of the flexolectroptic effect in the ULH configuration. http://www-g.eng.cam.ac.uk/CMMPE/res_phenom_flexo.html

Compared to TN-LCDs, displays based on the flexoelectrooptic effect would have the following advantages [42]: (i) wider viewing angles, because of the in-plane switching mechanism: (ii) better gray-scale modulation, because of the linear relation between ϕ and E; (iii) faster switching times.

In order to exploit the potential of this display mode, nematic liquid crystals with high values of $\bar{e}/\bar{K}$ are required. Bent-shaped mesogens appear to be promising candidate, because of their unconventional flexoelectric and elastic properties.

2.4 Thesis Outline

In this thesis the phase and material behaviour of liquid crystals of bent molecules have been investigated by theoretical and computational methods, with the aim to establish a connection between the macroscopic behaviour and the molecular structure. This is a challenging task: computational methods such as quantum mechanical calculations and

atomistic Molecular Dynamics simulations are in many cases insufficient and alternatives routes must be found. In this work different methods have been used and developed, suitable to cover or connect the different length scales involved.

In particular we have focused on the following problems: (***i***) the origin and the structure of the twist-bend nematic phase (N_{TB}); (***ii***) the elastic and flexoelectric properties of the nematic (N) phase.

(***i***) To get insight into the molecular origin of the N_{TB} phase, we propose an extension of the Maier-Saupe model, modified to take into account the coupling between the molecular shape and the director modulation. Our objectives are the following: checking whether we can predict the existence of a nematic (N) to N_{TB} phase transition; assessing the effect of changes in the molecular structure on the transition; investigating the possible relation between the formation of the N_{TB} phase and the elastic behaviour. The model is presented in Chapter 3. In Chapter 4, the phase organization of bent-shaped particles is examined using Molecular Dynamics simulations, to further check the formation an N_{TB} phase and its molecular determinants and to characterize the molecular organization in this phase.

Based on our generalized Maier-Saupe model we also intend to obtain some general information about the structural parameter (pitch and conical angle) of the N_{TB} phase. In Chapter 9, a molecular model capable of providing quantitative estimates of these parameters starting from a realistic representation of the molecular structure is presented.

(***ii***) The relationship between the molecular structure and the elastic and flexoelectric properties of liquid crystals of bent-shaped molecules has been investigated using a methodology capable of bridging the different length scales involved. The methodology, which is illustrated in Chapter 5, had been previously applied to the prediction of the elastic constants of conventional rod-like LCs, providing results in good quantitative agreement with experimental data, at a modest computational cost. Here the methodology has been extended and used to predict various properties. In particular we have focused on the elastic and flexoelectric properties of bent-core compounds and liquid crystal dimers with various molecular structures, with the aim to understand the origin of their unsual behaviour. Collaboration with experimental groups has allowed us to validate our computational approach against a large number of

experimental data. The results obtained are presented in Chapters from 6 to 8.

2.5 References

1 R. A. Reddy and C. Tschierske, *J. Mater. Chem.*, 2006, **16**, 907-961.

2 A. Jákli, *Liq. Cryst. Rev.*, 2013, **1**, 65-82.

3 C. T. Imrie and P. A. Henderson, *Chem. Soc. Rev.*, 2007, **36**, 2096–2124.

4 H. Takezoe and Y. Takanishi, *Jpn. J. Appl. Phys.*, 2006, **45**, 597-625.

5 W. Weissflog, H. Nadasi, U. Dunemann, G. Pelzl, S. Diele, A. Eremin and H. Kresse, *J. Mater. Chem.*, 2001, **11**, 2748 – 2758.

6 C. Tschierske and D. J. Photinos, *J. Mater. Chem.*, 2010, **20**, 4263–4294.

7 C. Keith, A. Lehmann, U. Baumeister, M. Prehm and C. Tschierske, *Soft Matter*, 2010, **6**, 1704-1721.

8 M. Lehmann, *Liq. Cryst.*, 2011, **38**, 1389–1405.

9 H. F. Gleeson, S. Kaur, V. Görtz, A. Belaissaoui, S. Cowling and J.W. Goodby, *ChemPhysChem*, 2014, **15**, 1251 – 1260.

10 B. R. Acharya, A. Primak, and S. Kumar, *Phys. Rev. Lett.*, 2004, **92**, 145506.

11 V. Prasad, S.-W. Kang, K. A. Suresh, L. Joshi, Q. Wang and S. Kumar, *J. Am. Chem. Soc.*, 2005, **127**, 17224–17227.

12 R. Berardi, L. Muccioli, S. Orlandi, M. Ricci and C. Zannoni, J. *Phys.: Condens. Matter*, 2008, **20**, 463101.

13 O. Francescangeli, V. Stanic, S. I. Torgova, A. Strigazzi, N. Scaramuzza, C. Ferrero, I. P. Dolbnya, T. M. Weiss, R. Berardi, L. Muccioli, S. Orlandi and C. Zannoni, *Adv. Funct. Mater.*, 2009, **19**, 2592-2600.

14 G. Pelzl, A. Eremin, S. Diele, H. Kresse and W. Weissflog, *J. Mater. Chem.*, 2002, **12**, 2591-2593.

15 S. Taushanoff, K. Van Le, J. Williams, R. J. Twieg, B. K. Sadashiva, H. Takezoe and A. Jákli, *J. Mater. Chem.*, 2010, **20**, 5893–5898.

16 S.-T. Hur, M.-J. Gim, H.-J. Yoo, S.-W. Choi and H. Takezoe, *Soft Matter*, 2011, **7**, 8800–8803.

17 M. Cestari, S. Diez-Berart, D. A. Dunmur, A. Ferrarini, M. R. de la Fuente, D. J. B. Jackson, D. O. Lopez, G. R. Luckhurst, M. A. Perez-Jubindo, R. M. Richardson, J. Salud, B. A Timimi and H. Zimmermann, *Phys. Rev. E*, 2011, **84**, 031704.

18 L. Beguin, J. W. Emsley, M. Lelli, A. Lesage, G. R. Luckhurst, B. A. Timimi and H.

Zimmermann, *J. Phys. Chem. B*, 2012, **116**, 7940–7951.

19 V. P. Panov, M. Nagaraj, J. K. Vij, Yu. P. Panarin, A. Kohlmeier, M. G. Tamba, R. A. Lewis and G. H. Mehl, *Phys. Rev. Lett.*, 2010, **105**, 167801.

20 P. A. Henderson and C. T. Imrie, *Liq. Cryst.*, 2011, **38**, 1407-1414.

21 C.S.P. Tripathi, P. Losada-Pérez, C. Glorieux, A. Kohlmeier, M.-G.Tamba, G. H. Mehl and J. Leys, *Phys. Rev. E*, 2011, **84**, 041707.

22 K. Adlem, M. Čopič, G. R. Luckhurst, A. Mertelj, O. Parri, R. M. Richardson, B. D. Snow, B. A. Timimi, R. P. Tuffin and D. Wilkes, *Phys. Rev. E*, 2013, **88**, 022503.

23 R. B. Meyer, in *Molecular Fluids (Le Houches Summer School on Theoretical Physics* 1973), ed. R. Balian and G. Weill, Gordon and Breach, New York, 1976, pp. 271–343.

24 I. Dozov, *Europhys. Lett.*, 2001, **56**, 247–253.

25 R. Memmer, *Liq. Cryst.*, 2002, **29**, 483-496.

26 D. Chen, J. H. Porada, J. B. Hooper, A. Klittnick, Y. Shen, M. R. Tuchband, E. Korblova, D. Bedrov, D. M. Walba, M. A. Glaser, J. E. Maclennan and N. A. Clark, *Proc. Natl. Acad. Sci. U.S.A.*, 2013, **110**, 15931–15936.

27 V. Borshch, Y.-K. Kim, J. Xiang, M. Gao, A. Jakli, V. P. Panov, J. K. Vij, C. T. Imrie, M. G. Tamba, G. H. Mehl and O. D. Lavrentovich, *Nat. Commun.*, 2013, **4**, 2635.

28 C. Meyer, G. R. Luckhurst and I. Dozov, *J. Mater. Chem. C*, 2015, **3**, 318-328.

29 P. K. Challa, V. Borshch, O. Parri, C. T. Imrie, S. N. Sprunt, J. T. Gleeson, O. D. Lavrentovich and A. Jákli, *Phys. Rev. E*, 2014, **89**, 060501(R).

30 N. Sebastián, D. O. López, B. Robles-Hernández, M. R. de la Fuente, J. Salud, M. A. Pérez-Jubindo, D. A. Dunmur, G. R. Luckhurst and D. J. B. Jackson, *Phys. Chem. Chem. Phys.*, 2014, **16**, 21391

31 R. J. Mandle, E. J. Davis, S. A. Lobato, C. C. A. Voll, S. J. Cowling and J. W. Goodby, *Phys. Chem. Chem. Phys.*, 2014, **16**, 6907–6915.

32 P. S. Salter, C. Tschierske, S. J. Elston and E. P. Raynes, *Phys. Rev. E*, 2011, **84**, 031708.

33 R. Balachandran, V. P. Panov, J. K. Vij, A. Lehmann and C. Tschierske, *Phys. Rev. E*, 2013, **88**, 032503.

34 J. Harden, B. Mbanga, N. Éber, K. Fodor-Csorba, S. Sprunt, J. T. Gleeson and A. Jákli, *Phys. Rev. Lett.*, 2006, **97**, 157802.

35 M. Majumdar, P. Salamon, A. Jákli, J. Gleeson, S. Sprunt, *Phys. Rev. E*, 2011, **83**, 031701.

36 P. Sathyanarayana, M. Mathews, Q. Li, V. S. S. Sastry, B. Kundu, K. V. Le, H.

Takezoe and S. Dhara, *Phys. Rev. E*, 2010, **81**, 010702.

37 P. Tadapatri, U. S. Hiremath, C. V. Yelamaggad and K. S. Krishnamurthy, *J.Phys. Chem. B*, 2010, **114**, 1745 –1750.

38 N. Avci, V. Borshch, D. D. Sarkar, R. Deb, G. Venkatesh, T. Turiv, S. V. Shiyanovskii, N. V. S. Rao and O. D. Lavrentovich, *Soft Matter*, 2013, **9**, 1066 –1075.

39 V. Domenici, *Soft Matter*, 2011, **7**, 1589-1598.

40 Y. Jang, V. P. Panov, A. Kocot, A. Lehmann, C. Tschierske and J. K. Vij, *Phys. Rev. E*, 2011, **84**, 060701.

41 D. Wiant, J. T. Gleeson, N. Éber, K. Fodor-Csorba, A. Jákli, T. Tóth-Katona, *Phys. Rev. E*, 2005, **7**2, 041712.

42 S. M. Morris, M. J. Clarke, A. E. Blatch and H. J. Coles, *Phys. Rev. E.*, 2007, **75**, 041701.

43 K. L. Atkinson, S. M. Morris, F. Castles, M. M. Qasim, D. J. Gardiner and Harry J. Coles, *Phys. Rev. E*, 2012, **85**, 012701.

44 F. Castles, S. M. Morris, E. M. Terentjev and H. J. Coles, *Phys. Rev. Lett.*, 2010, **104**, 157801.

45 A. Jákli, *Liq. Cryst.*, 2010, **37**, 825-837.

46 T. D. Nguyen, S. Mao , Y.-W. Yeh , P. K. Purohit and M. C. McAlpine, *Adv. Mater.*, 2013, **25**, 946–974.

47 P. G. de Gennes and J. Prost, *The Physics of Liquid Crystals*, Clarendon Press, Oxford, 1993.

48 C. W. Oseen, *Trans. Faraday Soc.*, 1933, **29**, 883–889.

49 F. C. Frank, *Discuss. Faraday Soc.*, 1958, **25**, 19–28.

50 S. Singh, *Phys. Rep.*, 1996, **277**, 283–384.

51 A. Ferrarini, *Liq. Cryst.*, 2010, **37**, 811–823.

52 D.A. Dunmur, in *Physical Properties of Liquid Crystals*, ed. D. Dunmur, A. Fukuda and G. R. Luckhurst, Inspec, London, 2001, ch. 5.

53 M. R. Dodge, R. G. Petschek, C. Rosenblatt, M. E. Neubert and M. E. Walsh, *Phys. Rev. E*, 2003, **68**, 031703.

54 B. Kundu, R. Pratibha and N. V. Madhusudana, *Phys. Rev. Lett.*, 2007, **99**, 247802.

55 P. Sathyanarayana, B. K. Sadashiva and S. Dhara, *Soft Matter*, 2011, **7**, 8556 –8560.

56 *Flexoelectricity in Liquid Crystals: Theory, Experiments and Applications*, ed. Á. Buka and N. Éber, Imperial College Press, London, 2013.

57 R. B. Meyer, *Phys. Rev. Lett.*, 1969, **22**, 918-921.

58 J. Prost and J. P. Marcerou, *J. Phys. (France)*, 1977, **38**, 315-324.

59 A. G. Petrov, in *Physical Properties of Liquid Crystals*, ed. D. Dunmur, A. Fukuda and G. R. Luckhurst, Inspec, London, 2001, ch. 5.

60 F. Castles, S. C. Green, D. J. Gardiner, S. M. Morris and H. J. Coles, *AIP Adv.*, 2012, **2**, 022137.

61 Coles H. J., Musgrave B., Coles M. J., Willmott J. *J. Mater. Chem.* **2001**, *11*, 2709.

62 K. V. Le, F. Araoka, K. Fodor-Csorba, K. Ishikawa and H. Takezoe, *Liq. Cryst.* 2009, **36**, 1119-1124.

63 (a) F. Castles, S. M. Morris and H. J. Coles, *AIP Advances*, 2011, **1**, 032120. (b) P. Palffy-Muhoray, *AIP Advances*, 2013, **3**, 019101. (c) F. Castles, S. M. Morris and H. J. Coles, *AIP Advances*, 2013, **3**, 019102.

64 A. Ferrarini, C. Greco and G.R. Luckhurst, *J. Mater. Chem.*, 2007, **17**, 1039–1042.

65 J. S. Patel and R. B. Meyer, *Phys. Rev. Lett.*, 1987, **58**, 1538-1540.

Part I

Chapter 3

A generalised Maier-Saupe theory for the N_{TB}-N phase transition*

3.1 Introduction

As described in Chapter 2, recent experiments have shown that, on cooling, liquid crystals of bent-shaped molecules can undergo a transition from the conventional nematic phase (N) to another kind of nematic phase, called a twist-bend nematic (N_{TB}) [1]: this is chiral, with doubly degenerate handedness, spontaneously bent, and locally polar, being characterized by a periodically distorted director $\hat{\mathbf{n}}$ forming a conical helix, with conical angle θ_0 and helical pitch p.

Although the structural features of the N_{TB} phase are becoming progressively clear, the origin of the direction modulation is not completely understood. The N_{TB} organization was theoretically predicted several years before its experimental observation, and two different mechanisms were proposed [2,3]. According to Meyer's theory [2], spontaneous bend distorsions of the director could result from the gain in free energy density $f_{\text{flexo}}^{\text{bend}}$ associated with flexoelectric couplings:

$$f_{\text{flexo}}^{\text{bend}} \propto -\mathbf{P}\cdot\mathbf{B} \quad , \tag{3.1}$$

where $\mathbf{P}$ is the electric polarization and $\mathbf{B}=(\nabla\times\hat{\mathbf{n}})\times\hat{\mathbf{n}}$ is the vector defining the bend deformation, which is perpendicular to $\hat{\mathbf{n}}$ (Figure 2.4(c)).

A different mechanism was proposed by Dozov [3], who speculated that in liquid

* This Chapter is adapted from: C. Greco, G. R. Luckhurst and A. Ferrarini, *Soft Matter*, 2014, **10**, 9318-9323. © 2014 The Royal Society of Chemistry

crystals of bent-shaped molecules the bend elastic constant K_{33} can become negative: the N_{TB} organization would thus become stable as a result of an elastic instability. Considering one-dimensional modulations of the director, $\hat{\mathbf{n}} = \hat{\mathbf{n}}(Z)$, Dozov proposed the following expression for the deformation free energy density [3]:

$$f_{\text{def}} = \frac{1}{2}\left(K_{11}\mathbf{S}^2 + K_{22}T^2 + K_{33}\mathbf{B}^2\right) + f_4 \ . \tag{3.2}$$

The first term in Eq. (3.2) is the usual Frank expression of the elastic free energy density (Eq. 2.1). The term f_4 contains spatial derivatives of the director up to fourth order in the expansion and it is assumed to be always positive, thus ensuring that, even for $K_{33} < 0$, the elastic energy is bounded from below. The twist-bend field is a possible solution which minimizes the free energy in Eq. (3.2); another solution corresponds to a splay-bend modulation [3]. Negative K_{33} values for nematics of bent molecules have been predicted either for purely steric reasons [4] or as result of flexoelectric renormalization [5], using respectively a molecular field theory with atomistic modelling and a Landau approach. The meaning of these predictions has been widely debated.

In addition to the origin of the N_{TB} phase, another aspect which needs clarification is the relationship between the formation of this phase and the molecular structure [1,6-9]. Continuum models alone are not adequate for this purpose and a molecular based approach is needed.

Here we present a molecular field theory for the N_{TB} phase. Considering the case of rigid, V-shaped molecules, a minimalist model is used, which can be seen as a generalization of the Maier–Saupe theory† suitable to take account of both the molecular architecture and the twist-bend spatial modulation of the director. Thus we obtain an expression for the free energy where the distinctive features of the system are introduced from the molecular level, rather than as ad hoc parameters. This allows us to obtain a consistent picture of the N and N_{TB} phases, of their transitional and elastic behaviour, in relation to the molecular geometry. In the next section we will give an overview of the model, then we will present the theoretical predictions and we will discuss them in the light of the available experimental data. Finally, we summarise the

† The Maier-Saupe theory was outlined in Chapter 1.

significant conclusions of our study and make comparisons with other theories.

3.2 The molecular field model

The molecular model is sketched in Figure 3.1(a): a molecule is made of two mesogenic arms (A and B), each of length *L*, joined at one end, with the bend angle χ. The following unit vectors are attached to the molecule: $\hat{\mathbf{w}}$ is parallel to the C_2 (molecular) symmetry axis and $\hat{\mathbf{u}}_A, \hat{\mathbf{u}}_B$ are along the arms.

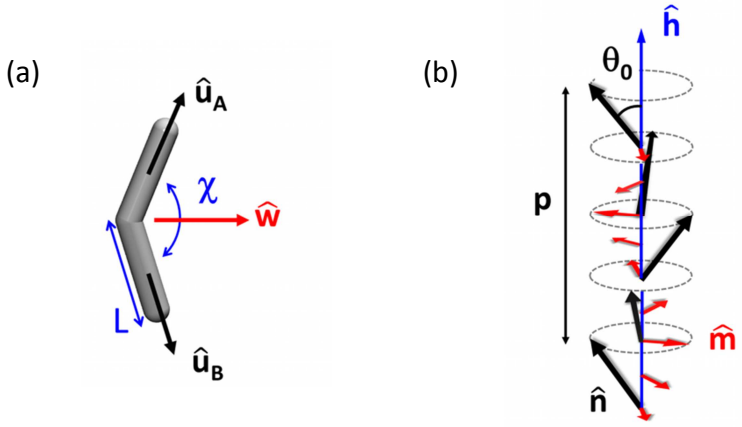

Figure 3.1. (a) The molecular model, with χ the bend angle and *L* the length of one arm; $\hat{\mathbf{w}}$, $\hat{\mathbf{u}}_{A,B}$ are unit vectors parallel to the two-fold symmetry axis and to the arms, respectively. (b) The N_{TB} phase organization (one of the two degenerate helicoidal domains) with θ_0 the conical angle and *p* the helical pitch; $\hat{\mathbf{n}}$ and $\hat{\mathbf{h}}$ are unit vectors parallel to the local director and to the helix axis, respectively, and $\hat{\mathbf{m}} = \hat{\mathbf{h}} \times \hat{\mathbf{n}}$.

The classic N phase is characterized by a uniform director $\hat{\mathbf{n}}$, whereas, according to the customary description, each chiral domain of the N_{TB} phase features a director that undergoes a heliconical precession around an axis (parallel to the unit vector $\hat{\mathbf{h}}$), with conical angle θ_0 and pitch *p*, or wavenumber $q = 2\pi / p$ (see Figure 3.1(b)). In a laboratory frame with the *Z* axis parallel to the helix axis we can then write:

$$\hat{\mathbf{n}} = \hat{\mathbf{n}}(Z) = \left(\sin\theta_0 \cos\phi, \sin\theta_0 \sin\phi, \cos\theta_0\right) \quad , \tag{3.3}$$

where $\phi = qZ$. The uniaxial nematic phase is recovered for pitch $p \to \infty$ and/or conical angle θ_0 = 0°, whereas the case with finite pitch and θ_0 = 90° corresponds to the

cholesteric[‡] organization. In the spirit of the Maier–Saupe theory, each arm is assumed to align preferentially to the local director $\hat{\mathbf{n}}$ at the position of the arm. Thus, the complete orientational potential experienced by the molecule, U^{or}, is the sum of the contributions of the two arms:

$$U^{or} = -c\langle P_2\rangle\left[P_2\left(\hat{\mathbf{u}}_{\mathrm{A}}\cdot\hat{\mathbf{n}}(\mathbf{R}_{\mathrm{A}})\right)+P_2\left(\hat{\mathbf{u}}_{\mathrm{B}}\cdot\hat{\mathbf{n}}(\mathbf{R}_{\mathrm{B}})\right)\right] \quad , \tag{3.4}$$

where c is a constant (with the dimension of energy) that quantifies the orienting strength, P_2 is the second Legendre polynomial, $\hat{\mathbf{n}}(\mathbf{R}_J)$ is the director at the position of the midpoint of the Jth arm (J = A, B), and $\langle P_2\rangle$ is the orientational order parameter of an arm. It is worth pointing out that the orientational potential U^{or} defined in Eq. (3.4) depends on a microscopic order parameter ($\langle P_2\rangle$) and two macroscopic order parameters (θ_0 and p) which characterize the position dependence of the director field. For the special case of rod-like molecules (χ=180°) and uniform $\hat{\mathbf{n}}$ (*i.e.* $p\to\infty$), the Maier–Saupe expression is recovered [12] (apart from a factor of 2, which results from considering the molecule as made of two mesogenic units). The molecular field potential defined in Eq. (3.4) is a function of the molecular orientation: $U^{or} = U^{or}(\Omega)$, where $\Omega = \{\alpha, \beta, \gamma\}$ are Euler angles that define this orientation in a local frame with its Z' axis parallel to $\hat{\mathbf{n}}$. Orientational averages can then be defined as:

$$\langle ... \rangle = \int ... f(\Omega) d\Omega \quad , \tag{3.5}$$

where $f(\Omega)$ is the single molecule orientational distribution function:

$$f(\Omega) = \frac{1}{Q}\exp\left[-U^{or}(\Omega)/k_{\mathrm{B}}T\right] \quad , \tag{3.6}$$

with k_{B} the Boltzmann constant, T the temperature and Q the orientational partition function:

$$Q = \int \exp\left[-U^{or}(\Omega)/k_{\mathrm{B}}T\right] d\Omega \quad . \tag{3.7}$$

[‡] Unlike most literature, here "chiral nematic" will not be used as a synonym of cholesteric, since this could be ambiguous after the identification of other chiral nematic phases [10,11].

By construction the potential $U^{or}(\Omega)$ reflects the symmetry of the molecule and that of its local environment. The N_{TB} structure has global D_∞ symmetry, with the C_∞ axis parallel to the helix axis ($\hat{\mathbf{h}}$ in Figure 3.1(b)), and local C_2 symmetry, with the twofold axis perpendicular to the plane containing the helix axis and the local $\hat{\mathbf{n}}$ director, i.e. along $\hat{\mathbf{m}}$ in Figure 3.1(b). Therefore the N_{TB} phase is locally polar: it is compatible with the existence of odd-rank order parameters, defined with respect to the $\hat{\mathbf{m}}$ axis, which is the only principal direction common to any locally averaged property.

According to the molecular field procedure the Helmholtz free energy of the liquid crystal phase, taken as the difference with respect to that of the isotropic phase, is built as the sum of an entropy and an internal energy contribution, both expressed in terms of the molecular field orientational potential [13]. The N_{TB} phase, though non-uniform, is homogeneous; thus for both the N and the N_{TB} phases we can simply refer to thermodynamic properties per unit volume. The change in entropy density resulting from orientational order is given by: $\Delta s^{or} = -\rho k_B \int \ln\left[8\pi^2 f(\Omega)\right] f(\Omega) d\Omega$, where ρ is the number density, $\rho = N/V$, with N the number of molecules and V the volume. The change in internal energy density is simply related to the average value of the molecular field potential: $\Delta u^{or} = (\rho/2)\langle U^{or} \rangle$, where again the angular brackets denote the orientational averages defined previously. Then, we obtain for the entropic term:

$$\Delta s^{or} = -2\rho \frac{c}{T} \langle P_2 \rangle^2 + \rho k_B \ln \frac{Q}{8\pi^2} \ , \tag{3.8}$$

and for the internal energy contribution:

$$\Delta u^{or} = -\rho c \langle P_2 \rangle^2 \quad . \tag{3.9}$$

We can then define the scaled Helmholtz free energy density as:

$$\Delta a^* = \frac{\Delta a}{\rho k_B T} = \left\{ \frac{\langle P_2 \rangle^2}{T^*} - \ln \frac{Q}{8\pi^2} \right\} \ , \tag{3.10}$$

with the scaled temperature $T^* = k_B T / c$. A key feature of the free energy density in Eq. (3.10) is that it implicitly contains the position dependence of the director, through the

potential of mean torque, Eq. (3.4). Thus, it represents the free energy density of the nematic phase with the director field $\hat{\mathbf{n}}(\mathbf{R})$, relative to the isotropic phase. At a given scaled temperature, this difference is a function of the director deformation and of the $\langle P_2 \rangle$ orientational order parameter. Conversely, if a parametric form of the director field is used, the equilibrium state can be obtained by minimization of the free energy density, Eq. (3.10), with respect to $\langle P_2 \rangle$ and the director field parameters (θ_0 and p, or q, for the N_{TB} phase). We can define the deformation free energy density at a given temperature as the difference between the free energy density of the deformed (Δa^*) and the undeformed (Δa_u^*) system:

$$\Delta a_{def}^* = \Delta a^* - \Delta a_u^* \quad . \tag{3.11}$$

Calculation of this difference as a function of the principal modes of deformation, defined with respect to the equilibrium state, allows us to determine the elastic constants, as will be shown later.

3.3 Results and discussion

We have investigated the phase behaviour of V-shaped molecules with different values of the bend angle χ. In our calculations the arm length L is taken as the unit of length. Figure 3.2 shows a set of molecular orientational order parameters and the conical angle and pitch in the N_{TB} phase, calculated for χ = 150°, 140°, 135° and 130°. They are reported as a function of the reduced temperature $T_{red} = T / T_{NI}$, where T_{NI} is the nematic–isotropic transition temperature. For χ = 140° and χ =135° we can see a first order transition from the isotropic to the uniaxial nematic phase, marked by a jump to a finite value of the $\langle P_2 \rangle$ order parameter, followed by a second order transition, from the N to the N_{TB} phase, at a lower temperature. This is evidenced by a discontinuous change in slope of $\langle P_2 \rangle$, and a simultaneous appearance of a conical angle and a finite pitch. Correspondingly, the onset of polar order is evidenced by the first rank order parameter $\langle P_1^{wm} \rangle$, with $P_1^{wm} = \hat{\mathbf{w}} \cdot \hat{\mathbf{m}}$. Both conical angle and pitch exhibit a steep change at the N_{TB}–N transition, reaching values that then remain almost constant with decreasing

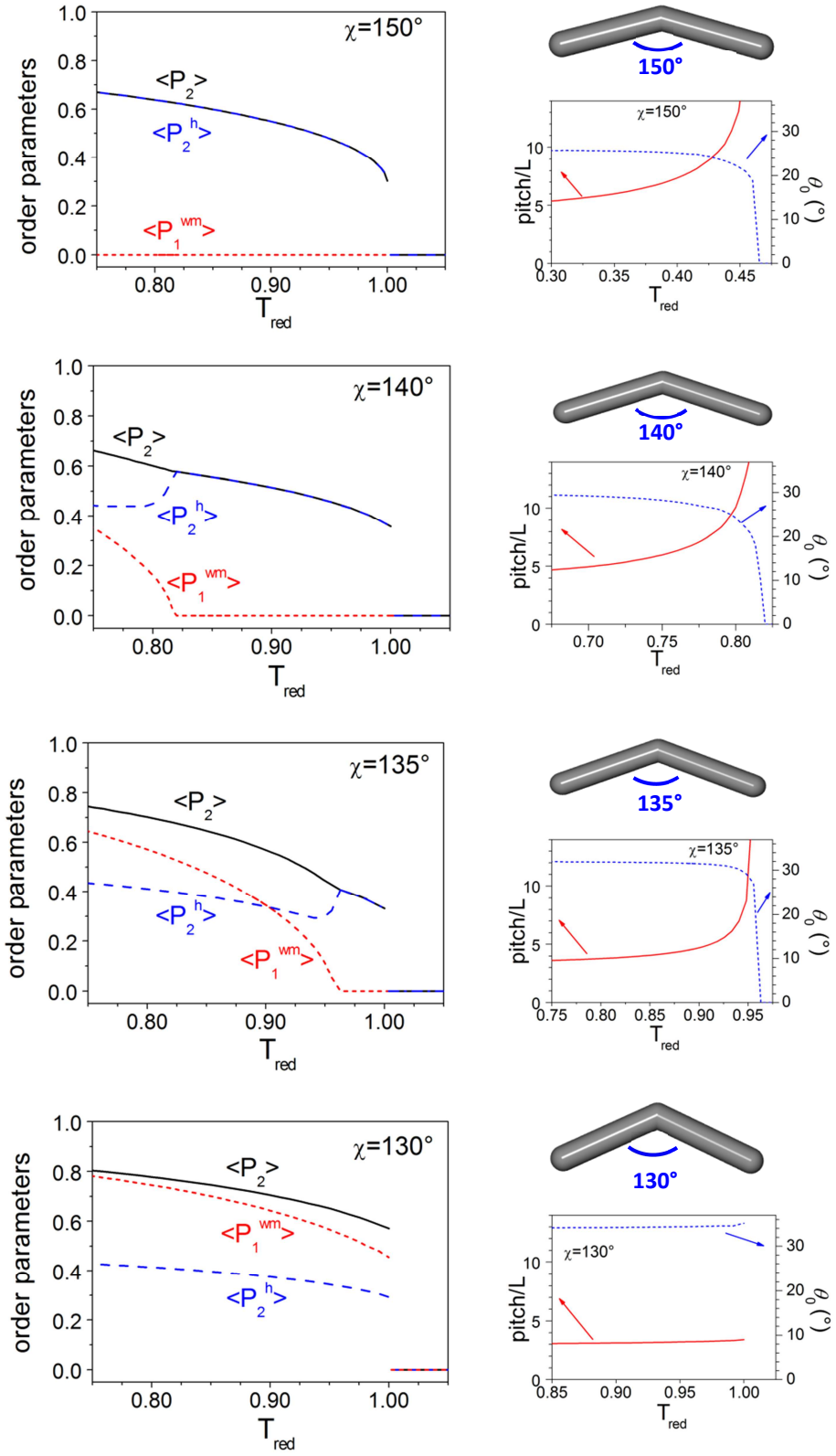

Figure 3.2 Molecular order parameters (see text), on the left, and helical pitch p and conical angle θ_0, on the right, as a function of the reduced temperature T_{red}, for V-shaped molecules with bend angle χ= 150°, 140°,135°,130° (from top to bottom).

temperature: θ_0 around 30° and $p \sim 4$–$5L$. In the plots we also show the second rank order parameter $\left\langle P_2^{\mathrm{h}} \right\rangle$, for the molecular arms with respect to the helix axis $\hat{\mathbf{h}}$. In the N phase, where there is no tilt, this is identical to $\left\langle P_2 \right\rangle$, but at the N_{TB}–N transition a difference appears, since the former exhibits a drop, which is a signature of the tilt of the $\hat{\mathbf{n}}$ director, and then increases very slowly with decreasing temperature. For χ larger than 150° the N_{TB}–N transition is predicted at a very low temperature ($T_{NI} / T_{N_{TB}N} > 2$). Surprisingly for χ = 130° we can see a direct first order transition from the isotropic to the N_{TB} phase, denoted by a jump to finite values of the conical angle, the helical pitch and of all the orientational order parameters. These results point to a strong sensitivity of the phase behaviour to the bend angle: as χ becomes smaller so the width of the N phase decreases and the N_{TB} phase is progressively stabilized. Unlike the stability range of the N phase, the structural properties of the N_{TB} phase exhibit only a weak dependence upon the χ value: interestingly in all cases a tight pitch is predicted, of the order of a few molecular lengths, which decreases slightly with narrowing of the bend angle, whereas the conical angle tends to increase.

Figure 3.3 shows the scaled deformation free energy density, $\Delta a_{\mathrm{def}}^{*}$, as a function of helical wavenumber and conical angle for χ = 140° at three different reduced temperatures, on either side of the N_{TB}–N phase transition.

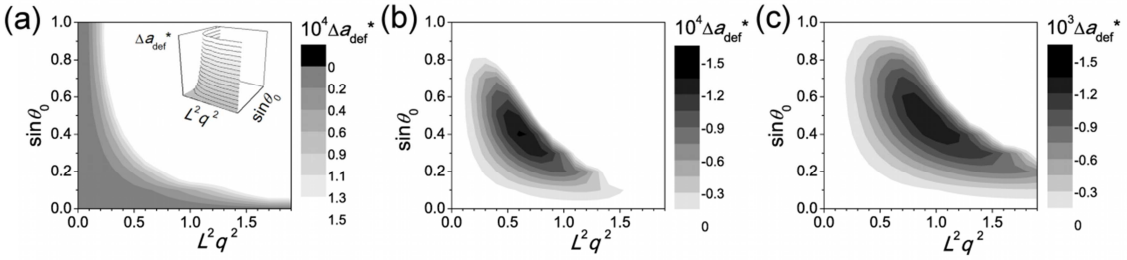

Figure 3.3 Contour plots showing the scaled deformation free energy density $\Delta a_{\mathrm{def}}^{*}$ as a function of the square of the wavenumber q (L is taken as the unit of length) and of $\sin\theta_0$, with θ_0 being the conical angle. Calculations are for molecules with bend angle χ = 140°, at three different reduced temperatures on either side of the N_{TB}–N phase transition: T_{red} = 0.83 (a), 0.80 (b) and 0.77 (c). The inset in the (a) graph shows a 3D representation of the free energy surface.

At the higher temperature the free energy exhibits a single minimum, at q = 0, $\sin\theta_0$ = 0, *i.e.* in the N phase, and increases as the deformation grows. On decreasing temperature

the minimum becomes shallower until a new minimum appears, at finite values of q and $\sin\theta_0$. Then, on further decreasing temperature the minimum becomes deeper and moves toward higher θ_0 and q values.

According to the continuum elastic theory, the free energy density of the nematic phase in the presence of a twist-bend deformation ($q \to 0$) can be expressed as [14]:

$$\Delta a_{\text{def}} = \frac{1}{2} K_{22} q^2 \sin^4 \theta_0 + \frac{1}{2} K_{33} q^2 \sin^2 \theta_0 \cos^2 \theta_0 \quad , \tag{3.12}$$

where K_{22} and K_{33} are the twist and bend elastic constants, respectively. For $\theta_0 = 90°$ the deformation is a pure twist, whereas for $\theta_0 = 0°$ the energetic cost is essentially that for bend. Therefore we can write:

$$\Delta a_{\text{def}} = \frac{1}{2} K_{22} q^2 \qquad \text{for } \theta_0 = 90° \quad , \tag{3.13}$$

$$\Delta a_{\text{def}} / \sin^2 \theta_0 = \frac{1}{2} K_{33} q^2 \qquad \text{for } \theta_0 \to 0° \quad . \tag{3.14}$$

Thus, from the initial slope ($q \to 0$) of Δa_{def} *vs.* q^2 we can obtain the twist and bend elastic constants of the N phase. This is different from the common methodology, in which explicit expressions for the elastic constants are used [15].

For pure twist, the deformation free energy is an increasing function of q and its initial slope remains positive over the whole temperature range. For bend deformations we find a more complex behaviour, as illustrated in Figure 3.4. This shows the ratio $\Delta a^*_{\text{def}} / \sin^2 \theta_0$ calculated for $\theta_0 \to 0°$ as a function of q^2, for the case $\chi = 140°$. Data for a set of temperatures are reported, on either side of the N_{TB}–N phase transition. Above the transition the deformation free energy for pure bend is positive and proportional to q^2; however, unlike the usual behaviour for rod-like nematics, the initial slope, and hence K_{33}, decreases with decreasing temperature. On going through the N_{TB}–N transition, the slope reverses its sign, simultaneously with the disappearance of the nematic minimum. Analogous results were obtained using a different methodology and a molecular field model with atomistic resolution [4,16], for both bent-core mesogens and odd liquid crystal dimers having an average bent shape: the bend elastic constant K_{33} was found to decrease with increasing order, and then to take negative values.

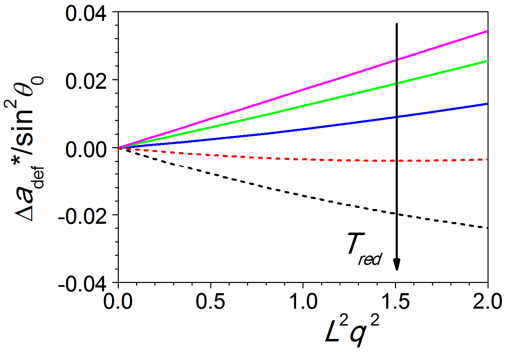

Figure 3.4 Scaled deformation free energy density for pure bend as a function of the square of the wavenumber q (L is taken as the unit of length), for particles with bend angle χ=140° at different reduced temperatures (T_{red} = 0.90, 0.87, 0.83, 0.80, 0.77). Solid(/short-dashed) lines are used for values predicted at temperatures above (/below) the N_{TB}-N transition.

It is worth stressing that in this context K_{33} is meant as a synonym of 'second derivative of the free energy with respect to bend deformations', and only if positive does it have the meaning of a standard elastic modulus associated with a restoring force.

Our results are in keeping with the main experimental findings on the N_{TB} phase. These include the key role of the bend angle: the N_{TB} phase has been detected in liquid crystal dimers with an odd number of groups between the mesogenic units and its appearance exhibits a strong sensitivity to molecular modifications [1,6-9]. In these systems the bend angle, taken as the angle between the mesogenic units, changes with the molecular conformation. The bend angle distribution for a given dimer has a subtle dependence on the nature of the linking group between the mesogenic units and the spacer, being shifted to larger values on moving from methylene to ether links [1,4]. Up to now there is no evidence of a direct N_{TB}–I transition; according to our predictions good candidates would be systems with a small bend angle, for which however there could be other competing phases. From FFTEM [17,18], birefringence experiments [17-20], analysis of NMR spectroscopy data [21,22] and measurements of an electroclinic effect [23] , conical angles between 11° and 30°, together with pitches in the range 5–10 nm and weakly dependent on temperature, have been determined for CB7CB and other odd liquid crystal dimers of similar structure (average molecular lengths 2.5–3 nm). A slightly longer pitch, of 14 nm, was reported for a bent-core mesogen (average molecular length 5 nm) [24]. The birefringence, which in the N phase is found to increase with lowering temperature, exhibits a decrease on entering the N_{TB} phase,

which was interpreted as evidence for a tilt of the director. A strong decrease was observed at the N_{TB}–N transition for CB7CB and for a mixture of liquid crystal dimers [17,19,20] but for another odd mesogenic dimer a smoother decrease was found [18]. A qualitative comparison can be made with the temperature dependence of the $\left\langle P_2^{\mathrm{h}} \right\rangle$ order parameter (Figure 3.2). A great deal of information on the N_{TB} phase has been provided by NMR spectroscopy, however the molecular representation used in our present model is not sufficiently detailed to allow an accurate comparison with NMR data. Finally, we have to mention the anomalous behaviour of the bend elastic constant in the N phase: for odd liquid crystal dimers K_{33} has been found to be unusually small and to decrease on moving towards the transition with the N_{TB} phase, up to very small values in the proximity of the transition [7,18] although in one case a plateau was observed [25].

The ability to investigate on the same footing different phases and properties allows us to clarify some controversial issues. One is the relationship between the phase transition and the elastic properties. We have found that for sufficiently bent molecules, as the temperature decreases, the N free energy minimum broadens along the bend coordinate, until a new minimum appears, which corresponds to the N_{TB} phase. This behaviour can be described in terms of elastic constants, *i.e.* the principal curvatures of the free energy at its minimum: K_{33} in the N phase decreases, until vanishing, as the temperature is lowered. When $K_{33} = 0$ the director can bend without cost and the twist-bend organization appears. With further decreasing of temperature the curvature of the free energy in the undeformed (N) state with respect to bend deformations becomes increasingly negative and the N_{TB} minimum becomes deeper. A few points are worth stressing. The N_{TB} phase has its own elastic properties, different from those of the N phase; thus, in principle the use of the classical Frank free energy to analyse experiments in the N_{TB} phase is not justified, and could lead to questionable conclusions [26]. Recently, extensions of the Frank elastic theory to the N_{TB} phase have been proposed, one of which contains a quartic term [3] whereas the other retains the quadratic form [27]. Another issue that deserves attention is the concept of 'negative K_{33}', which should be meant as negative curvature of the free energy in the undeformed N state with respect to bend deformations. As such it indicates that the N phase is unstable with respect to bend deformations [4,7,15].

3.4 Conclusions

We have shown that a generalized Maier–Saupe theory, modified to take into account the coupling between director field and molecular shape, predicts the existence of the N_{TB}–N transition. This means that, compared to the N phase, the N_{TB} organization allows a better interaction between the noncollinear mesogenic groups, which compensates for the loss of entropy due to the additional polar order. Differently from previous theoretical approaches [3,5] our model includes molecules explicitly, though in a rather basic form, so that we can assess the effect of changes in the molecular structure on the phase behaviour. We show that this is especially sensitive to the molecular bend angle, with the N_{TB}–N transition occurring for a limited range of values. We predict the orientational and structural parameters of the N_{TB} phase and their temperature dependence; in particular, we obtain a pitch of the order of a few molecular lengths, weakly dependent on temperature or molecular details, in agreement with the available experimental data. We can also provide a consistent description of the elastic properties of the system, which allows us to discuss their relationship with the N_{TB}–N transition. In this regard, the scenario that we describe is in substantial agreement with the Dozov picture, though from a different perspective. Elsewhere electrostatics, and in particular flexoelectric couplings, have been proposed as the main feature responsible for the formation of modulated phases [2,28]. One cannot, of course, exclude that such couplings are present and may also be more significant than in conventional rod-like nematics, but this does not necessarily mean that they are the driving force for the phase transition. Interestingly, the N_{TB} phase has been observed experimentally even for mesogens that lack strong electric dipoles [18]. Indeed, the results predicted by our model point towards a primary role of the molecular shape, in line with the suggestion of early Monte Carlo simulations [29] and also with more recent lattice simulations [5]. In the latter the site interactions leading to the twist-bend modulation were denoted as ‘dipolar’ or ‘flexoelectric’ but, given the model used, this has to be taken more as a general indication of their symmetry, rather than of their physical nature, as clarified also by the author themselves [30].

Our present study can be extended along various directions. One is the introduction of a more detailed molecular representation, along the lines shown in Ref. [4] and [16], which will allow closer comparison of the predictions with experimental data, in

particular with those from NMR spectroscopy [21,22]. Another is the extension to different phases, having not only 1D periodicity, like the predicted splay–bend nematic [3], but even 2D and 3D modulations [30]. This is especially important in view of the well-known difficulties of molecular simulations of finite samples in handling non-uniform systems. Also the use of free energy calculations in the presence of director deformations, as proposed here, to evaluate the elastic constants, is a general methodology that clearly merits exploration.

3.5 References

1 M. Cestari, S. Diez-Berart, D. A. Dunmur, A. Ferrarini, M. R. de la Fuente, D. J. B. Jackson, D. O. Lopez, G. R. Luckhurst, M. A. Perez-Jubindo, R. M. Richardson, J. Salud, B. A Timimi and H. Zimmermann, *Phys. Rev. E*, 2011, **84**, 031704.

2 R. B. Meyer, in *Molecular Fluids (Le Houches Summer School on Theoretical Physics* 1973), ed. R. Balian and G. Weill, Gordon and Breach, New York, 1976, pp. 271–343.

3 I. Dozov, *Europhys. Lett.*, 2001, **56**, 247–253.

4 M. Cestari, E. Frezza, A. Ferrarini and G. R. Luckhurst, *J. Mater. Chem.*, 2011, **21**, 12303-12308.

5 S. M. Shamid, S. Dhakal and J. V. Selinger, *Phys. Rev. E*, 2013, **87**, 052503.

6 P. A. Henderson and C. T. Imrie, *Liq. Cryst.*, 2011, **38**, 1407-1414.

7 K. Adlem, M. Čopič, G. R. Luckhurst, A. Mertelj, O. Parri, R. M. Richardson, B. D. Snow, B. A. Timimi, R. P. Tuffin and D. Wilkes, *Phys. Rev. E*, 2013, **88**, 022503.

8 R. J. Mandle, E. J. Davis, S. A. Lobato, C. C. A. Voll, S. J. Cowling and J. W. Goodby, *Phys. Chem. Chem. Phys.*, 2014, **16**, 6907–6915.

9 N. Sebastián, D. O. López, B. Robles-Hernández, M. R. de la Fuente, J. Salud, M. A. Pérez-Jubindo, D. A. Dunmur, G. R. Luckhurst and D. J. B. Jackson, *Phys. Chem. Chem. Phys.*, 2014, **16**, 21391

10 E. Barry, Z. Hensel, Z. Dogic, M. Shribak and R. Oldenbourg, *Phys. Rev. Lett.*, 2006, **96**, 018305.

11 H. B. Kolli, E. Frezza, G. Cinacchi, A. Ferrarini, A. Giacometti and T. S. Hudson, *J. Chem. Phys.*, 2014, **140**, 081101.

12 (a) W. Maier and A. Saupe, *Z. Naturforsch. A*, 1958, **13**, 564–566. (b) W. Maier and A. Saupe, *Z. Naturforsch. A.*, 1959, **14**, 882–889. (c) W. Maier and A. Saupe, *Z. Naturforsch. A* , 1960, **15**, 287–292.

13 G. R. Luckhurst, in *The Molecular Physics of Liquid Crystals*, ed. G. R. Luckhurst and G. W. Gray, Academic Press, 1979, ch. 4.

14 P. G. de Gennes and J. Prost, *The Physics of Liquid Crystals*, Clarendon Press, Oxford, 1993.

15 A. Ferrarini, *Liq. Cryst.*, 2010, **37**, 811–823.

16 C. Greco, A. Marini, E. Frezza and A. Ferrarini, *ChemPhysChem*, 2014, **15**, 1336-1344.

17 D. Chen, J. H. Porada, J. B. Hooper, A. Klittnick, Y. Shen, M. R. Tuchband, E. Korblova, D. Bedrov, D. M. Walba, M. A. Glaser, J. E. Maclennan and N. A. Clark, *Proc. Natl. Acad. Sci. U.S.A.*, 2013, **110**, 15931–15936.

18 V. Borshch, Y.-K. Kim, J. Xiang, M. Gao, A. Jakli, V. P. Panov, J. K. Vij, C. T. Imrie, M. G. Tamba, G. H. Mehl and O. D. Lavrentovich, *Nat. Commun.*, 2013, **4**, 2635.

19 C. Meyer, G. R. Luckhurst and I. Dozov, *J. Mater. Chem. C*, 2015, **3**, 318-328.

20 P. K. Challa, V. Borshch, O. Parri, C. T. Imrie, S. N. Sprunt, J. T. Gleeson, O. D. Lavrentovich and A. Jákli, *Phys. Rev. E*, 2014, **89**, 060501(R).

21 L. Beguin, J. W. Emsley, M. Lelli, A. Lesage, G. R. Luckhurst, B. A. Timimi and H. Zimmermann, *J. Phys. Chem. B*, 2012, **116**, 7940–7951.

22 C. Greco, G. R. Luckhurst and A. Ferrarini, *Phys. Chem. Chem. Phys.*, 2013, **15**, 14961-14965.

23 C. Meyer, G. R. Luckhurst and I. Dozov, *Phys. Rev. Lett.*, 2013, **111**, 067801.

24 D. Chen, M. Nakata, R. Shao, M. R. Tuchband, M. Shuai, U. Baumeister, W. Weissflog, D. M. Walba, M. A. Glaser, J. E. Maclennan and N. A. Clark, *Phys. Rev. E*, 2014, **89**, 022506.

25 R. Balachandran, V. P. Panov, J. K. Vij, A. Kocot, M. G. Tamba, A. Kohlmeier and G. H. Mehl, *Liq. Cryst.*, 2013, **40**, 681–688.

26 V. P. Panov, M. Nagaraj, J. K. Vij, Yu. P. Panarin, A. Kohlmeier, M. G. Tamba, R. A. Lewis and G. H. Mehl, *Phys. Rev. Lett.*, 2010, **105**, 167801.

27 E. G. Virga, *Phys. Rev. E*, 2014, **89**, 052502.

28 N. Vaupotič, M. Čepič, M. A. Osipov and E. Gorecka, *Phys. Rev. E*, 2014, **89**, 030501.

29 R. Memmer, *Liq. Cryst.* 2002, **29**, 483-496.

30 S. M. Shamid, D. W. Allender and J. V. Selinger, *Phys. Rev. Lett.*, 2014, **113**, 237801.

Part II

Chapter 4

Molecular Dynamics simulations of bent-shaped particles

4.1 Introduction

In the previous Chapter, the nematic (N) to twist-bend nematic (N_{TB}) phase transition was investigated by molecular field theory. To further check the formation of a N_{TB} organization and its molecular determinants, and to characterize the molecular organization in the N_{TB} phase, we performed Molecular Dynamics simulations of rigid, achiral, apolar bent-shaped particles interacting via a purely repulsive potential.

Computer simulations of bent-shaped particles are still relatively scarce. In these studies, different simulation techniques and molecular models have been used to explore and understand the effect of the bent molecular shape on the phase behaviour. The majority of them are off-lattice Monte Carlo (MC) or Molecular Dynamics (MD) simulations using generic coarse-grained molecular models [1-13]. Particles having a bent shape were built by joining anisotropic interaction sites, such as soft or hard spherocylinders [1-3] or Gay-Berne ellipsoids [4-9], or chains of spherical interaction sites [10-13]. Particles with different bend angles were studied, with or without electric dipoles. A few atomistic MD simulations have also been performed, for a bent-core oxadiazole compound [14] and for the liquid crystalline dimer CB7CB [15]. Finally, a couple of works using on-lattice MC simulations can also be found in the literature [16, 17].

The earlier computational studies were motivated mainly by the interest in the unconventional smectic phases of bent-shaped molecules (see Chapter 2) [2,4-7,10-12]. In addition, bent molecules appeared to be good candidates for the formation of the long sought-after biaxial nematic phase [2,7,14,16]. Computer simulations specifically

devoted to the investigation of the uniaxial nematic phase of bent-shaped molecules have appeared only recently, following the experimental discovery that also this phase exhibits unconventional properties. In the work of Peroukidis *et al.* [3] and Francescangeli *et al.* [9] the model bent-shaped particles were found to exhibit short-range positional and orientational correlations, taken as an indication of a uniaxial nematic phase made of smectic-like cybotactic clusters with local polar order. Interestingly, in Ref. [3] right-handed and left-handed twisted nematic organizations were also found, resulting from the arrangement of cybotactic clusters into a cholesteric-like helix. These twisted organizations formed only if some degree of molecular flexibility was included in the model, allowing for the existence of chiral molecular conformations.

Of particularly relevance to the present work are the results obtained by Memmer [4], who, in addition to the conventional nematic (N) phase, observed an unusual nematic organization, having the characteristics of a twist-bend N_{TB} phase (see Chapter 2) [18]. Such an organization was observed only in a single simulation run, and the author pointed out the need for further studies. The works of Chen *et al.* [15] and Shamid *et al.* [17] support the early results obtained by Memmer, though by the use of different models: in both cases a N_{TB} organization was evidenced.

The molecular model used in the simulations performed in this thesis will be introduced in the next section. In Section 4.3 and 4.4 we will outline the details of the simulation procedure and define the structural indicators used to characterize the phase organization. The results obtained will be presented in Section 4.5 and finally the main conclusion of this preliminary investigation will be summarized.

4.2 The molecular model

A bent-shaped molecule is modelled as a chain of N_b=11 identical interaction sites (hereafter called “beads”), rigidly connected to each other to form a particle of C_{2v} symmetry. Beads belonging to different molecules interact via the WCA repulsive potential [19]:

$$V(r_{pq}) = \begin{cases} 4\varepsilon\left[\left(\frac{\sigma}{r_{pq}}\right)^{12} - \left(\frac{\sigma}{r_{pq}}\right)^{6}\right] + \varepsilon & r_{pq} < 2^{1/6}\sigma \\ 0 & r_{pq} \geq 2^{1/6}\sigma \end{cases} , \qquad (4.1)$$

where $r_{pq} = |\mathbf{r}_p - \mathbf{r}_q|$ is the distance between the *p*th and *q*th beads, located at position $\mathbf{r}_p$ and $\mathbf{r}_q$, and σ and ε are the characteristic length and energy scales of the interaction, respectively (Figure 4.1). In the rest of this Chapter all quantities will be expressed in reduced units, obtained by setting σ as the unit of length, ε as the unit of energy and the mass *m* of a bead as the unit of mass [19].

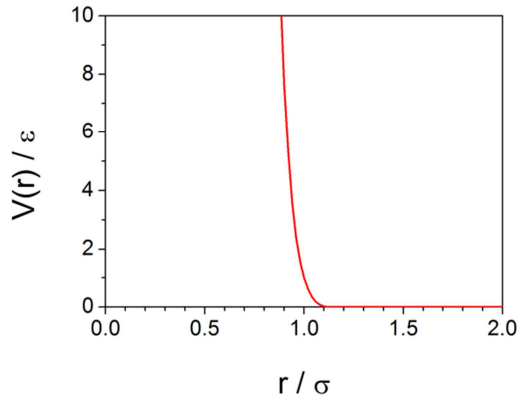

Figure 4.1 The WCA potential as a function of the interbead distance *r*. σ and ε are the characteristic parameters of the interaction.

The center of each bead lies on the arc of a circle, of contour length L=10, with the tangents at the arc's endpoints making an angle χ = 140° (Figure 4.2(A)). Three unit vectors are attached to the molecule (Figure 4.2(B)): **b** is along the C_2 molecular symmetry axis, and **a**,**c** are each perpendicular to a molecular symmetry plane, with $\mathbf{c} = \mathbf{a} \times \mathbf{b}$. With the choice made for N_b, L and χ, the distance between the terminal beads is about 9.8 and the angle between the unit vectors $\mathbf{u}_1$ and $\mathbf{u}_2$ connecting the central bead to the terminal ones (Figure 4.2(B)) is equal to 160°. In summary, the model bent-shaped molecules studied in this work are achiral, rigid object, bearing no electrical dipole, but only a steric dipole intrinsic to their C_{2v} symmetry.

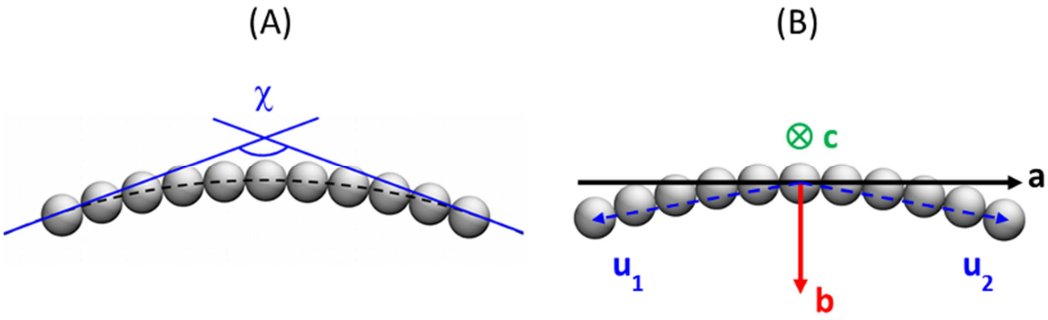

Figure 4.2 The molecular model studied in this work. (A) A particle is made of a chain of N_b=11 beads lying on the arc of a circle; the arc length is L=10 and the tangents at the arc's endpoints make an angle χ=140°. (B) **a**,**b**,**c** are unit vectors parallel to the principal molecular axes and $\mathbf{u}_1$,$\mathbf{u}_2$ are unit vectors connecting the central bead to the terminal ones.

4.3 Simulation details

Molecular Dynamics simulations were performed using the software LAMMPS [20]. A system of N=1000 molecules was studied in the *NPT* ensemble, at reduced temperature T=1 and reduced pressures P=0.65 and P=1.045. Temperature and pressure were controlled using a Nosé-Hoover thermostat and barostat [21-23], with time constants τ_T = 1 and τ_P = 1, respectively. The equations of motion were integrated using the rigid body algorithm of Ref. [24], with a time step Δt = 0.01. The neighbour list was updated every step. Tetragonal boxes with periodic boundary conditions (PBCs) were used, with sides $L_x = L_y \neq L_z$ having a fixed aspect ratio, $L_z / L_x = 4$. This relatively high aspect ratio was chosen with the purpose of minimizing the effect of PBCs on the pitch of the helical (N_{TB}) phase [25]. To evaluate the magnitude of finite-size effects in such an anisotropic box, another simulation at P=0.65 was conducted, using $L_z / L_x = 1.52$: the results thus obtained were in agreement with those found in the more anisotropic box. Simulations were started from a dilute lattice of molecules, with either polar or apolar arrangement of the molecular axes: after equilibration, analogous results were obtained in both cases. Simulations were run for tens of millions of steps, with configurations saved every 5×10^4 steps for subsequent analysis. Shorter runs, of about 5×10^4 steps and sampled every 10 steps, were also conducted for specific purposes. When presenting the results, these simulations will be referred to as "short" simulations.

4.4 Characterization of the phase organization

The structure of the phases formed by the system under study was investigated by determining various orientational order parameters and pair correlation functions [26, 27]. To compute these quantities, home-made Python codes were implemented, either as standalone programs or, for computationally intensive tasks such as the calculation of pair correlation functions, as scripts calling home-made C routines. For the latter purpose, the library "MD analysis" was used as a framework to interface Python and C codes [28]. This library was also used to extract the particles coordinates from the binary DCD trajectories [20].

4.4.1 Order parameters

Second rank orientational order parameters were obtained following the procedure described in Ref. [29]. For each configuration of the system, three ordering tensors $\mathbf{Q}_{\alpha\alpha}$ were computed, with elements:

$$Q_{\alpha\alpha}^{IJ} = \frac{1}{N}\sum_{i=1}^{N}\left(\frac{3}{2}\alpha_I^{(i)}\alpha_J^{(i)} - \frac{1}{2}\delta_{IJ}\right), \tag{4.2}$$

where $I, J = X', Y', Z'$ are cartesian axes of an arbitrary laboratory frame, $\alpha_I^{(i)}$ is the Ith component of the $\boldsymbol{\alpha}$ axis of the ith molecule ($\boldsymbol{\alpha} = \boldsymbol{a}, \boldsymbol{b}, \boldsymbol{c}$, see Figure 4.2(B)), and δ_{IJ} is the Krokecker delta. Diagonalization of the three $\mathbf{Q}_{\alpha\alpha}$ tensors yields three sets of eigenvalues $\left\{\lambda_{\alpha\alpha}^{+}, \lambda_{\alpha\alpha}^{0}, \lambda_{\alpha\alpha}^{-}\right\}$, with $\lambda_{\alpha\alpha}^{-} < \lambda_{\alpha\alpha}^{0} < \lambda_{\alpha\alpha}^{+}$. The principal phase director **Z** was identified with the eigenvector corresponding to the largest of the three $\lambda_{\alpha\alpha}^{+}$ eigenvalues, with the latter providing the major order parameter. For the systems here investigated, the largest $\lambda_{\alpha\alpha}^{+}$ was always obtained for $\boldsymbol{\alpha} = \boldsymbol{a}$, therefore we can write:

$$\mathbf{Q}_{aa} = \begin{pmatrix} \lambda_a^0 & 0 & 0 \\ 0 & \lambda_a^- & 0 \\ 0 & 0 & \lambda_a^+ \end{pmatrix} = \begin{pmatrix} Q_{aa}^{XX} & 0 & 0 \\ 0 & Q_{aa}^{YY} & 0 \\ 0 & 0 & Q_{aa}^{ZZ} \end{pmatrix}, \tag{4.3}$$

Q_{aa}^{ZZ} being the major order parameter. For a uniaxial phase $Q_{aa}^{XX} = Q_{aa}^{YY} = -Q_{aa}^{ZZ}/2$;

therefore the difference $Q_{aa}^{XX} - Q_{aa}^{YY}$ provides an indication of the phase biaxiality [30]. Many of the structural quantities defined in the following paragraphs are functions of the components along the director **Z** of molecular or intermolecular position vectors. In particular, if $\mathbf{r}_i$ is the position vector of the center of mass of the *i*th molecule, the molecular position along **Z** is given by $z_i = \mathbf{r}_i \cdot \mathbf{Z}$. Similarly, if $\mathbf{r}_{ij}$ is the vector joining the centers of mass of the *i*th and *j*th molecules, then its projection along **Z** is given by $z_{ij} = \mathbf{r}_{ij} \cdot \mathbf{Z}$. Structural quantities depending on these variables were computed over trajectory intervals in which the principal director **Z** was almost parallel to the long side of the simulation box.

To probe the existence of local polar ordering of the molecular **b** axis, first rank order parameters were calculated, as a function of the position *z* along the principal director **Z** [4,7]:

$$P_1^X(z) = \sum_{i=1}^{N} \left(\mathbf{b}_{i,\perp} \cdot \mathbf{X}\right) \delta\left(z_i - z\right) \Big/ \sum_{i=1}^{N} \delta\left(z_i - z\right), \tag{4.4}$$

$$P_1^Y(z) = \sum_{i=1}^{N} \left(\mathbf{b}_{i,\perp} \cdot \mathbf{Y}\right) \delta\left(z_i - z\right) \Big/ \sum_{i=1}^{N} \delta\left(z_i - z\right), \tag{4.5}$$

where **X** and **Y** are Cartesian axes in the plane perpendicular to **Z**, $\mathbf{b}_{i,\perp}$ is the unit vector obtained by projecting the **b** vector of the *i*th molecule on this plane, and δ is the Dirac delta function.

4.4.2 Pair distribution functions

The longitudinal pair distribution function was computed [31]:

$$g(r_{\parallel}) = \frac{1}{\rho L_x L_y} \frac{1}{N} \sum_{i=1}^{N} \sum_{\substack{j=1 \\ j \neq i}}^{N} \delta\left(\left|z_{ij}\right| - r_{\parallel}\right), \tag{4.6}$$

where $\rho = N/V$ is the molecular number density, with $V = L_x L_y L_z$ the volume of the system. In a nematic phase $g(r_{\parallel})$ is essentially constant; on the contrary, in a smectic phase $g(r_{\parallel})$ exhibits peaks with a periodicity equal to the distance between the smectic

layers.

4.4.3 Orientational pair correlation functions

Orientational pair correlations were characterized by considering a suitable set of orientationally-averaged Stone invariants* [32]. Both radial and longitudinal orientational correlation functions were obtained, respectively by computing these invariants as a function of *r*, the intermolecular distance, or of $r_{\parallel}$, the intermolecular separation along the director **Z**. Second rank orientational correlations were examined using the functions:

$$S_{aa}^{220}(r) = \sum_{i=1}^{N}\sum_{\substack{j=1 \\ j\neq i}}^{N}\left[\frac{3}{2}\left(\mathbf{a}_i \cdot \mathbf{a}_j\right)^2 - \frac{1}{2}\right]\delta\left(r_{ij} - r\right) \Bigg/ \sum_{i=1}^{N}\sum_{\substack{j=1 \\ j\neq i}}^{N}\delta\left(r_{ij} - r\right) , \tag{4.7}$$

$$S_{aa}^{220}(r_{\parallel}) = \sum_{i=1}^{N}\sum_{\substack{j=1 \\ j\neq i}}^{N}\left[\frac{3}{2}\left(\mathbf{a}_i \cdot \mathbf{a}_j\right)^2 - \frac{1}{2}\right]\delta\left(\left|z_{ij}\right| - r_{\parallel}\right) \Bigg/ \sum_{i=1}^{N}\sum_{\substack{j=1 \\ j\neq i}}^{N}\delta\left(\left|z_{ij}\right| - r_{\parallel}\right) . \tag{4.8}$$

where $\mathbf{a}_i$ and $\mathbf{a}_j$ are the unit vectors parallel to the long molecular axes of the *i*th and *j*th molecule (see Figure 4.2(B)). If the intermolecular distance is sufficiently large, the molecular orientations become uncorrelated and $S_{aa}^{220}(r)$ reaches a limiting value which is related to second rank order parameters according to [33,34]:

$$S_{aa}^{220}(r) \to \left(Q_{aa}^{ZZ}\right)^2 + 2\left(\frac{Q_{aa}^{XX} - Q_{aa}^{YY}}{\sqrt{6}}\right)^2 \qquad r \gg \xi_r , \tag{4.9}$$

where ξ_r is a correlation length. Polar pair correlations between the two-fold molecular symmetry axes **b** were probed by calculating the average invariants [4,7]:

$$S_{bb}^{110}(r) = \sum_{i=1}^{N}\sum_{\substack{j=1 \\ j\neq i}}^{N}\left(\mathbf{b}_i \cdot \mathbf{b}_j\right)\delta\left(r_{ij} - r\right) \Bigg/ \sum_{i=1}^{N}\sum_{\substack{j=1 \\ j\neq i}}^{N}\delta\left(r_{ij} - r\right) \tag{4.10}$$

* In this thesis, scaled invariants were calculated, by omitting the numerical pre-factors which appear in the definition of Stone invariants. For brevity, these scaled invariants will be denoted simply as invariants.

$$S_{bb}^{110}(r_{\parallel}) = \sum_{i=1}^{N}\sum_{\substack{j=1\\ j\neq i}}^{N}\left(\mathbf{b}_i\cdot\mathbf{b}_j\right)\delta\left(\left|z_{ij}\right|-r_{\parallel}\right) \Bigg/ \sum_{i=1}^{N}\sum_{\substack{j=1\\ j\neq i}}^{N}\delta\left(\left|z_{ij}\right|-r_{\parallel}\right) \quad . \tag{4.11}$$

Finally the following longitudinal correlation function was considered [4,35]:

$$S_{aa}^{221}(r_{\parallel}) = \sum_{i=1}^{N}\sum_{\substack{j=1\\ j\neq i}}^{N}\left[\left(\mathbf{a}_i\times\mathbf{a}_j\right)\cdot\frac{z_{ij}}{|z_{ij}|}\mathbf{Z}\right]\left(\mathbf{a}_i\cdot\mathbf{a}_j\right)\delta\left(\left|z_{ij}\right|-r_{\parallel}\right) \Bigg/ \sum_{i=1}^{N}\sum_{\substack{j=1\\ j\neq i}}^{N}\delta\left(\left|z_{ij}\right|-r_{\parallel}\right). \tag{4.12}$$

If the molecular organization is achiral, this function vanishes at all distances. On the contrary, for a helical phase of pitch p, this function exhibits a sinusoidal profile, with periodicity $\lambda=p/2$ for a cholesteric helix and $\lambda=p$ for a twist-bend helix. The helix handedness can be evaluated from the sign of the function at $r_{\parallel}=\lambda/4$:

$$\begin{cases} S_{aa}^{221}(r_{\parallel}=\lambda/4)>0 & \text{right-handed helix} \\ S_{aa}^{221}(r_{\parallel}=\lambda/4)<0 & \text{left-handed helix} \end{cases} \quad . \tag{4.13}$$

Trajectory averages of the quantities described above will be indicated with an overbar:

$$\overline{A} = \frac{1}{M}\sum_{m=1}^{M}A(t_m) \quad , \tag{4.14}$$

where $A(t_m)$ is the value of the property A at time t_m and M is the total number of time steps considered to compute the average.

4.5 Results and Discussion

The average number density $\overline{\rho}$ at the two values of pressure P investigated is reported in Table 4.1. The statistical error on density was estimated using the method of block averages [19].

P	$\overline{\rho}$
0.65	0.047589 ($\pm 2\times10^{-6}$)
1.045	0.05651 ($\pm 1\times10^{-5}$)

Table 4.1. Pressure P and average number density $\overline{\rho}$. The estimated statistical error on density is reported between parentheses.

At P=0.65 the system forms a nematic phase, as evidenced by the analysis of orientational order parameters, of the longitudinal pair distribution function and of orientational pair correlation functions. As shown in Figure 4.3(A)[†], the major order parameter Q_{aa}^{ZZ} is different from zero, indicating the formation of an orientationally ordered phase, with the long molecular axes **a** preferentially aligned with each other. The average value of the major order parameter is $\overline{Q_{aa}^{ZZ}} = 0.82$. Given the geometric relation between the molecular axes **a** and **b**, the latter preferentially orient perpendicular to **Z**, as confirmed by the negative value of the corresponding order parameter ($\overline{Q_{bb}^{ZZ}} = -0.41$). The longitudinal pair distribution function $g(r_{\|})$ is essentially constant (data not shown), leading to the identification of the phase as a nematic. Also reported in Figure 4.3(A) is the order parameter $Q_{aa}^{XX} - Q_{aa}^{YY}$, which is close to zero. The absence of long-range biaxial order is confirmed by the negligibly small value (less than 0.05) of the difference in the ordering of the **b** and **c** molecular axes in the plane perpendicular to the principal director **Z** [7,30,33].

The radial second rank orientational correlation function $\overline{S_{aa}^{220}(r)}$ (Figure 4.3(B)) reaches a plateau at a distance of about one molecular length, indicating the absence of long-range correlations. Its asymptotic value, $\overline{S_{aa}^{220}(r)} \sim 0.67$, is approximately equal to

[†] The results at P=0.65 presented in this and the other Figures are taken from the simulation with $L_z / L_x = 1.52$.

$\left(\overline{Q_{aa}^{ZZ}}\right)^2$, as expected for a uniaxial nematic phase (see Eq. (4.9)). The features appearing in the radial correlation function $\overline{S_{bb}^{110}(r)}$ (Figure 4.3(C)) indicate the presence of short-range polar correlations between the two-fold symmetry axes **b** of nearby molecules. At larger distances $\overline{S_{bb}^{110}(r)}$ vanishes. Because of the absence of long-range correlations, the longitudinal correlation functions $\overline{S_{aa}^{220}(r_{\|})}$ and $\overline{S_{bb}^{110}(r_{\|})}$ are essentially constant, and equal to the asymptotic value of the corresponding radial correlation function.

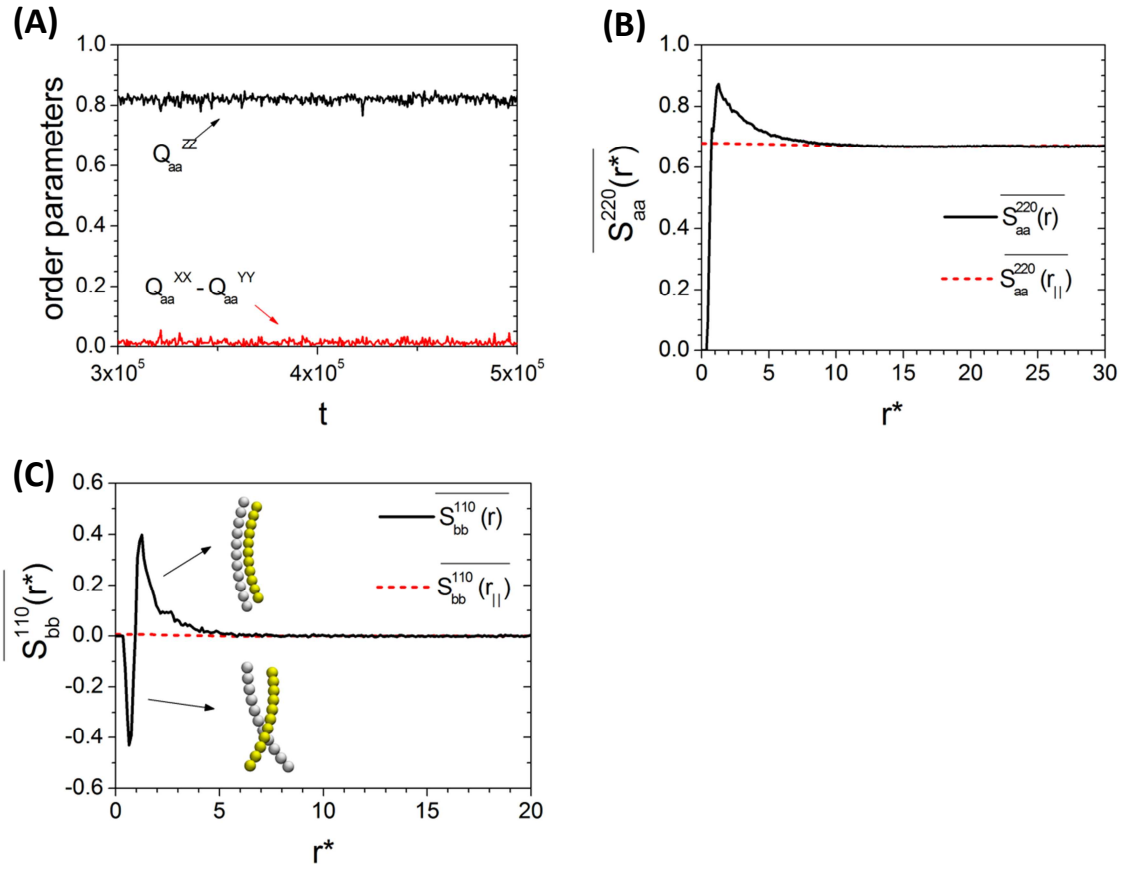

Figure 4.3 Orientational order parameters and pair correlation functions at P=0.65. (**A**) Second rank orientational order parameters Q_{aa}^{ZZ} (black line at the top) and $Q_{aa}^{XX} - Q_{aa}^{YY}$ (red line at the bottom), as a function of simulation time. (**B**) Radial ($\overline{S_{aa}^{220}(r)}$, solid black line) and longitudinal ($\overline{S_{aa}^{220}(r_{\|})}$, red dashed line) second rank orientational correlation functions for the molecular axis **a**. (**C**) Radial ($\overline{S_{bb}^{110}(r)}$, solid black line) and longitudinal ($\overline{S_{bb}^{110}(r_{\|})}$, dashed red line) polar orientational correlation functions for the molecular axis **b**. The cartoons show a pair of antiparallelly (/parallelly) oriented nearby molecules giving rise to the negative (/positive) peak in $\overline{S_{bb}^{110}(r)}$. In (**B**, **C**) the symbol r^* indicates either r or $r_{\|}$. Values of $r^* < 1$ are possible since the center of mass of the model bent-shaped molecule considered in this work lies outside the body.

At pressure P=1.045, the system still forms a nematic phase: no sign of layering could be detected from the analysis of the longitudinal distribution function $g(r_{\|})$. The second rank order parameters for the long molecular axis **a** are shown in Figure 4.4. The major order parameter Q_{aa}^{ZZ} exhibits large fluctuations, assuming values which range between 0.55 and 0.85. We will return on this point later. The biaxiality parameter $Q_{aa}^{XX} - Q_{aa}^{YY}$ is small, although also in this case relatively large fluctuations are observed.

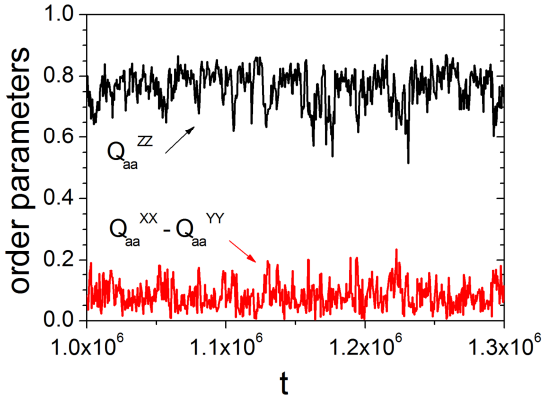

Figure 4.4 Second rank orientational order parameters at P=1.045, as a function of simulation time: major order parameter Q_{aa}^{ZZ} (black line at the top) and phase biaxiality $Q_{aa}^{XX} - Q_{aa}^{YY}$ (red line at the bottom).

The short-range structure of the system is qualitatively similar to that exhibited at P=0.65, as evidenced by the features appearing in the radial orientational correlation functions at short distances (data not shown). However a different long-range behavior is observed. In Figure 4.5(A)-(C) the longitudinal correlation functions $S_{aa}^{221}(r_{\|})$, $S_{bb}^{110}(r_{\|})$ and $S_{aa}^{220}(r_{\|})$ are reported. Multiple curves are shown in each plot, each corresponding to a single configuration taken from a representative part of the trajectory. The profiles obtained from each configuration are qualitatively similar: in particular, many of them are not flat, as it would be for a conventional nematic phase, but instead exhibit a periodic modulation as a function of $r_{\|}$, with a periodicity p ~ 65. Quantitatively the profiles differ, which is a signature that the system has a dynamic organization, continuously changing with time. The detailed analysis of each correlation function allowed us to characterize these modulated structures more precisely.

The oscillatory behavior of $S_{aa}^{221}(r_{\|})$ (Figure 4.5(A)) indicates the formation of a helical

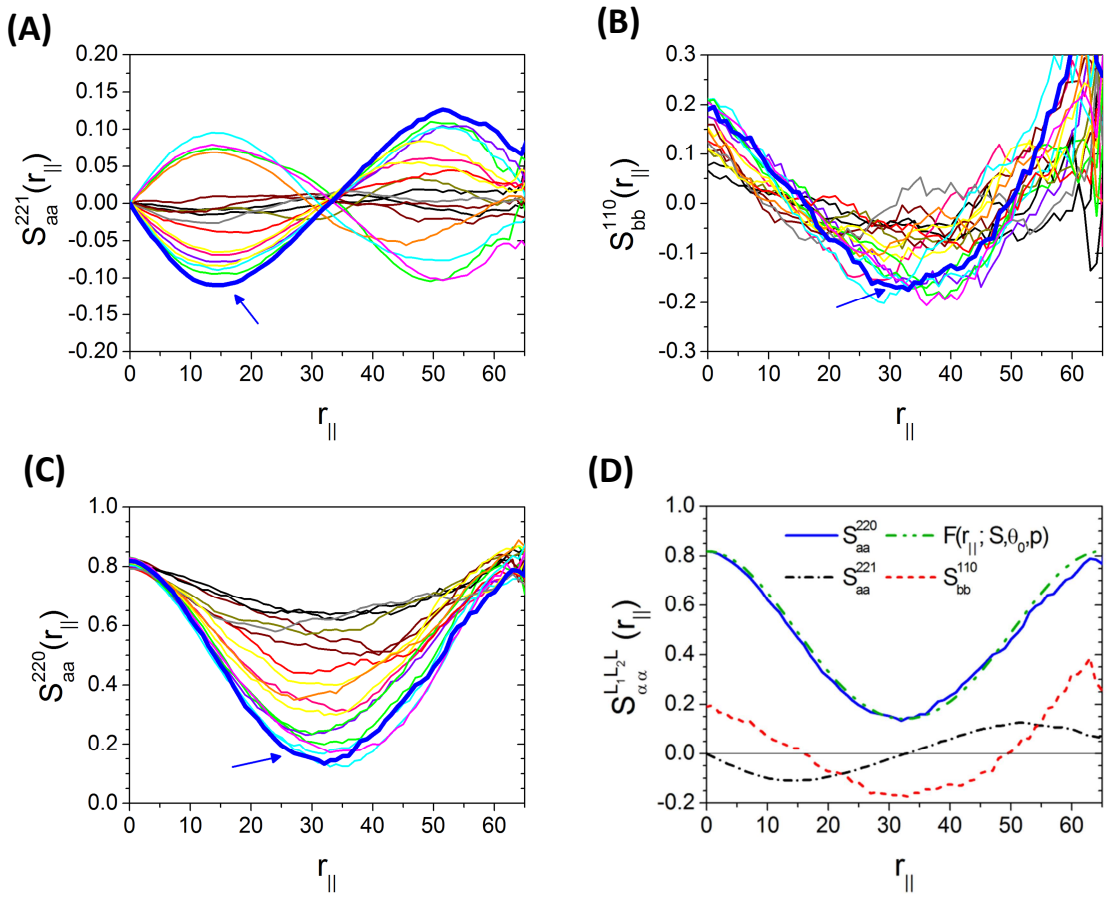

Figure 4.5 Longitudinal orientational correlation functions at P=1.045. (**A**, **B**, **C**) Data obtained from the analysis of a representative part of the trajectory. The various curves correspond to different configurations of the system. The same line color is used to plot data obtained from a given configuration. A thick blue line, also indicated by an arrow, is used to highlight one of the configurations giving the lowest minimum value of $S_{aa}^{220}(r_{||})$. The correlation functions for this configuration are shown together in (**D**): $S_{aa}^{220}(r_{||})$ (solid blue line), $S_{bb}^{110}(r_{||})$ (dashed red line) and $S_{aa}^{221}(r_{||})$ (dash-dotted black line). $F(r_{||};S,\theta_0,p)$ (dot-dot-dashed green line) is the function defined in Eq. (4.15), with parameters S=0.82, p=65 and θ_0=24°.

superstructure, with the helix axis parallel to **Z**. The inversion of the sinusoid along the trajectory indicates a change of handedness of the helix (see Eq.(4.13)). The interconversion between right- and left-handed helices gives rise to structures in which the helix is almost unwound and for which $S_{aa}^{221}(r_{||}) \sim 0$ is found.

The function $S_{bb}^{110}(r_{||})$ also oscillates (Figure 4.5(B)) and its maximum value, which corresponds to preferentially parallel arrangement of the **b** axes, is obtained for molecules lying on the same plane (perpendicular to **Z**), or separated by $r_{||} = p$. The

minimum of $S_{bb}^{110}(r_{\parallel})$ is located at $r_{\parallel} = p/2$: its negative value indicates that the **b** axes of molecules separated by this distance are preferentially anticorrelated. On the whole, the profile of $S_{bb}^{110}(r_{\parallel})$ shows that the helical organization is locally polar, with the two-fold molecular symmetry axes **b** spiralling around **Z**.

The value of $S_{aa}^{220}(r_{\parallel})$ in its minimum, also located at $r_{\parallel} \sim p/2$ (Figure 4.5(C)), provides information about the tilt angle θ_0 of the molecular long axis **a** with respect to the phase director **Z** [4]. For the system under study, each configuration is characterized by a different minimum value of $S_{aa}^{220}(r_{\parallel})$, and therefore by a different value of θ_0. This observation can explain, at least qualitatively, the large fluctuations detected in the order parameters (Figure 4.4): in each configuration, the molecular **a** axes are tilted with respect to the helix axis **Z**, and the tilt angle changes along trajectory, leading to different values of Q_{aa}^{ZZ}. To obtain an estimate of the highest value of tilt angle ($\theta_0^{\max}$) adopted by the system, one of the configurations providing the lowest minimum value of $S_{aa}^{220}(r_{\parallel})$ was selected (Figure 4.5(D)). An estimate of the corresponding tilt angle was obtained by analyzing the profile of $S_{aa}^{220}(r_{\parallel})$ with the following equation:

$$F(r_{\parallel};\, S, \theta_0, p) = S\left\{\frac{3}{2}\left[\sin^4\theta_0 \cos^2\left(\frac{2\pi r_{\parallel}}{p}\right) + 2\sin^2\theta_0 \cos^2\theta_0 \cos\left(\frac{2\pi r_{\parallel}}{p}\right) + \cos^4\theta_0\right]^2 - \frac{1}{2}\right\}, \tag{4.15}$$

where S is the value of S_{aa}^{220} at $r_{\parallel} = 0$ and p is the helical pitch. The term between curly brackets in Eq. (4.15) was derived by assuming that the long molecular axes **a** are perfectly ordered and undergo a heliconical precession around **Z**, as the one described by the local director **n** in a twist-bend nematic phase (see Eq. 3.3). The prefactor S accounts for the fact the orientational order is not perfect. Using S=0.82 and p=65, the value of tilt angle that provided the best agreement between Eq. (4.15) and the profile of $S_{aa}^{220}(r_{\parallel})$ in the selected configuration was found to be $\theta_0 = 24°$.

To further characterize the local polar arrangement of the molecular steric dipoles **b**, the polar order parameters $\overline{P_1^X}(z)$ and $\overline{P_1^Y}(z)$ defined by Eqs. (4.4)-(4.5) were computed, by

analysing a “short simulation” (see Section 4.3) during which the structure of the phase did not change appreciably. The results are reported in Figure 4.6, where the values obtained in the nematic phase at P=0.65 are also shown for comparison. The helical shape of the curve relative to P=1.045 clearly shows the presence of a local polar ordering axis which rotates around **Z** . The degree of order is represented by the helix radius. At P=0.65 the radius is close to zero, in agreement with the apolarity of the phase.

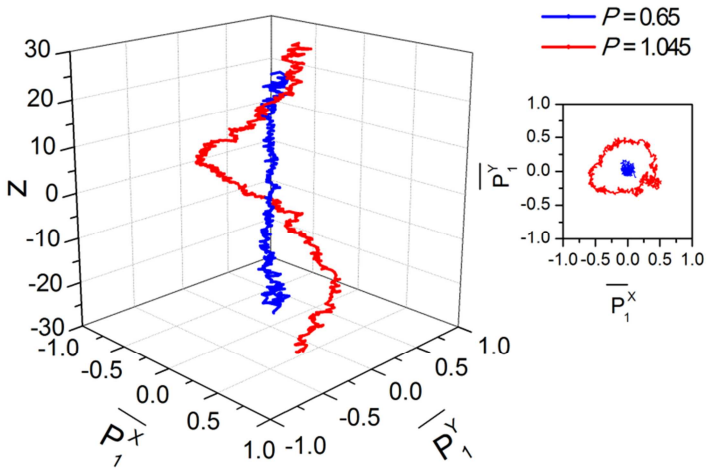

Figure 4.6 Polar order parameters $\overline{P_1^X}$ and $\overline{P_1^Y}$ as a function of the molecular position z along the principal director **Z**, at pressure P=0.65 and P= 1.045. The inset on the right shows the projection of the curves on the XY plane.

Snapshots of the molecular organization at P=0.65 and P=1.045 are reported in Figure 4.7, where each molecule is coloured according to its azimuthal angle in the plane perpendicular to Z.

The results obtained for the conical angle (θ_0^{max} ~ 24°) and for the pitch (p ~ 65 corresponding to 6-7 molecular lengths) can be compared with the available experimental data for the N_{TB} phase of different compounds [15,36-39], with the theoretical predictions obtained in this thesis and reported in Chapter 3 and 9 [40,41], and with the value provided by an atomistic MD simulation [15]: qualitative agreement is found for both quantities. Quantitatively, the pitch obtained from the simulations performed here is somewhat larger than the value reported in the references, which amounts to 3-5 molecular lengths. This difference may be a consequence of the geometric parameters used in the present investigation: for example, according to our

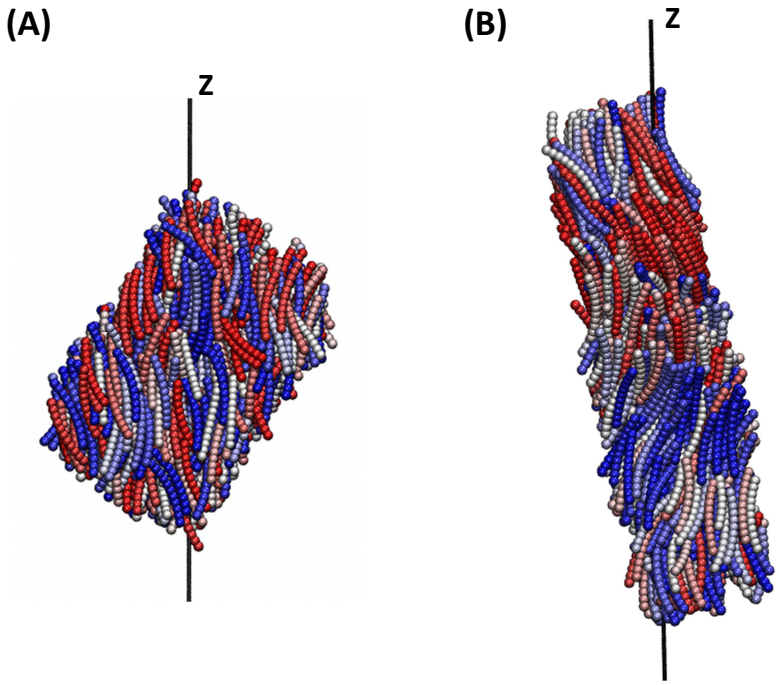

Figure 4.7 Snapshots of the molecular organization at (**A**) P=0.65 and (**B**) P=1.045. Each molecule i is colour-coded according to the value of $\mathbf{b}_{i,\perp} \cdot \mathbf{X}$, where $\mathbf{b}_{i,\perp}$ is the projection of the steric dipole $\mathbf{b}_i$ on the plane perpendicular to the principal director **Z,** and **X** is a Cartesian axis in this plane. The color scale ranges from red ($\mathbf{b}_{i,\perp} \cdot \mathbf{X} = -1$) to blue ($\mathbf{b}_{i,\perp} \cdot \mathbf{X} = +1$).

generalized Mayer-Saupe theory (Chapter 3) [40], a narrower bend angle should provide a slightly smaller pitch. Moreover, because of the use of periodic boundary conditions, the pitch may be influenced by the dimensions of the simulation box. Further simulations are needed to investigate this issue, but some preliminary work in this direction indicates that the value $p \sim 65$ here reported may be not too far from the equilibrium pitch.

4.6 Conclusions

Molecular Dynamics simulations of rigid, achiral, apolar bent-shaped particles were performed, using a generic coarse-grained molecular model consisting of a chain of purely repulsive spherical interactions sites arranged on the arc of a circle. The behaviour of particles with an angle $\chi = 140°$ between the arc's endpoint was examined. Simulations were conducted at two different pressures P to investigate whether we could observe a phase transition to the twist-bend nematic phase (N_{TB}). Although this

study is still preliminary, some interesting indications have been found. At P=0.65 the system organizes into a conventional nematic phase, but significant changes are observed by increasing the pressure to P=1.045. The results obtained from the analysis of various structural parameters are in line with the presence of a twist-bend nematic organization. Both right- and left-handed conical helices form during the simulation time: as a result of the interconversion between helices of opposite handedness, different conical angles θ_0 are observed along the trajectory, with a maximum value of $\theta_0^{\max} = 24°$. The observation of a twist-bend organization in a system of rigid, achiral, apolar particles with purely steric interactions is not a foregone result and points out the crucial role of the bent molecular shape. This is in agreement with the conclusions reached in the previous Chapter using a generalized Maier-Saupe theory [40], and contrasts with the interpretations proposed in Ref. [42,43] and Ref. [44,45], where the N_{TB} organization was ascribed to flexoelectricity or conformational chirality, respectively. Notice that in the generalized Maier-Saupe theory, the N_{TB}-N phase transition is of enthalpic origin: in the system of "hard" particles considered here the transition must be driven by the entropic gain associated with exclude-volume effects. Experimentally the twist-bend phase has been observed in thermotropic liquid crystals (see Chapter 2): it would be of interest to check whether bent-shaped colloids can also exhibit this organization.

The results presented here need to be confirmed by further simulations, on larger systems and/or employing computational boxes of different size or different boundary conditions. Further possible extensions of the current work include simulations of systems with a smaller bend angle. Investigation of the effect of molecular flexibility, here neglected, is also of major interest. Finally, comparison with the phase behaviour of multi-site V-shaped models, for which, up to now, a nematic twist-bend phase has not been detected [10-13], is an aspect worth further exploration.

4.7 References

1 P. J. Camp, M. P. Allen and A. J. Masters, *J. Chem. Phys.*, 1999, **11**, 9871-9881.

2 Y. Lansac, P. K. Maiti, N. A. Clark, and M. A. Glaser, *Phys. Rev. E*, 2003, **67**,011703.

3 S. D. Peroukidis, A. G. Vanakaras and D. J. Photinos, *Phys. Rev. E*, 2011, **84**, 010702

(R).

4 R. Memmer, *Liq. Cryst.* 2002, **29**, 483-496.

5 S. J. Johnston, R. J. Low and M. P. Neal, *Phys. Rev. E*, 2002, **65**, 051706.

6 S. J. Johnston, R. J. Low and M. P. Neal, *Phys. Rev. E*, 2002, **66**, 061702.

7 S. Orlandi, R. Berardi, J. Steltzer and C. Zannoni, *J. Chem. Phys.*, 2006, **124**, 124907.

8 W. Józefowicz and L. Longa, *Mol. Cryst. Liq. Cryst.*, 2011, **545**, 204-213.

9 O. Francescangeli, V. Stanic, S. I. Torgova, A. Strigazzi, N. Scaramuzza, C. Ferrero, I. P. Dolbnya, T. M. Weiss, R. Berardi, L. Muccioli, S. Orlandi and C. Zannoni, *Adv. Funct. Mater.*, 2009, **19**, 2592-2600.

10 J. Xu, R. L. B. Selinger, J. V. Selinger and R. Shashidhar, *J. Chem. Phys.*, 2001, **115**, 4333-4338.

11 A. Dewar and P. J. Camp, *Phys. Rev. E*, 2004, **70**, 011704.

12 A. Dewar and P. J. Camp, *J. Chem. Phys.*, 2005, **123**, 174907.

13 R. J. Sargant, PhD Thesis, University of Manchester, 2012.

14 J. Pelaez and M. Wilson, *Phys. Rev. Lett.*, 2006, **97**, 267801.

15 D. Chen, J. H. Porada, J. B. Hooper, A. Klittnick, Y. Shen, M. R. Tuchband, E. Korblova, D. Bedrov, D. M. Walba, M. A. Glaser, J. E. Maclennan and N. A. Clark, *Proc. Natl. Acad. Sci. U.S.A.*, 2013, **110**, 15931–15936.

16 M. A. Bates and G. R. Luckhurst, *Phys. Rev. E*, 2005, **72**, 051702.

17 S. M. Shamid, S. Dhakal and J. V. Selinger, *Phys. Rev. E*, 2013, **87**, 052503.

18 I. Dozov, *Europhys. Lett.*, 2001, **56**, 247–253.

19 M. P. Allen and D. J. Tildesley, *Computer Simulation of Liquids*, Clarendon Press, Oxford, 1987.

20 S. Plimpton, *J. Comput. Phys.*, 1995, **117**, 1-19.

21 M. Tuckerman, B. Berne and G. Martyna, *J. Chem. Phys.*, 1992, **97**, 2635-2643.

22 G. Martyna, D. Tobias and M. Klein, *J. Chem. Phys.*, 1994, **101**, 4177-4189.

23 M. Tuckerman, *Statistical Mechanics: Theory and Molecular Simulation*, Oxford University Press, New York, 2010.

24 H. Kamberaj, R. J. Low and M. P. Neal, *J. Chem. Phys.*, 2005, **122**, 224114.

25 D. Frenkel, *Eur. Phys. J. Plus*, 2013, **128**,10.

26 C. Zannoni, in *The Molecular Physics of Liquid Crystals*, ed. G. R. Luckhurst and G. W. Gray, Academic Press, 1979, ch. 3.

27 C. Zannoni, in *Advances in the Computer Simulatons of Liquid Crystals*, ed. P. Pasini and C. Zannoni, Kluwer, Dordrecht, 2000, ch. 2.

28 N. Michaud-Agrawal, E. J. Denning, T. B. Woolf and O. Beckstein, *J. Comput. Chem.*, 2011, **32**, 2319–2327.

29 M. P. Allen, *Liq. Cryst.*, 1990, **8**, 499-511.

30 F. Biscarini, C. Chiccoli, P. Pasini, F. Semeria and C. Zannoni, *Phys. Rev. Lett.*, 1995, **75**, 1803-1806.

31 J. Billeter and R. Pelcovits, *Comput. Phys.*, 1998, **12**, 440-448.

32 A. J. Stone, *Mol. Phys.*, 1978, **36**, 241-256.

33 R. Berardi and C. Zannoni, *J. Chem Phys.*, 2000, **113**, 5971-5979.

34 R. Berardi, S. Orlandi and C. Zannoni, *Phys. Chem. Chem. Phys.*, 2000, **2**, 2933-2942.

35 R. Berardi, M. Cecchini, and C. Zannoni, *J. Chem. Phys.*, 2003, **119**, 9933-9946.

36 C. Meyer, G. R. Luckhurst and I. Dozov, *Phys. Rev. Lett.*, 2013, **111**, 067801.

37 V. Borshch, Y.-K. Kim, J. Xiang, M. Gao, A. Jakli, V. P. Panov, J. K. Vij, C. T. Imrie, M. G. Tamba, G. H. Mehl and O. D. Lavrentovich, *Nat. Commun.*, 2013, **4**, 2635.

38 D. Chen, M. Nakata, R. Shao, M. R. Tuchband, M. Shuai, U. Baumeister, W. Weissflog, D. M. Walba, M. A. Glaser, J. E. Maclennan and N. A. Clark, *Phys. Rev. E*, 2014, **89**, 022506.

39 P. K. Challa, V. Borshch, O. Parri, C. T. Imrie, S. N. Sprunt, J. T. Gleeson, O. D. Lavrentovich and A. Jákli, *Phys. Rev. E* , 2014, **89**, 060501(R).

40 C. Greco, G. R. Luckhurst and A. Ferrarini, *Soft Matter*, 2014, **10**, 9318-9323.

41 C. Greco, G. R. Luckhurst and A. Ferrarini, *Phys. Chem. Chem. Phys.*, 2013, **15**, 14961–14965.

42 R. B. Meyer, in *Molecular Fluids (Le Houches Summer School on Theoretical Physics* 1973), ed. R. Balian and G. Weill, Gordon and Breach, New York, 1976, pp. 271–343.

43 N. Vaupotič, M. Čepič, M. A. Osipov and E. Gorecka, *Phys. Rev. E*, 2014, **89**, 030501.

44 A. Hoffmann, A. G. Vanakaras, A. Kohlmeier, G.H. Mehl and D. J. Photinos, arXiv:1401.5445, 2014.

45 T. Ivšić, M. Vinković, U. Baumeister, A. Mikleuševića and A. Lesac, *Soft Matter*, 2014, **10**, 9334-9342.

Part III

Chapter 5

Modelling the properties of nematic liquid crystals of bent-shaped molecules with atomistic detail

5.1 Introduction

Liquid crystals (LCs) are complex soft materials, whose structure and behaviour are characterized by different length and time scales [1]. The relevant properties and interesting phenomena, though related to the microscopic structure, involve scales much larger than the molecular one. Important physical properties, such as the elastic moduli, are material parameters defined at the macroscopic scale.

This poses a fundamental challenge to computational methods. Different particle-based methods exist, suitable to investigate the behaviour of soft matter at a certain level of resolution [1-4]. Quantum mechanical (QM) methods can provide accurate information about single-molecule properties but, at the present stage, are alone not sufficient to study soft materials, given the importance that intermolecular interactions and thermal fluctuations have for the behaviour of these systems. Atomistic Molecular Dynamics (MD) or Monte Carlo (MC) simulations allow studying samples of thousands of molecules for tens or hundreds of nanoseconds, and are thus suited to investigate structural features and behaviour at the nanoscale. Finally, generic particle models have proved useful for a basic understanding of processes and properties at the mesoscopic scale. Addressing problems at this scale while retaining chemical specificity, is, on the contrary, a difficult task. The ability to predict the properties of LCs starting from the molecular structure is of paramount importance for material design, given the strong sensitivity of these properties to chemical details. In recent years major advancements have been made in atomistic simulations of rod-like LCs: phase transition temperatures,

molecular order parameters, conformational distributions and other structural properties can be predicted with reasonable accuracy, provided suitable force-fields are used [5-7]. Atomistic simulation studies of the phase behaviour of bent-shaped molecules are much more challenging [8-11], and several aspects of the molecular organization of these systems remain poorly understood.

The situation is even more critical for material properties such as elasticity and flexoelectricity. Different techniques have been proposed to determine these parameters from MD simulations [1,12-14]. Elastic constants can be obtained in a direct way from the long-wavelength fluctuations of the ordering tensor: this approach is robust, but requires very large samples to measure fluctuations with small wavevectors. Alternatively, an indirect approach can be used, based on a density functional formalism [15,16], which relates the elastic constants to the direct correlation functions (DCF). The latter can be in principle obtained from computer simulations [17]: in practice various approximations are usually introduced, which can impair the results. Recently a method based on free-energy calculations has also been proposed [14], but up to know it has been used only in the original paper. Calculations of flexoelectric coefficients from atomistic simulations are pratically non-existent. In principle, flexoelectric coefficients can be obtained from the DCF [16,18]: the problems of this approach are analogous to those mentioned above for the elastic constants. In Ref. [13] a linear response theory was used, whereby the flexoelectric coefficients are related to correlation functions of the polarization and orientational stress tensor: the results were affected by relatively large errors and the authors pointed out the need to find alternative routes.

Recently, an integrated methodology (IM) has been proposed for predicting the phase and materials properties of nematic LCs, including elasticity and flexoelectricity, starting from the molecular structure [19-23]. For this purpose the method combines an atomistic description of the molecular structure with a molecular field model for the orientational order in the nematic (N) phase, by means of the so-called Surface Interaction (SI) model [24]. The method has been successfully applied to the prediction of the elastic constants of conventional rod-like LCs [25], obtaining results in good quantitative agreement with experimental data, at a modest computational cost. In Ref. [23] the method was used to investigate the elastic and flexoelectric behaviour of a series of ether-linked LC dimers with odd and even-membered spacers, providing

considerable understanding about the dependence of these properties on the molecular structure.

In this thesis, the IM methodology has been used to investigate the phase and materials properties of nematic LCs of bent-core compounds and liquid crystal dimers. We considered systems with different chemical structures, with the aim to shed light on the relationship between the molecular structure of bent-shaped systems and their macroscopic behaviour. In the remaining part of this Chapter a brief review of the SI model, and of its use in the derivation of expressions for the elastic and flexoelectric parameters, will be given, and the IM computational procedure will be outlined. In Chapter 6 the uniaxial N phase of the bent core compound A131 will be characterized, looking at properties at different length scales. Chapter 7 is devoted to the elastic and flexoelectric properties of bent-core compounds and Chapter 8 to the elastic behaviour of liquid crystal dimers. Finally, in Chapter 9, we will show how the SI model can be extended to describe the long-range orientational order in the recently discovered twist-bend nematic phase (N_{TB}).

5.2 The Surface Interaction model (SI)

The Surface Interaction model (SI) is a molecular field model for the orientational distribution in nematic LCs, in which the anisotropy of the short-range steric and dispersive interactions responsible for orientational order is parameterized according to the anisotropy of the molecular surface. As such it can be thought of as a generalization of the Maier-Saupe theory* to molecules of any shape and structure. Assuming that each surface element *dS* tends to align parallel to the director **n**, the orienting molecular field potential, U^{or}, experienced by a rigid molecule is expressed as an integral over the molecular surface *S* [24]:

$$U^{or}(\Omega) = \varepsilon k_{\mathrm{B}} T \int_{S} P_2\left(\mathbf{n}\cdot\mathbf{s}\right) dS \ . \tag{5.1}$$

Here $\Omega = \{\alpha, \beta, \gamma\}$ is the set of Euler angles defining the molecular orientation in a

* The Maier-Saupe theory is outlined in Chapter 1.

laboratory frame $\{X,Y,Z\}$, k_B is the Boltzmann constant, T is the temperature, **s** is the unit vector perpendicular to the surface element dS and P_2 is the second Legendre polynomial. Finally ε is a parameter, with dimension of inverse square length, which quantifies the orienting strength of the nematic environment. As such it is related to the reduced temperature $T_r = T/T_{NI}$, where T_{NI} is the nematic (N) to isotropic (I) transition temperature, higher values of ε corresponding to lower T_r. The single particle orientational distribution function, $p(\Omega)$, is related to the molecular field potential by[†]:

$$p(\Omega) = \frac{1}{Q}\exp\left[-U^{or}(\Omega)/k_B T\right] , \tag{5.2}$$

where is Q the orientational partition function:

$$Q = \int \exp\left[-U^{or}(\Omega)/k_B T\right] d\Omega \quad . \tag{5.3}$$

Orientational averages are defined by:

$$\langle ... \rangle = \int ... p(\Omega)\, d\Omega ; \tag{5.4}$$

So, according to Eq. 1.9, the second rank order parameter for an arbitrary axis (i) in the molecule is given by:

$$S_{ii} = \frac{3}{2}\left\langle \cos^2 \beta_i \right\rangle - \frac{1}{2}, \tag{5.5}$$

where β_i is the angle between the i axis and the director **n**. Conformational flexibility can be easily included into the model. Let's denote by $\boldsymbol{\chi}$ the set of torsional degrees of freedom: then the orientational distribution function is replaced by the orientational-conformational distribution function, $p(\Omega,\boldsymbol{\chi})$, which can be approximated as:

$$p(\Omega,\boldsymbol{\chi}) = \frac{1}{Z}\exp\left\{-\left[U_{\chi}^{or}(\Omega) + V(\boldsymbol{\chi})\right]/k_B T\right\} \quad , \tag{5.6}$$

where $V(\boldsymbol{\chi})$ is the torsional potential in the isotropic phase, $U_{\chi}^{or}(\Omega)$ is the orienting

[†] General definitions of distribution functions and second-rank order parameters can be found in Chapter 1.

potential experienced by a molecule in the conformational state defined by $\boldsymbol{\chi}$ and Z is the conformational-orientational partition function:

$$Z = \int d\Omega d\boldsymbol{\chi} \exp\left\{-\left[U_{\chi}^{or}(\Omega) + V(\boldsymbol{\chi})\right]/k_{\mathrm{B}}T\right\}. \tag{5.7}$$

Equilibrium properties are then given by the following conformational-orientational averages:

$$\begin{aligned} \langle ... \rangle &= \int ... p(\Omega, \boldsymbol{\chi})\, d\Omega d\boldsymbol{\chi} \\ &= \int \langle ... \rangle_{\chi} \, w(\boldsymbol{\chi})\, d\boldsymbol{\chi} \end{aligned} \quad . \tag{5.8}$$

Here $\langle ... \rangle_{\chi}$ denotes an orientational average for the conformation specified by the torsional angles $\boldsymbol{\chi}$:

$$\begin{aligned} \langle ... \rangle_{\chi} &= \int ... p_{\chi}(\Omega)\, d\Omega \\ &= \frac{1}{Q_{\chi}} \int ... \exp\left[-U_{\chi}^{or}(\Omega)/k_B T\right] d\Omega \end{aligned} \quad , \tag{5.9}$$

and $w(\boldsymbol{\chi})$ is the conformational distribution function in the nematic phase:

$$w(\boldsymbol{\chi}) = \frac{\exp\left[-V(\boldsymbol{\chi})/k_{\mathrm{B}}T\right] Q_{\chi}}{Z} \quad . \tag{5.10}$$

This function depends on the degree of orientational order, and is thus different from that in the isotropic phase: in general the orienting potential will stabilize elongated conformations, which are better accommodated in the nematic environment than bent ones. If the Rotational Isomeric State approximation (RIS) [26] is used, the full conformational distribution is replaced by a finite set of conformers, each corresponding to a relative minimum of the torsional potential. Then the integrals over $\boldsymbol{\chi}$ can be replaced by a sum over conformers, and the averages defined by Eq. (5.8) can be rewritten as:

$$\langle ... \rangle = \sum_{m} \langle ... \rangle_{m} \, w_{m} \quad , \tag{5.11}$$

where the index *m* runs over conformers.

5.2.1 Elastic constants by the SI method

Within the framework of the SI model, director deformations arising from elastic distorsions or flexoelectric couplings are accounted for through the position dependence of the director field, **n**=**n**(**R**), in Eq. (5.1). Elastic constants can then be obtained as second derivatives of the Helmoltz free energy density, $a = A/V$, with V the volume of the system, taken with respect to the three director deformation modes[‡]. The difference in free energy density between the nematic and isotropic phase, Δa, is given by [22]:

$$\begin{aligned} \Delta a &= \Delta u - T\Delta s \\ &= \frac{1}{v}\left\{ \frac{1}{2}\left\langle U^{or} \right\rangle + \left\langle \Delta V(\boldsymbol{\chi}) \right\rangle + k_{\mathrm{B}}T \left\langle \ln p \right\rangle \right\} \quad , \end{aligned} \tag{5.12}$$

where $\Delta u = \Delta U/V$ and $\Delta s = \Delta S/V$ are the internal energy and entropy contributions, v is the volume per molecule, $\Delta V(\boldsymbol{\chi})$ is the difference between the torsional potential in the nematic and isotropic phase, reflecting the difference in the conformational distribution, and the angular brackets denotes orientational-conformational averages, Eq. (5.8) or (5.11). The free energy density, Eq.(5.12), can be expanded in Taylor series with respect to gradients of the director: for deformations characterized by a length scale much longer than the molecular dimensions, the expansion can be truncated at quadratic terms and the elastic constants are identified with the coefficients of these terms. The following molecular expressions are thus obtained for the splay (K_{11}), twist (K_{22}) and bend (K_{33}) elastic constants [22]:

$$K_{ii} = \frac{k_{\mathrm{B}}T}{v}\left\{ \; 3\varepsilon\left[c_{IIXX} - c_{IIZZ} - 2c_{XZXZ}\left(\delta_{i1} - \delta_{i3}\right)\right] - 9\varepsilon^2 c_{IXZ,IXZ} + 9\varepsilon^2 c_{YXZ}^2 \delta_{i2} \; \right\} \tag{5.13}$$

$I = X$ for $i = 1$, $I = Y$ for $i = 2$, $I = Z$ for $i = 3$.

The terms c_{JKL}, c_{JKLM} and $c_{JKL,JKL}$ are elements of Cartesian tensors defined as integrals over the molecular surface, and averaged according to $p_0(\Omega,\boldsymbol{\chi})$, the distribution function in the undeformed nematic phase. The Z axis is parallel to the director **n** in this phase.

[‡] The fundamental deformation modes of the N phase have been defined in Chapter 2.

5.2.2 Flexoelectric coefficients by the SI method

Expressions for the flexoelectric coefficients can be obtained starting from the microscopic definition of the electric polarization [27]:

$$\mathbf{P} = \frac{1}{v}\left(\langle \boldsymbol{\mu} \rangle - \nabla \cdot \langle \boldsymbol{\theta} \rangle + ...\right) \tag{5.14}$$

where $\boldsymbol{\mu}$ and $\boldsymbol{\theta}$ are respectively the molecular electric dipole and quadrupole moments. If the molecular charge distribution is described by a set of point charges q_α located at the nuclei positions $\mathbf{R}_\alpha$, the dipole and quadrupole moments take the form [27]:

$$\boldsymbol{\mu} = \sum_\alpha q_\alpha \mathbf{R}_\alpha \ , \tag{5.15}$$

$$\boldsymbol{\theta} = 1/2 \sum_\alpha q_\alpha \left(\mathbf{R}_\alpha \otimes \mathbf{R}_\alpha\right) \ , \tag{5.16}$$

where the symbol $\otimes$ indicates a direct product. Eqs. (5.15) and (5.16) can be substituted into Eq. (5.14), and the resulting expression can be compared with the macroscopic form of the flexoelectric polarization, Eq. 2.2. In the limit of long wavelength deformations of the director, the following microscopic expressions for the splay (e_1) and bend (e_3) flexoelectric coefficients are finally obtained [19,20]:

$$e_i = -\frac{3\varepsilon}{v}\left\langle \int_S dS \mu_I r_J s_X s_Z \right\rangle_0 + \frac{3\varepsilon}{v}\left\langle \int_S dS \ \theta_{ZX} s_X s_Z \right\rangle_0$$
$$I = Z, J = X \quad \text{for} \quad i = 1 \quad ; \quad I = X, J = Z \quad \text{for} \quad i = 3 \ , \tag{5.17}$$

where again the averages are calculated over the distribution function in the undeformed phase, $p_0(\Omega,\boldsymbol{\chi})$, and Z is parallel to the director. The splay and bend flexoelectric coefficients have both a dipolar (d) and a quadrupolar (q) contribution[§], corresponding respectively to the first and second term on the right side of Eq. (5.17): $e_3(d)$ depends only on μ_X, the component of the electric dipole moment perpendicular to the director,

[§] The flexoelectric coefficients e_1 and e_3 defined by Eq. (5.17) are independent of the choice of the origin of the molecular frame. However each of the two integrals contributing to e_1 and e_3, taken individually, depends on this choice: in order to uniquely identify a dipolar and quadrupolar contribution to the flexoelectric coefficients, these integrals are averaged over all possible origins within the molecular volume, as done for the elastic constants in Ref. [22].

whereas $e_1(d)$ depends only on μ_Z, the component parallel to the director. The quadrupole contribution is identical for e_1 and e_3. Experimentally, measurements of the individual flexoelectric coefficients are rare, and more commonly their difference and sum are determined. On the basis of Eq. (5.17) these are given by:

$$e_1 - e_3 = -\frac{3\varepsilon}{v}\left[\left\langle \int_S dS \mu_Z r_X s_X s_Z \right\rangle_0 - \left\langle \int_S dS \mu_X r_Z s_X s_Z \right\rangle_0\right] \tag{5.18}$$

$$e_1 + e_3 = -\frac{3\varepsilon}{v}\left[\left\langle \int_S dS \mu_Z r_X s_X s_Z \right\rangle_0 + \left\langle \int_S dS \mu_X r_Z s_X s_Z \right\rangle_0 - 2\left\langle \int_S dS \theta_{ZX} s_X s_Z \right\rangle_0\right] \quad . \tag{5.19}$$

Therefore $(e_1 - e_3)$ depends only on the molecular dipole moment and vanishes for non-polar molecules, while both dipole and quadrupole moments contribute to $(e_1 + e_3)$.

5.3 The IM Computational Methodology

Eqs. (5.13) and (5.17) allow to predict the elastic constants and the flexoelectric coefficients (magnitude and sign) starting from knowledge of the molecular geometry, torsional potentials and atomic charges. At the computational level this requires using and combining different methods: the overall procedure is outlined in Figure 5.1. Reliable predictions of phase properties are possible only if accurate values of the molecular parameters are employed: the latter were obtained by quantum mechanical density functional theory (DFT) calculations in vacuum [28], using different levels of theory, according to the required degree of accuracy. For the systems investigated in this thesis, geometry optimizations on single conformations were generally performed at the B3LYP/6-31G** level [29,30]. Atomic charges were obtained using the RESP method, with the electrostatic potential computed at the B3LYP/6-311+G** level [31,32]. One of the main advantages of the RESP approach is its ability to provide charges which are only weakly conformation dependent [31]. Electric dipole and quadrupole moments and flexoelectric coefficients were computed by reducing the RESP charges by a factor of 0.7 [23].

Torsional potentials were obtain using a fragment-based approach: the molecular structure was broken into smaller representative model compounds, as customarily done in force-field development [33]. Relaxed torsional scans were performed, using either

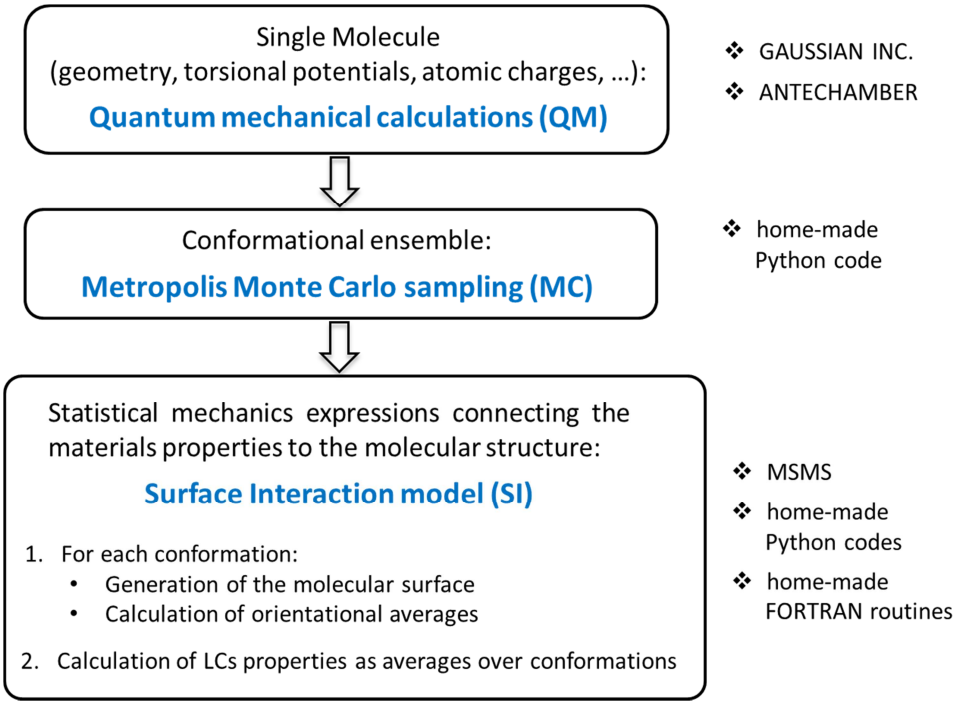

Figure 5.1. Scheme of the IM computational methodology (left) and of the principal computer codes used at each step (right).

the B3LYP or the M06-2X [34] functionals, and a Gaussian double-zeta basis set, usually 6-31+G**, as a compromise between cost-effectiveness and accuracy [34,35]. M06-2X is a relatively new functional developed to account for non-local electronic correlations at the basis of dispersion interactions, which common functional, such as B3LYP, are unable to describe correctly [36]. Because of its nature, the M06-2X can only capture electron correlations at the medium-range, but this can be sufficient to account for dispersion effects in small molecular systems [36,37]. Generally, in this thesis, the B3LYP functional was used to compute simple torsional profiles (for example those characterized by two symmetry-related minima separated by a large barrier) whereas the M06-2X functional was used to model more complex torsional profiles, such as those relative to fragments containing alkyl chains and aromatic rings, for which dispersion effects might be important. The torsional potential data thus obtained were fitted according to the following functional form [33]:

$$V(\chi) = V_0 + \sum_n \frac{V_n}{2}\left[1+\cos\left(n\chi+\gamma_n\right)\right] \quad , \tag{5.20}$$

where values of n up to 6 were considered. If the torsional potential is symmetric with

respect to χ=0°, the phase angles γ_n can be simply set equal to 0° (for odd n) or 180° (for even n), and the only fitting parameters are represented by the coefficients V_0-V_n. Otherwise the phase angles were also included among the fitting parameters.

The torsional profiles obtained from the fitting procedure were used to generate molecular conformations by Monte Carlo (MC) sampling. At each MC move a certain (random) number of dihedral angles is changed by a random rotation: the resulting conformation is accepted or rejected on the basis of its torsional energy, according to the Metropolis criterion [38]. In this way the conformational space is populated according to the canonical distribution $w^{iso}(\chi) \propto \exp\left[-V(\chi)/k_B T\right]$ [39, 40]. In some cases, instead of sampling the full torsional profile, the RIS approximation [26] was adopted and only the conformers corresponding to the relative minima of the torsional potential were considered: this will be specified when presenting the results in Chapters 6-9. In the MC sampling procedure, conformations containing steric clashes were identified and eliminated: this was achieved by checking for pair of atoms closer than a cutoff distance $d = x\left(r_i + r_j\right)$, where r_i is the van der Waals radius of atom i and x=0.82 [21] : radii equal to 0.185 nm (C), 0.15 nm (N and O), and 0.1 nm (H) were assumed [41].

For each molecular conformation, calculation of the mean field potential, Eq. (5.1), requires the definition of the molecular surface. For this purpose the solvent excluded surface was used, generated by rolling a probe sphere over the set of spheres representing a molecule. The triangulated surface was calculated using the free library MSMS [42], with a probe sphere radius of 0.3 nm and a density of vertices of 5 $Å^{-2}$. The same van der Waals radii used for the cutoff distance were assumed.

5.4 References

1 M. R. Wilson, *Int. Rev. Phys. Chem.*, 2005, **24**, 421-453.

2 C. Peter and K. Kremer, in *Multiscale Simulation Methods in Molecular Sciences*, ed. J. Grotendorst, N. Attig, S. Blügel and D.Marx, NIC Series, Jülich, 2009, vol. 42, pp. 337-358.

3 C. Peter and K. Kremer, *Faraday Discuss.*, 2010, **144**, 9-24.

4 S. O. Nielsen, R. E. Bulo, P. B. Moore and B. Ensing, *Phys. Chem. Chem. Phys.*,

2010, **12**, 12401-12414.

5 A. Pizzirusso, M. E. Di Pietro, G. De Luca, G. Celebre, M. Longeri, L. Muccioli and C. Zannoni, *ChemPhysChem*, 2014, **15**, 1356-1367.

6 G. Tiberio, L. Muccioli, R. Berardi and C. Zannoni, *ChemPhysChem*, 2009, **10**, 125-136.

7 I. Cacelli, A. Cimoli, L. De Gaetani, G. Prampolini and A. Tani, *J. Chem. Theory Comput.*, 2009, **5**, 1865–1876.

8 D. J. Earl, M. A. Osipov, H. Takezoe, Y. Takanishi and M. R. Wilson, *Phys. Rev. E*, 2005, **71**, 021706

9 J. Pelaez and M. Wilson, *Phys. Rev. Lett.*, 2006, **97**, 267801.

10 O. Francescangeli, V. Stanic, S. I. Torgova, A. Strigazzi, N. Scaramuzza, C. Ferrero, I. P. Dolbnya, T. M. Weiss, R. Berardi, L. Muccioli, S. Orlandi and C. Zannoni, *Adv. Funct. Mater.*, 2009, **19**, 2592-2600.

11 D. Chen, J. H. Porada, J. B. Hooper, A. Klittnick, Y. Shen, M. R. Tuchband, E. Korblova, D. Bedrov, D. M. Walba, M. A. Glaser, J. E. Maclennan and N. A. Clark, *Proc. Natl. Acad. Sci. U.S.A.*, 2013, **110**, 15931–15936.

12 M. P. Allen and A. J. Masters, *J. Mater. Chem.*, 2001, **11**, 2678-2689.

13 D. L. Cheung, S. J. Clark and M. R. Wilson, *J. Chem. Phys.*, 2004, **121**, 9131-9139.

14 A.A. Joshi, J. K. Whitmer, O. Guzmán, N. L. Abbott and J. J. de Pablo, *Soft Matter*, 2014,**10**, 882- 893.

15 A. Poniewierski and J. Stecki, *Mol. Phys.*, 1979, **38**, 1931-1940.

16 A. M. Somoza and P. Tarazona, *Mol. Phys.*, 1991, **72**, 927-939.

17 N. H. Phuong, G. Germano and F. Schmid, *J. Chem. Phys.*, 2001, **115**, 7227-7233.

18 J. Stelzer, R. Berardi and C. Zannoni, *Chem Phys. Lett.*, 1999, **299**, 9-16.

19 A. Ferrarini, *Phys. Rev. E*, 2001, **64**, 021710.

20 A. Ferrarini, C. Greco and G. R. Luckhurst, *J. Mater. Chem.*, 2007, **17**, 1039-1042.

21 M. Cestari, PhD Thesis, University of Padova, 2009.

22 M. Cestari, A. Bosco and A. Ferrarini, *J. Chem. Phys.*, 2009, **131**, 054104.

23 M. Cestari, E. Frezza, A. Ferrarini and G. R. Luckhurst, *J. Mater. Chem.*, 2011, **21**, 12303- 12308.

24 A. Ferrarini, G. J. Moro, P.L. Nordio and G. R. Luckhurst, *Mol. Phys.*, 1992, **77**, 1-15.

25 M. Cestari and A. Ferrarini, *Soft Matter*, 2009, **5**, 3879-3887.

26 P. W. Flory, *Statistical Mechanics of Chain Molecules*, Wiley-Interscience, New York, 1969.

27 C. J. F. Böttcher, *Theory of Electric Polarization*, Elsevier, Amsterdam, 1973.

28 (a) Gaussian 09, Revision B.01. (b) Gaussian 03, Revision D.02. M. J. Frish et al., Gaussian, Inc., Wallingford CT, 2009.

29 A. D. Becke, *J. Chem. Phys.*, 1993, **98**, 5648-5652.

30 P. J. Stephens, F. J. Devlin, M. J. Frisch and C. F. Chabalowski, *J. Phys. Chem.*, 1994, **98**, 11623-11627.

31 C. Bayly, P. Cieplak, W. Cornell and P. A. Kollman, *J. Phys. Chem.*, 1993, **97**, 10269-10280.

32 J. Wang, R. M. Wolf, J. W. Caldwell, P. A. Kollman and D. A. Case, *J. Comput. Chem.*, 2004, **25**, 1157-1174.

33 F. Jensen, *Introduction to Computational Chemistry*, Wiley, Chichester, 2007.

34 Y. Zhao and D. G. Truhlar, *Theor. Chem. Account*, 2008, **120**, 215-241.

35 B. J. Lynch, Y. Zhao and D. G. Truhlar, *J. Phys. Chem. A*, 2003, **107**, 1384-1388.

36 S. Grimme, WIREs *Comput. Mol. Sci*, 2011, **1**, 211–228.

37 E. Hohenstein, S. T. Chill and C. D. Sherrill, *J. Chem Theory Comput.*, 2008, **4**, 1996-2000.

38 N. Metropolis, A. Rosenbluth, M. Rosenbluth, N. Marshall, A. Teller and E. Teller, *J. Chem. Phys.*, 1953, **21**, 1087 –1092.

39 A. Ferrarini, G. R. Luckhurst and P. L. Nordio, *Mol. Phys.*, 1995, **85**, 131 –143.

40 M. Stocchero, A. Ferrarini, G. J. Moro and D. A. Dunmur, *J. Chem. Phys.*, 2004, **121**, 8079– 8097.

41 *Handbook of Chemistry and Physics*, ed. D. R. Lide, CRC Press, Boca Raton, 1996.

42 M. F. Sanner, J. C. Spehner and A. J. Olson, *Biopolymers*, 1996, **38**, 305 –320.

Chapter 6

From the molecular structure to spectroscopic and material properties: the bent-core compound A131 as case study*

6.1 Introduction

Here the IM methodology (see Chapter 5) is used to investigate the uniaxial nematic phase of the bent-core mesogen A131 (Figure 6.1). This system has been the object of several investigations by different experimental techniques, probing the phase properties both at the molecular and the macroscopic level [1-7]. Besides being interesting on its own, this system represents a good case study to show the ability of the IM approach to consistently describe properties at different length scales. In particular, we focus on the ^{13}C NMR chemical shifts, which are related to molecular orientational order parameters, and on the Frank elastic constants. In Section 6.2 we report the details of the computational procedure. In Section 6.3 the results obtained for the various properties investigated are presented and discussed in the light of the available experimental data.

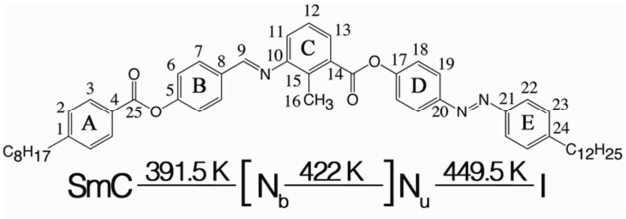

Figure 6.1. Chemical structure of A131 with carbon numbering. I, N_u, N_b and SmC denote the isotropic, the uniaxial nematic, the presumed biaxial nematic and the smectic C phase, respectively.

* This Chapter is adapted from C. Greco, A. Marini, E. Frezza and A. Ferrarini, *ChemPhysChem*, 2014, **15**, 1336-1344. © 2014 Wiley-VCH Verlag GmbH & Co. KGaA, Weinheim. NMR data were kindly provided by Prof. Ronald Y. Dong, University of British Columbia, Vancouver.

6.2 Computational details

The general features of the IM computational procedure have been described in Chapter 5. Here only the aspects specifically related to the system under investigation will be presented.

6.2.1 Molecular geometry and torsional potentials

The geometric parameters and torsional potentials of A131 were obtained by quantum mechanical DFT calculations [8]. Figure 6.2 (left) shows the molecular structure of A131 with the rotating bonds located in the five-ring core and in the alkyl chains. The overall shape of the aromatic core depends on the value of the dihedral angles C_9–N–C_{10}–C_{11} and C_{13}–C_{14}–C=O flanking the central aromatic ring (see Figure 6.1 for atom numbering), which are denoted as χ_{24} and χ_{25} respectively. A special role of the geometry around the central ring, which is determined by the constraints imposed by the local chemical structure [9], is recognized as a typical feature of bent-core mesogens [10,11]. According to previous computations [12,13], the torsional potential for the dihedral angle χ_{24} is characterized by two degenerate minima (χ_{24} ~ ± 45°); for each of them four states were identified for χ_{25} (~ ± 15° and ~ ± 165°). Thus, there is a total of eight symmetry-related configurations of the core, henceforth denoted as $\mathbf{\Gamma}_1$–$\mathbf{\Gamma}_8$. They are sketched in Figure 6.2 (right) and their relevant structural and energetic parameters are summarized in Table 6.1. The description of core configurations arising from rotation around χ_{24} and χ_{25} in terms of the rotational isomeric state approximation (RIS) [15] is justified by the fact that the potential energy minima are relatively narrow and separated by high barriers [12]. This description is also beneficial for the present study, as the identification of a small number of core geometries simplifies the analysis of the relationship between the molecular structure and the physical properties of interest. Therefore, it is kept throughout this work, and molecular conformations are grouped into discrete sets, each corresponding to a given core configuration. Thus, when speaking of the $\mathbf{\Gamma}_i$ set, we refer to the group of molecular conformations having the core in the $\mathbf{\Gamma}_i$ configuration and any possible value of the dihedrals different from χ_{24} and χ_{25}.

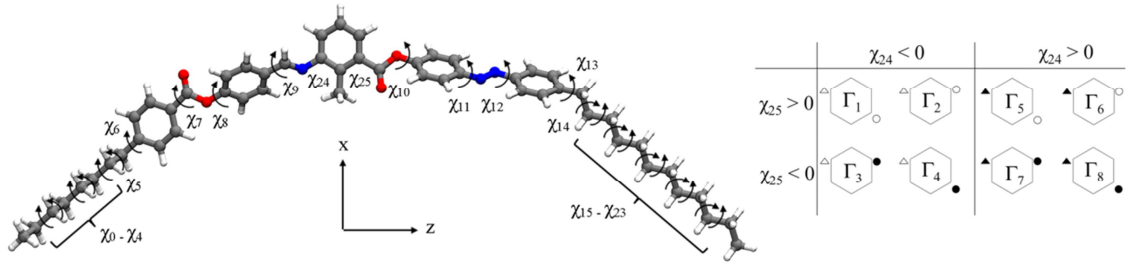

Figure 6.2. Left: molecular structure of A131; χ_i are the rotating dihedrals and $\{x,y,z\}$ is the molecular frame, with x parallel to the *para* axis of the central ring and y perpendicular to the plane of this ring. Right: representation of the different configurations of the core of A131. The hexagon represents the central ring; open and filled symbols are used for the iminic hydrogen, linked to the carbon C_9 (triangle) and the carbonylic oxygen (circle), above and below the plane of the central ring, respectively. Core configurations are defined as in Ref. [13] but, according to the IUPAC recommendation [14], the opposite convention is used for the sign of χ_{24} and χ_{25} (therefore the sign of the two dihedrals is the opposite of that of ϕ_4 and ϕ_5 in Figure 3 of Ref. [13]).

Configuration	χ_{24} (°)[(a)]	χ_{25} (°)[(a)]	ΔV (kJ/mol) [(b)]
Γ_1	- 44	+ 165	0.0
Γ_2	- 45	+ 18	4.5
Γ_3	- 45	- 17	5.9
Γ_4	- 45	- 166	1.7
Γ_5	+ 44	+ 166	1.7
Γ_6	+ 45	+ 17	5.9
Γ_7	+ 45	- 18	4.5
Γ_8	+ 44	- 165	0.0

Table 6.1. Structural and energetic parameters for the eight core configurations of A131, as obtained by DFT calculations at the B3LYP/6-31+G* level in vacuum (from Ref. [13]). [(a)] Dihedral angles are defined as positive for clockwise rotation [14] (this is the opposite of the convention used in Ref. [13]).
[(b)] Relative energies are defined with respect to the most stable configuration.

Atomic coordinates for each of the Γ_i core configurations were obtained by geometry optimization at the B3LYP/6-31+G* level [13]. Torsional energy profiles for the bonds indicated by arrows in Figure 2 were derived by relaxed scans on selected fragments and are reported in Appendix A. Different levels of the theory were used, as explained in the following. For the alkyl chain dihedrals (χ_0-χ_4, χ_5, χ_6 and their analogues in the other side arm), calculations were done at the M06-2X/6-31+G** level of theory (Figures A.1 and A.3) [16]. According to a recent computational analysis of the conformational preferences of butylbenzene, the M06-2X functional gives results that

are in better agreement with experiments than the B3LYP functional [17]. The torsional potential for χ_8 and χ_{10} was calculated at the M06-2X/6-31+G** level, using 4-methylphenyl 4-methylbenzoate as a model compound (Figure A.5(j)). The potential energy surface of phenyl benzoate has been the subject of intense investigation, and some discrepancies exist between the different calculations as to the exact position of the minima and the relative height of barriers [18-20]. However, in all cases four equivalent energy minima are found (~ ± 60°, ~ ± 120°) and the energy barriers at 0° and 180° are higher than those at ± 90°. The torsional profile calculated in this work substantially agrees with those obtained at the B3LYP/6-31+G*[18,19] or the MP2/6–31+G** and MP2/6–31+G* levels [18-20]. The χ_7 and χ_9 dihedrals are characterized by relatively simple torsional potentials, for which the standard B3LYP functional was used with the 6–31+G* basis set (Figures A.5(i) and A.7). For χ_{11} and χ_{12} the same torsional potential was assumed (Figure A.8).

The full account of the molecular flexibility (including lateral chains) is the main difference between ours and previous computational investigations of A131, which were restricted to a few conformers of the core [13].

6.2.2 Monte Carlo sampling and orientational-conformational averages

In generating conformations with Monte Carlo sampling, the full torsional potentials were used (see Section 5.3). The χ_{24} and χ_{25} dihedrals were not sampled since, for convenience of analysis and computation, separate calculations were performed for each of the core configurations schematized in Figure 6.2. Actually, in the light of the molecular symmetry, only the $\mathbf{\Gamma}_1$–$\mathbf{\Gamma}_4$ sets were considered. Over 50000 conformations were sampled for each core configuration, to guarantee convergence of all the investigated properties. A lower number would have been enough for most properties, with the exception of the bend elastic constant which, being strongly sensitive to molecular shape, can exhibit large fluctuations from one conformation to another. Final averages of the investigated properties were calculated including all core configurations. Only in some cases partial averages, restricted to conformations having a specific core configuration, were considered; this is explicitly said in Section 6.3.

Properties were calculated as a function of the orienting strength ε (see Eq. 5.1): to

make the comparison with experimental data easier, some of the results are reported as a function of temperature. To relate ε to temperature, a linear dependence of the chemical shifts calculated for C_5 on temperature was assumed, as observed experimentally for this carbon in the range between 445 and 406 K.

6.2.3 ^{13}C NMR chemical shifts

In ^{13}C NMR experiments, the relative shieldings of ^{13}C nuclei, known as chemical shifts, are measured. Henceforth these are denoted by $\langle\delta\rangle$, that is, the average value of the symmetric part of the chemical shift tensor, $\boldsymbol{\delta}$. This average is conveniently expressed in terms of the order parameters for the principal axes of the tensor [21]. Hence, for the *i*th nucleus we can write:

$$\left\langle \delta^i \right\rangle = \delta^i_{iso} + \frac{2}{3}\left[\left(\delta^i_{33} - \frac{\delta^i_{22}+\delta^i_{11}}{2}\right)S^i_{33} + \frac{1}{2}(\delta^i_{22}-\delta^i_{11})(S^i_{22}-S^i_{11})\right] \quad , \tag{6.1}$$

where δ^i_{jj} (j=1–3) are the principal values of the chemical shift tensor, S^i_{jj} are the orientational order parameters for the corresponding principal axes, and $\delta^i_{iso} = \left\langle Tr\boldsymbol{\delta}^i \right\rangle / 3$.

6.3 Results and Discussion

6.3.1 Molecular shape and conformational distribution

Figure 6.3, showing the molecular geometry of conformers with the core in $\boldsymbol{\Gamma}_1$–$\boldsymbol{\Gamma}_4$ configurations and all-*trans* alkyl chains, illustrates the importance of the χ_{24} and χ_{25} dihedrals. The overall shape of the $\boldsymbol{\Gamma}_2$ and $\boldsymbol{\Gamma}_3$ structures is clearly more bent than that of the $\boldsymbol{\Gamma}_1$ and $\boldsymbol{\Gamma}_4$ structures. For this reason in previous works they were denoted as hockey-stick-shaped and banana-shaped, respectively [13]. The bend angle, which we defined as the angle between the *para* axes of the *AE* rings (see Figure 6.1), is about 135° for the $\boldsymbol{\Gamma}_1$ and $\boldsymbol{\Gamma}_4$ core configurations and 115° for $\boldsymbol{\Gamma}_2$ and $\boldsymbol{\Gamma}_3$. Analogous values were found for the bend angle between the *para* axes of the *BD* rings in the $\boldsymbol{\Gamma}_1$ and $\boldsymbol{\Gamma}_4$ and in the $\boldsymbol{\Gamma}_2$ and $\boldsymbol{\Gamma}_3$ core configurations, respectively. The torsional freedom within the aromatic core does not significantly change the core shape within a given $\boldsymbol{\Gamma}_i$ set. Due to the form of

the torsional potentials for bonds within the core, the *B* ring, on one side, and the *D*, *E* rings, on the other side, tend to be twisted with respect to the central *C* ring, with twist angles of about ± 45° and ± 50°, respectively. A wider angular distribution is predicted for ring *A*, as relatively low energy barriers oppose its rotation with respect to ring *B*.

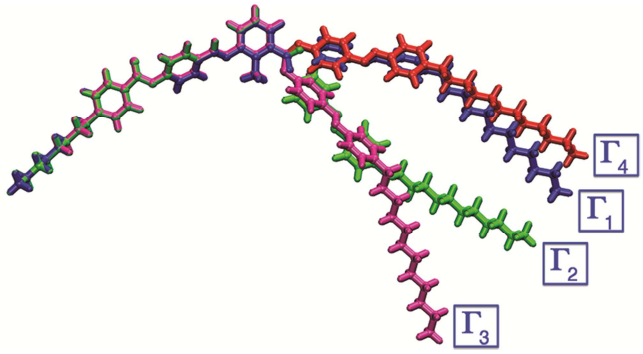

Figure 6.3. Superposition of four conformers of A131, with the core in $\mathbf{\Gamma}_1$–$\mathbf{\Gamma}_4$ configurations and all-*trans* alkyl chains.

According to the torsional potentials for the χ_6 and χ_{13} dihedrals, alkyl chains tend to lie perpendicular to the benzene ring to which they are attached, so protruding out of the approximate molecular plane, defined by the aromatic core. Rotations around chain bonds can significantly modify the overall molecular shape. To quantify these changes we calculated the size and shape distribution of molecular conformations. To this purpose the smallest rectangular box containing each conformer, with the edges parallel to its principal inertia axes, was considered. Thus, the length (*L*), breadth (*B*), and width (*W*) were taken equal to the largest differences between the atomic coordinates along each side. Figure 6.4 shows the *L*, *B*, *W* distributions calculated for the $\mathbf{\Gamma}_1$ and $\mathbf{\Gamma}_2$ sets, in the isotropic and in the nematic phase. The outer edges of the *L* distributions correspond to the end-to-end distance (measured between the terminal methyl carbons) in all-*trans* conformers: depending on the values of the χ_6 and χ_{13} dihedrals, this distance can reach up to 5.2 nm for the $\mathbf{\Gamma}_1$ and 4.8 nm for the $\mathbf{\Gamma}_2$ core configuration. In Figure 6.4 we can see that, even though the distributions are broadened by the chain mobility, the molecular shape remains strongly anisometric, with some difference between the $\mathbf{\Gamma}_1$ and $\mathbf{\Gamma}_2$ sets. On the average, conformations having the core in the $\mathbf{\Gamma}_2$ configuration are less elongated and more biaxial (larger difference between breadth and width) than those with the core in the $\mathbf{\Gamma}_1$ configuration. In the nematic phase, the maxima of the *L* distribu-

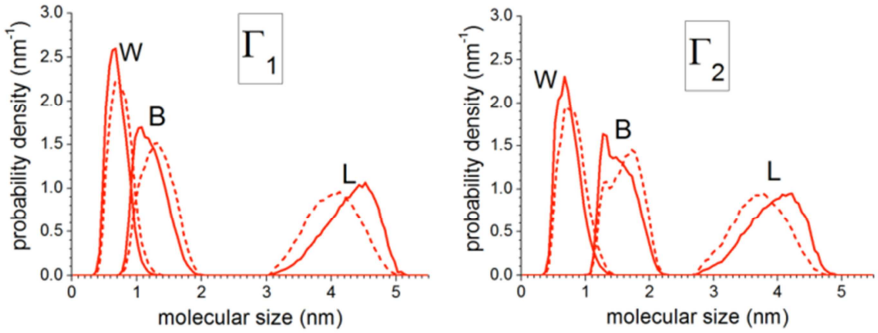

Figure 6.4. Distribution of length *L*, breadth *B* and width *W* calculated separately for the Γ_1 (left) and Γ_2 (right) sets of conformations, in the isotropic phase at T=450 K (dashed lines) and in the nematic phase at T=395 K (solid lines).

tions are shifted towards higher values, as a consequence of the stabilization of the more elongated molecular conformations within a given Γ_i set.

Table 6.2 reports the relative weight *w* of each Γ_i core configuration, calculated according to Eq. 5.10, which takes into account the effect of both the torsional potential and the molecular field potential. We can see that effect of the nematic environment does not dramatically modify these weights. The population of the Γ_2 and Γ_3 configurations, already low in the isotropic phase at 450 K, becomes even lower with

Configuration	450 K (I)	425 K (N)	395 K (N)
$\Gamma_1 = \Gamma_8$	0.23	0.26	0.29
$\Gamma_2 = \Gamma_7$	0.07	0.05	0.03
$\Gamma_3 = \Gamma_6$	0.05	0.03	0.02
$\Gamma_4 = \Gamma_5$	0.15	0.16	0.16

Table 6.2. Weights of the Γ_i core configurations of A131, calculated at different temperatures in the isotropic (I) and in the nematic (N) phase, according to Eq. 5.10 of Chapter 5.

decreasing temperature, in favour of the Γ_1 and Γ_4 configurations. These do not only have a lower energy in vacuum (see Table 6.1), but also, being more elongated, are stabilized by the interaction with the nematic environment. Thus, according to our calculations, hockey-stick-shaped conformers would have a low relative weight in the uniaxial nematic phase of A131, which becomes even smaller with decreasing temperature.

6.3.2 ^{13}C NMR chemical shifts and order parameters

^{13}C NMR chemical shifts were calculated according to Eq. (6.1), using experimental chemical shielding tensors for all carbons with the exception of C_1, C_{15}, and C_{24}, for which only the isotropic value, δ_{iso}^{i}, is available [22]. For these sites, theoretical tensor components (GIAO-DFT) were used [13]. The NMR spectral assignments reported in Ref. [22] were revised in the light of the results of our calculations. Indeed, the ^{13}C NMR spectrum of a complex molecule such as A131 is characterized by crowding of several peaks in a reduced spectral region [22], and the assignment necessarily has some degree of arbitrariness. The plots in Figure 6.5 show the calculated and the measured chemical shifts as a function of the shifted temperature T–T_{NI}, where T_{NI} is the isotropic-nematic transition temperature.

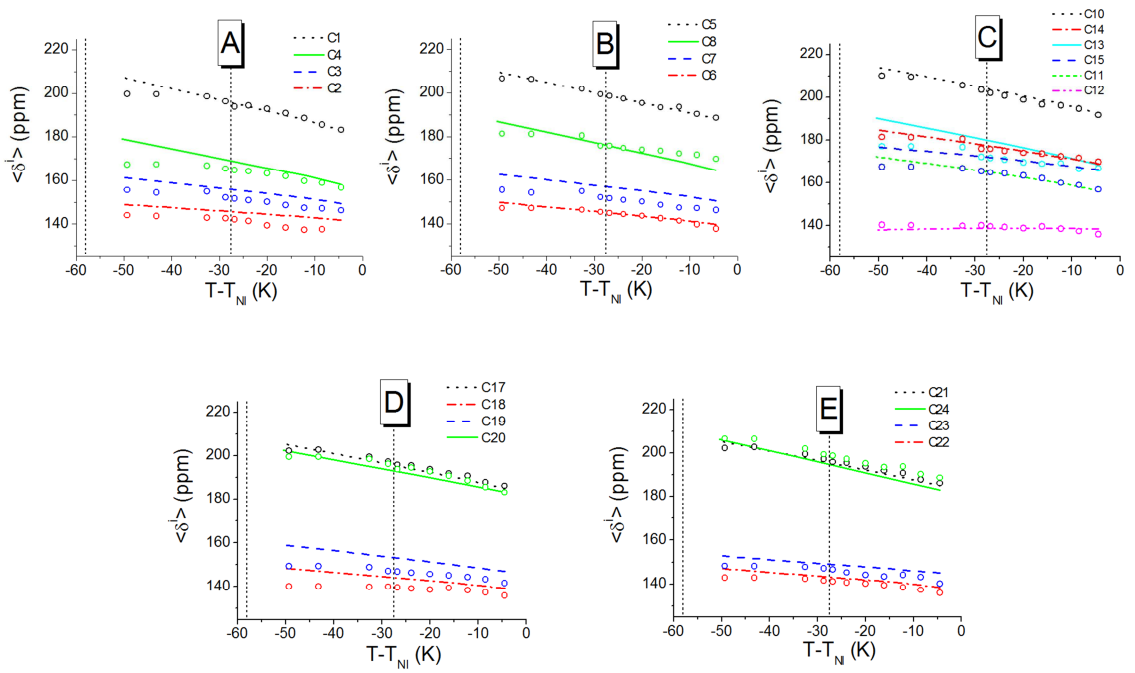

Figure 6.5. ^{13}C NMR chemical shifts for the aromatic rings of A131 as a function of the shifted temperature, T–T_{NI} : calculated (lines) and experimental values (symbols) [22]. Some of the assignments reported in Ref. [22] have been revised; the chemical shifts of C_{15} and C_{11} are now identical. The vertical lines indicate the presumed uniaxial–biaxal nematic transition and the nematic–smectic C transition. Site labelling is shown in Figure 6.1.

It may be worth stressing that our approach is methodologically different from other methods used for previous analyses of the ^{13}C NMR chemical shifts of A131, in which the experimental data were fitted to a model containing a number of fitting parameters

(typically order parameters for different parts of the molecule), which were then used a posteriori to interpret the orientational behavior [13, 22]. This results however must be taken with some prudence: depending on the spectral assignment, different sets of order parameters have been reported for A131, some of them clearly not consistent with the molecular structure [13,22]. Here, on the contrary, we started modeling the orientational and conformational distribution of the mesogen and the effects of the molecular geometry are introduced a priori. Chemical shifts, as well as any other property of the nematic phase, are obtained as a function of the orienting strength ε, without free parameters. Here we used the experimental chemical shifts of C_5 to define the relation between ε and temperature, to report our results as a function of temperature, which makes the comparison with experimental data easier. However, this choice does not imply the agreement between theoretical and calculated chemical shifts, as the pattern of the $\langle \delta^i \rangle$ values is determined by the molecular geometry and the specific orientational preferences of the conformers. Therefore the results shown in Figure 6.5 can be taken as an assessment of the adequacy of our description of the molecular structure and our account of the conformational and orientational distribution for A131. Some discrepancy between theoretical and experimental results can be ascribed to uncertainty in the molecular geometry and in the principal values and axes of the chemical shift tensors used in the calculations. In general, relatively higher discrepancies are found for carbons for which theoretical, rather than experimental shielding tensors were used. An example is represented by C_{15}, the chemical shifts of which were overestimated, probably because of the too large $\boldsymbol{\delta}$ tensor values used in the calculations (theoretical δ_{iso} values equal to 142.4 for $\boldsymbol{\Gamma}_1$ and 137.6 for $\boldsymbol{\Gamma}_4$ compared to the experimental value of 134.5). We can discern in Figure 6.5 that the discrepancies between theoretical and experimental chemical shifts tend to increase on approaching the nematic-smectic C transition, which could be a sign of deviations from the standard nematic organization assumed in our description. Indeed, the transition to a biaxial nematic phase has been debated [1-5,7,13]; more recently the onset of smectic C-like short-range fluctuations has been suggested [6].

We have also calculated quantities that are not directly accessible to the experiment. For instance, the order parameters separately calculated for the $\boldsymbol{\Gamma}_1$ and $\boldsymbol{\Gamma}_2$ sets of

conformations (Figure 6.6) show significant differences, amenable to the different shape of the two groups of conformers (see Figure 6.3 and 6.4). For $\mathbf{\Gamma}_1$ conformations higher ordering is predicted, with a strong tendency to align their long *z* axis to the director (high S_{zz}) and very small biaxiality of molecular order (low $S_{xx} - S_{yy}$). The ordering behavior of $\mathbf{\Gamma}_2$ conformations is characterized by a lower tendency to align their *z* axis to the director and higher biaxiality of molecular order. The positive sign of the difference S_{xx} - S_{yy} , for both $\mathbf{\Gamma}_1$ and $\mathbf{\Gamma}_2$ conformations, indicates their preference to keep the director on the *xz* plane, which can be identified as the molecular plane.

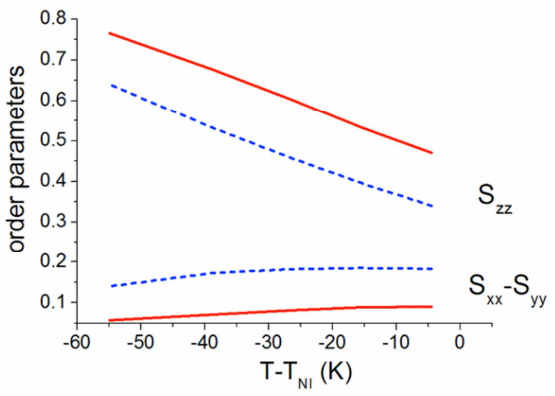

Figure 6.6. Order parameters, S_{zz} (top) and S_{xx} - S_{yy} (bottom), separately calculated for conformations of A131 having the core in the $\mathbf{\Gamma}_1$ (solid lines) and in the $\mathbf{\Gamma}_2$ (dashed lines) configuration, as a function of the shifted temperature, $T–T_{NI}$. For both configurations the {*x*,*y*,*z*} axes of the molecular frame, shown in Figure 6.2, are close to the principal axis systems of the molecular Saupe matrix.

6.3.3 Elastic constants

Figure 6.7 (solid lines) shows the splay (K_1), twist (K_2) and bend (K_3) elastic constants calculated for A131, as a function of temperature. Compared to the typical behaviour of conventional rod-like liquid crystals, remarkable differences appear. The elastic anisotropy, $K_3–K_1$, is negative, rather than positive. K_3 is unusually low and its temperature dependence cannot be described by the relationship $K_3 \propto S_{zz}^2$, customarily assumed for rod-like mesogens [23]. In order to understand the origin of this behaviour we considered the contribution given to K_3 by different molecular conformations. High and positive values were found for elongated conformers, and small or even negative values for bent-shaped ones. The balance between these different contributions gives rise, on average, to the low and almost temperature independent bending stiffness

predicted at higher temperatures. At lower temperature K_3 starts to decrease as a result of the steep decrease of the values coming from bent conformations. The special sensitivity of K_3 to the molecular curvature has already been evidenced for rod-like LCs [24] and especially for bent mesogenic dimers, for which even negative K_3 values have been predicted [25].

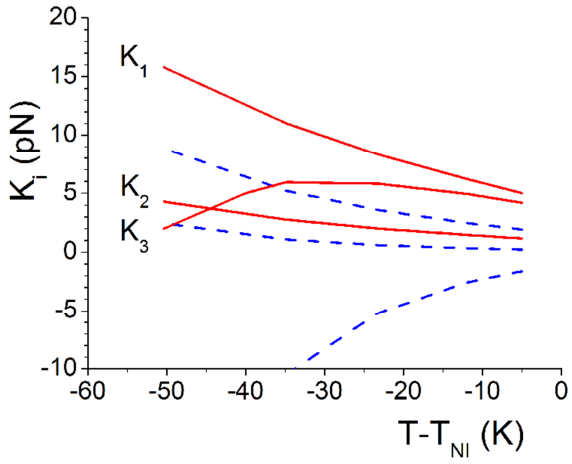

Figure 6.7. Elastic constants calculated for the nematic phase of A131 (solid lines). Dashed lines represent the results obtained for the restricted set of molecular conformations having the core in the $\mathbf{\Gamma}_2$ configuration (from top to bottom: K_1, K_2, K_3).

To illustrate the effect of the molecular structure, in Figure 6.7 we report, with dashed lines, the elastic constants calculated for the single set of molecular conformations having the core in the $\mathbf{\Gamma}_2$ configuration; similar results were obtained for the single $\mathbf{\Gamma}_3$ set. As described in Section 6.3.1 these conformations have a hockey-stick shape, with a narrow bend angle of 115°. The elastic constants predicted for banana-shaped conformers (sets $\mathbf{\Gamma}_1$ and $\mathbf{\Gamma}_4$, having a bend angle of 135°) are close to those obtained after averaging over all core configurations (due to the high statistical weight of $\mathbf{\Gamma}_1$ and $\mathbf{\Gamma}_4$ conformations). Once again the most striking differences are exhibited by K_3. For hockey-stick-shaped conformers strongly negative values are predicted, which would be incompatible with the existence of a stable nematic phase [26]. Our calculations may somehow overestimate the magnitude of these negative K_3 values, but they give a strong indication of the different contributions of banana-shaped and hockey-stick-shaped conformers to the bending stiffness. Due to the low relative weight of $\mathbf{\Gamma}_2$ and $\mathbf{\Gamma}_3$ conformations, the bend elastic constant obtained after averaging over all core

configurations remains positive; however, it would become rapidly negative upon increasing the amount of hockey-stick-shaped conformers. The influence of the bend angle on the phase behaviour of bent-core compounds is well known: the formation of the nematic phase is promoted by the introduction of substituents in suitable core positions, which stabilize conformations with wider bend angles [10,11]. The results obtained here for K_3 of the $\mathbf{\Gamma}_2$ conformations suggest that the bend angle can also have a critical role, up to now not sufficiently highlighted, for the stability of the nematic phase with respect to bend distorsions.

The elastic constants calculated for A131 can be compared with the measured K_1 and K_3 values, reported in Ref. [6]. Good agreement is found for the splay elastic constant: K_1 is high and shows an approximately linear dependence on temperature. For the bend elastic constant, theoretical predictions are in good agreement with the experimental trend in the temperature region far from the smectic C transition: $K_3 < K_1$ is found, with K_3 scarcely dependent on temperature. At low temperatures experimental data show a rapid increase of K_3: this behaviour cannot be predicted assuming a simple uniaxial nematic phase (see Figure 6.7). In Ref. [6] the divergence of K_3 has been ascribed to smectic C pretransitional short-range fluctuations. Phase biaxiality, which has been proposed for A131 [1,2a,2c,13] could not be the reason for the experimental behaviour, as relatively small contributions to the elastic constants are expected to arise from biaxial ordering [27,28].

6.4 Conclusions

In this work, we have presented a computational investigation of the nematic phase formed by the bent-core mesogen A131, based on an atomistic representation of the molecule combined with a molecular field model. We have shown that this is an affordable task and the capability to simultaneously analyse properties at different length scales can provide considerable insight, allowing us to check the consistency of hypotheses otherwise difficult to ascertain. The main results can be summarized as follows. We have calculated the ^{13}C NMR chemical shifts in the uniaxial nematic phase of A131 over a wide temperature range that extends from a few degrees below the nematic-isotropic transition downwards close to the transition to the smectic C phase. The comparison with the spectral signals reported in Ref. [22] has allowed us to revise

some assignment and to propose a consistent description of the molecular order in this system. We have found good agreement between experimental and theoretical chemical shifts over almost all the investigated temperature range. Some increase of the discrepancies upon lowering the temperature could be the effect of the pre-transitional SmC fluctuations that have been invoked to explain the low temperature behaviour of the bend-elastic constant.

The elastic constants predicted for A131, in agreement with the experimental data far from the smectic C transition, are different from those of typical low molar mass rod-like nematics. The most relevant feature is that K_3 is smaller than K_1 and remains almost constant over a wide temperature range: calculations have shown that this behaviour can be ascribed to the bent molecular shape. In ref. [29], it was argued that the molecular shape would not be sufficient to explain the unusually low K_3 of bent-core mesogens and the presence of cybotactic clusters was invoked. The results obtained here for A131 show that the bent molecular shape can indeed explain the unusual elastic properties. The experimental data for A131 show also a divergence of K_3 on moving towards the smectic C transition, which cannot be explained within the same framework. This kind of behaviour, however, does not seem to be a general feature for bent-core mesogens [30,31].

A valuable feature of our approach is the capability to relate phase properties to the conformational preferences of the mesogen. We have found that the two kinds of conformers of A131, evidenced by previous theoretical studies [13] and denoted as banana-shaped and hockey-stick-shaped, give quite different contributions not only to the molecular order parameters, but also to the elastic constants. However, the hockey-stick-shaped conformers do not significantly affect the properties of the system, given their low relative weight, which is around 10% and is even predicted to decrease with increasing order in the uniaxial nematic phase. A significant increase of these conformers, which has been proposed in Ref. [13] in connection with the presumed transition to a biaxial nematic phase, appears difficult to justify at the mean field level, unless short-range correlations are invoked. Thus, the features of the nematic phase are essentially determined by the banana-shaped conformers, which are elongated enough to allow for the existence of a nematic phase over a wide temperature range, and at the same time are bent enough to give this phase unconventional properties.

6.5 References

1 V. Prasad, S.-W. Kang, K. A. Suresh, L. Joshi, Q. Wang and S. Kumar, *J. Am. Chem. Soc.*, 2005, **127**, 17224–17227.

2 a) M. S. Park, B.-J. Yoon, J. O. Park, V. Prasad, S. Kumar and M. Srinivasarao, *Phys. Rev. Lett.*, 2010, **105**, 027801; b) H. F. Gleeson and P. D. Brimicombe, *Phys. Rev. Lett.*, 2011, **107**, 109801; c) M. S. Park, B.-J. Yoon, J. O. Park, V.Prasad, S. Kumar and M. Srinivasarao, *Phys. Rev. Lett.*, 2011, **107**, 109802.

3 K. V. Le, M. Mathews, M. Chambers, J. Harden, Q. Li, H. Takezoe and A. Jákli, *Phys. Rev. E*, 2009, **79**, 030701.

4 H. G. Yoon, S.-W. Kang, R. Y. Dong, A. Marini, K. A. Suresh, M. Srinivasarao and S. Kumar, *Phys. Rev. E*, 2010, **81**, 051706.

5 B. Senyuk, H. Wonderly, M. Mathews, Q. Li, S. V. Shiyanovskii and O. D. Lavrentovich, *Phys. Rev. E*, 2010, **82**, 041711.

6 P. Sathyanarayana, M. Mathews, Q. Li, V. S. S. Sastry, B. Kundu, K. V. Le, H. Takezoe and S. Dhara, *Phys. Rev. E*, 2010, **81**, 010702.

7 T. Ostapenko, C. Zhang, S. N. Sprunt, A. Jákli and J. T. Gleeson, *Phys. Rev. E*, 2011, **84**, 021705.

8 Gaussian 09 (Revision B.01), M. J. Frisch et al. Gaussian, Inc., Wallingford CT, 2010.

9 I. Cacelli and G. Prampolini, *Chem. Phys.*, 2005, **314**, 283– 290.

10 W. Weissflog, H. Nadasi, U. Dunemann, G. Pelzl, S. Diele, A. Eremin and H. Kresse, *J. Mater. Chem.*, 2001, **11**, 2748 – 2758.

11 C. Keith, A. Lehmann, U. Baumeister, M. Prehm and C. Tschierske, *Soft Matter*, 2010, **6**, 1704– 1721.

12 A. Marini, V. Prasad and R. Y. Dong, in *Nuclear Magnetic Resonance Spectroscopy of Liquid Crystals*, ed. R. Y. Dong), World Scientific, Singapore, 2009, ch. 13.

13 R. Y. Dong and A. Marini, *J. Phys. Chem. B*, 2009, **113**, 14062 –14072.

14 G. P. Moss, *Pure Appl. Chem.*, 1996, **68**, 2193 – 2222.

15 P. W. Flory, *Statistical Mechanics of Chain Molecules*, Wiley-Interscience, New York, 1969.

16 Y. Zhao and D. G. Truhlar, *Theor. Chem. Acc.*, 2008, **120**, 215-241.

17 S. Halbert, C. Clavaguéra and G. Bouchoux, *J. Comput. Chem.*, 2011, **32**, 1550 - 1560.

18 R. Wrzalik, K. Merkel and A. Kocot, *J. Mol. Model.*, 2003, **9**, 248– 258.

19 G. Cinacchi, G. Prampolini, *J. Phys. Chem. A*, 2005, **109**, 6290 –6293.

20 S. Kawauchi, S.-W. Choi, K. Fukuda, K. Kishikawa, J. Watanabe and H. Takezoe, *Chem. Lett.*, 2007, **36**, 750 –751.

21 P. L. Nordio and U. Segre, in *The Molecular Physics of Liquid Crystals*, ed. G. R. Luckhurst and G. W. Gray, Academic, New York, 1979.

22 R. Y. Dong, S. Kumar, V. Prasad and J. Zhang, *Chem. Phys. Lett.*, 2007, **448**, 54–60.

23 A. Ferrarini, *Liq. Cryst.*, 2010, **37**, 811 –823.

24 M. Cestari and A. Ferrarini, *Soft Matter*, 2009, **5**, 3879 –3887.

25 M. Cestari, E. Frezza, A. Ferrarini and G. R. Luckhurst, *J. Mater. Chem.*, 2011, **21**, 12303 – 12308.

26 J. L. Ericksen, *Phys. Fluids*, 1966, **9**, 1205– 1207.

27 Y. Singh, K. Rajesh and V. J. Menon, *Phys. Rev. E*, 1994, **49**, 501 –512.

28 A. Kapanowski, *Phys. Rev. E*, 1997, **55**, 7090 – 7104.

29 M. Majumdar, P. Salamon, A. Jákli, J. Gleeson, S. Sprunt, Phys. Rev. E 2011, **83**, 031701.

30 P. Tadapatri, U. S. Hiremath, C. V. Yelamaggad and K. S. Krishnamurthy, *J. Phys. Chem. B*, 2010, **114**, 1745 –1750.

31 N. Avci, V. Borshch, D. D. Sarkar, R. Deb, G. Venkatesh, T. Turiv, S. V. Shiyanovskii, N. V. S. Rao and O. D. Lavrentovich, *Soft Matter*, 2013, **9**, 1066 –1075.

Chapter 7

Elastic and flexoelectric properties of bent-core nematics*

7.1 Introduction

As described in Chapter 2, nematic liquid crystals of bent-core molecules (BCNs) exhibit unconventional elastic and flexoelectric properties, which remain the object of debate. The microscopic origin of their low bending stiffness is not fully understood [1-7]. Due to their bent shape, BCNs were proposed to be good candidates for high flexoelectric couplings, and there has even been a claim of a giant effect [10]. This observation has not been confirmed by other measurements [4,6,11,12] and flexoelectricity of bent-core systems remains an open issue of [8,9]. New experimental and computational efforts are clearly needed to get new insight into the relationship between the molecular structure and the elastic and flexoelectric properties of BCNs.

In the previous Chapter, a computational study of a bent-core compound, A131, was presented: there we could draw some preliminary conclusions about the unconventional elastic behaviour, highlighting the crucial role of a properly-bent shape. In this Chapter we present the results of a combined experimental and computational investigation of the elastic and flexoelectric properties of various bent-core compounds with different chemical structures. Experiments were carried out by the group of Prof.

* This Chapter is adapted from: (a) S. Kaur, J. Addis, C. Greco, A. Ferrarini, V. Görtz, J.W. Goodby and H.F. Gleeson., *Phys. Rev. E*, 2012, **86**, 041703. © 2012 American Physical Society (b) S. Kaur, L. Tian, H. Liu, C. Greco, A. Ferrarini, J. Seltmann, M. Lehmann and H.F. Gleeson, *J. Mater. Chem. C*, 2013, **1**, 2416-2425. © 2013 The Royal Society of Chemistry. (c) S. Kaur, H. Liu, J. Addis, C. Greco, A. Ferrarini, V. Görtz, J.W. Goodby and H.F. Gleeson, *J. Mater. Chem. C*, 2013, **1**, 6667-6676. © 2013 The Royal Society of Chemistry. (d) S. Kaur, V. P. Panov, C. Greco, A. Ferrarini, V. Görtz, J.W. Goodby and H. F. Gleeson, *Appl. Phys. Lett.*, 2014, **105**, 223505 © 2014 American Institute of Physics.

H. F. Gleeson, Manchester University [13-16]. Two kinds of systems with different aromatic cores were considered: a series of 1,3,4-oxadiazole derivatives, with various terminal chains and peripheral substituents (Figure 7.1(a)), and a 1,3,4-thiadiazole compound (Figure 7.1(b)). Apparently these systems have a similar (bent) molecular shape, suggesting that their elastic properties should also be qualitatively similar. However, as will be shown in the following paragraphs, the experimentally determined elastic constants of the oxadiazole and thiadiazole materials exhibit a markedly different behaviour. On the contrary, the chemical variations across the series of oxadiazole compounds were observed to have little influence on their elastic properties. Calculations were performed to shed light on the origin of these differences and to identify the main molecular determinants of the unusual elastic behaviour of BCNs.

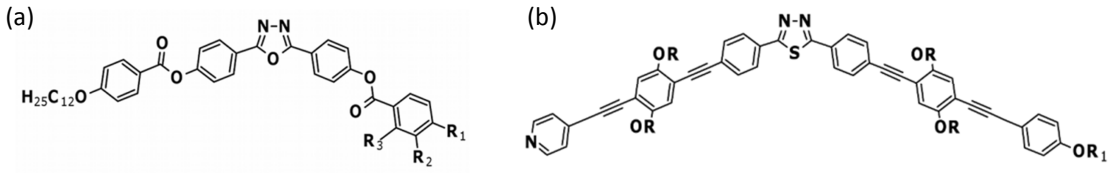

1: $R_1 = C_{12}H_{25}O$, $R_2 = R_3 = H$ Iso 217.7°C N 203.6 °C SmC
2: $R_1 = C_9H_{19}O$, $R_2 = R_3 = F$ Iso 221.4°C N 206.0 °C SmC
3: $R_1 = C_9H_{19}O$, $R_2 = R_3 = H$ Iso 236.6°C N 204.6 °C SmX
4: $R_1 = C_5H_{11}$, $R_2 = R_3 = H$ Iso 239.6°C N 184.6 °C DC

$R=C_6H_{13}$, $R_1=C_6H_{12}COOC_2H_5$ Iso 154.7°C N 90.9°C Cr

Figure 7.1 Chemical structure and phase transitions of (a) the oxadiazole derivatives **1**-**4,** (b) the thiadiazole derivative. Iso = Isotropic, N= Nematic, SmC = Smectic C, SmX = Smectic X, DC = Dark Conglomerate, Cr = Crystal.

Investigation of flexoelectricity was carried out for the oxadiazole derivative **4** (Figure 7.1 (a)): from the experiments the magnitude of the difference between the splay (e_1) and bend (e_3) flexoelectric coefficients, $|e_1 - e_3|$, and its temperature dependence were determined. Our calculations provided additional information on the individual flexoelectric coefficients, and on their dipolar and quadrupolar contribution, thus enabling a detailed interpretation of the experimental behaviour. Moreover, based on our calculations we could draw some general considerations on the flexoelectric properties of bent-core liquid crystals.

In section 7.2 we will outline the measurement techniques employed and summarize the experimental findings. The details of the calculations will be given in Section 7.3. The experimental and computational results will be compared and discussed in Section 7.4.

7.2 Experimental findings

7.2.1 Elastic constants of oxadiazole and thiadiazole bent-core LCs

Elastic constants were determined from the variation of the capacitance of a LC cell in response to electric field induced Freedericksz transitions [17]. The latter consist in a reorientation of the director **n** of a surface-aligned nematic sample upon application of an electric field. The reorientation process occurs only above a certain threshold voltage as a result of the balance between dielectric torques, which drive the transition, and elastic torques, which oppose the deformation: the elastic constants can thus be obtained from the analysis of the threshold characteristics.

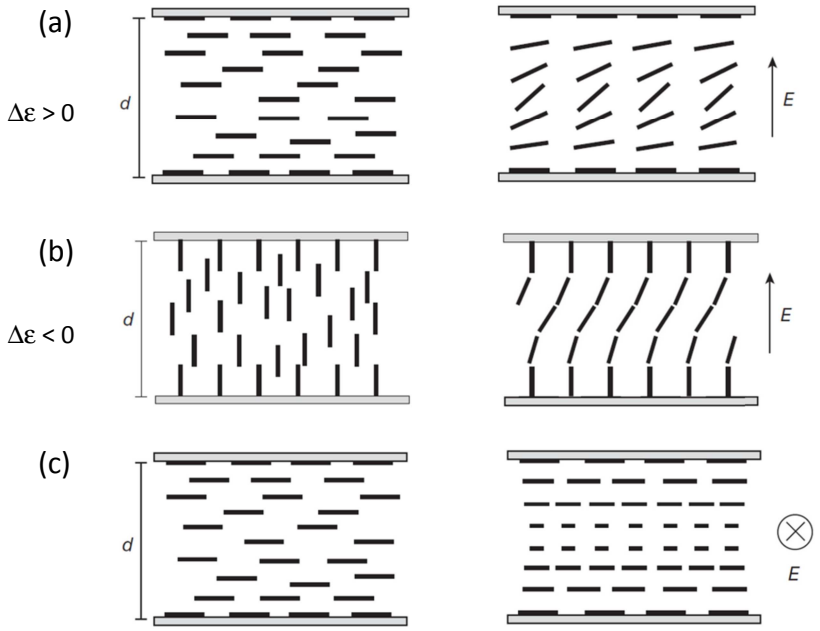

Figure 7.2. Freedericksz transition method to measure elastic constants: (a) splay (K_{11}), (b) bend (K_{33}), (c) twist (K_{22}). *E* is the electric field and *d* is the cell thickness. Adapted from [17].

For measurements of the splay (K_{11}) and bend (K_{33}) elastic constants, the electric field is applied perpendicular to the cell plates (see Figure 7.2(a)-(b)). Depending on the sign of the dielectric anisotropy of the material, $\Delta\varepsilon = \varepsilon_{\parallel} - \varepsilon_{\perp}$, different cell geometries are required: planar anchoring for $\Delta\varepsilon > 0$ (Figure 7.2(a)), homeotropic anchoring for $\Delta\varepsilon < 0$ (Figure 7.2(b)). The threshold voltage V_{th} is given by:

$$V_{th}^{K_{ii}} = \pi\left(\frac{K_{ii}}{\varepsilon_0 \Delta\varepsilon}\right)^{1/2} \qquad \begin{cases} i = 1 & \text{for} \quad \Delta\varepsilon > 0 \\ i = 3 & \text{for} \quad \Delta\varepsilon < 0 \end{cases}, \tag{7.1}$$

where ε_0 is the vacuum permittivity. Therefore either K_{11} or K_{33} can be determined from measurement of V_{th}, depending on the sign of $\Delta\varepsilon$. The other elastic modulus influences the steepness of the capacitance variation above threshold and is obtained from fitting of the corresponding voltage change [18].

The Freedericksz transition method in IPS (in-plane switching) cells was used for measurements of the twist elastic constant K_{22} (Figure 7.2(c)). In this geometry the electric field is parallel to the cell surfaces and, above a certain threshold, a twist of the director profile is induced. The threshold voltage V_{th} is related to K_{22} by [19]:

$$V_{th}^{K_{22}} = \frac{\pi L}{d}\left(\frac{K_{22}}{\varepsilon_0 \Delta\varepsilon}\right)^{1/2} \quad , \tag{7.2}$$

where d is the cell thickness and L is the electrode separation.

All the oxadiazole materials here investigated have $\Delta\varepsilon < 0$ [13,14]: as a consequence, measurement of the splay and bend elastic constants from Freedericksz transition requires homeotropic cell alignment. The elastic constants of compounds **2** and **4** were determined across the entire nematic regime (of about 15 K and 60 K respectively), whereas for compounds **1** and **3** measurements close to the underlying smectic phases were not possible because of the deterioration of the cell alignment. The thiadiazole derivative exhibits a dual-frequency behaviour (the sign of $\Delta\varepsilon$ changes with frequency of the applied electric field and temperature): measurements of the elastic constants for this compound were restricted to that part of the nematic range in which $\Delta\varepsilon > 0$, and planar cells were used [15].

Figure 7.3 (a)-(c) shows the elastic constants obtained for the oxadiazole derivatives **1**-**4** as a function of shifted temperature $T-T_{NI}$, where T_{NI} is the nematic-isotropic transition temperature. For all materials, the bend elastic constant K_{33} is found to be lower than the splay elastic constant K_{11}, in contrast to the typical behaviour of rod-like LCs, for which $K_{33} > K_{11} > K_{22}$. The values of all three elastic constants are almost undistinguishable for compounds **1**-**3**; slightly lower values were obtained for compound **4**. Measurements performed for compound **4** are of particular interest, since its nematic phase extends across about 60 K, allowing us to examine the elastic behaviour over a wide range of temperatures. Remarkably, the bend elastic constant K_{33} is found to be almost

independent of temperature, at variance with the behaviour of rod-like LCs, where K_{33} increases with decreasing temperature.

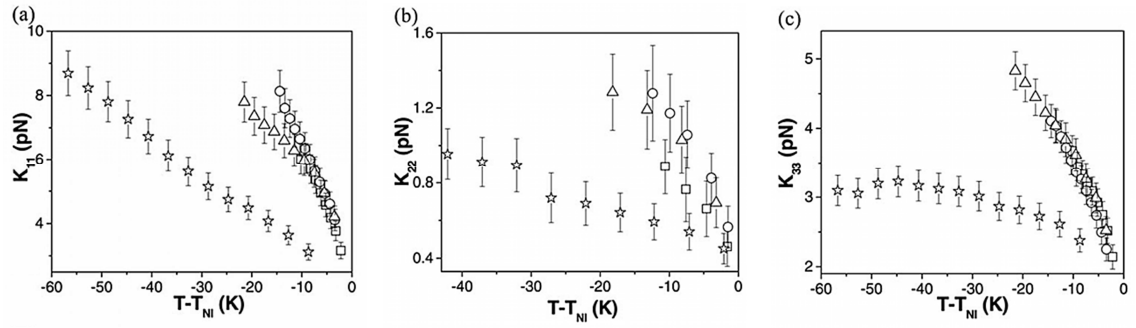

Figure 7.3 The experimental splay, K_{11} (a), twist K_{22} (b) and bend K_{33} (c) elastic constants as a function of shifted temperature, for the oxadiazole compounds **1** (squares) , **2** (circles), **3** (triangles) and **4** (stars).

The elasticity of the thiadiazole material (Figure 7.4) is quite different from that of the oxadiazole derivatives: at all temperatures $K_{33} > K_{11}$ is observed, analogous to the behaviour of rod-like LCs and in contrast to what reported to date for other bent-core materials, for which $K_{11} > K_{33}$ has been found, as for the oxadiazole derivatives here investigated [1-6].

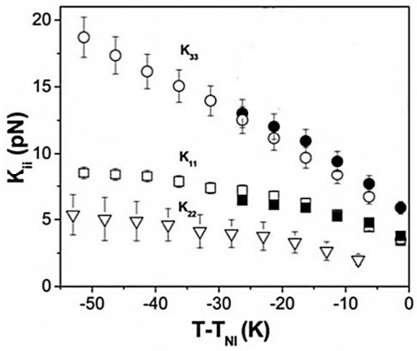

Figure 7.4. The experimental splay (K_{11}, squares), twist (K_{22}, triangles) and bend (K_{33}, circles) elastic constants as a function of shifted temperature, for the thiadiazole compound. Open and closed symbol refer to measurements carried out at 1kHz and 10Hz, respectively.

7.2.2 Flexoelectric coefficients of an oxadiazole bent-core LC

The magnitude of the difference between the splay and bend flexoelectric coefficients, $|e_1 - e_3|$, of the oxadiazole derivative **4** were obtained from the analysis of flexodomains. These are equilibrium patterns consisting in a spatially periodic modulation of the nematic director **n**, which are formed in planar cells upon application

of an electric field above a certain threshold [20]. They can be easily recognized under crossed polarizers, where the distorsion pattern appears as a series of optical stripes parallel to the rubbing direction of the cell plates (Figure 7.5(a)). The formation of flexodomains is driven by the free energy gain resulting from flexoelectric couplings. If a DC field is applied and the one elastic constant approximation (K_{11}=K_{22}=K) is adopted, the threshold voltage V_{th} and the wavenumber q_c of FDs are related to the flexoelectric difference $|e_1 - e_3|$ according to [20-23]:

$$V_{th} = \frac{2\pi K}{|e_1 - e_3|(1+\mu)} \tag{7.3}$$

$$q_c = \frac{\pi}{d}\sqrt{\frac{1-\mu}{1+\mu}} \quad , \tag{7.4}$$

where d is the cell gap, $\mu = \varepsilon_0 \Delta\varepsilon K / (e_1 - e_3)^2$, ε_0 is the vacuum permittivity and $\Delta\varepsilon = \varepsilon_{\parallel} - \varepsilon_{\perp}$ is the dielectric anisotropy of the liquid crystal. Eqs. (7.3)-(7.4) provide two independent measurements of $|e_1 - e_3|$.

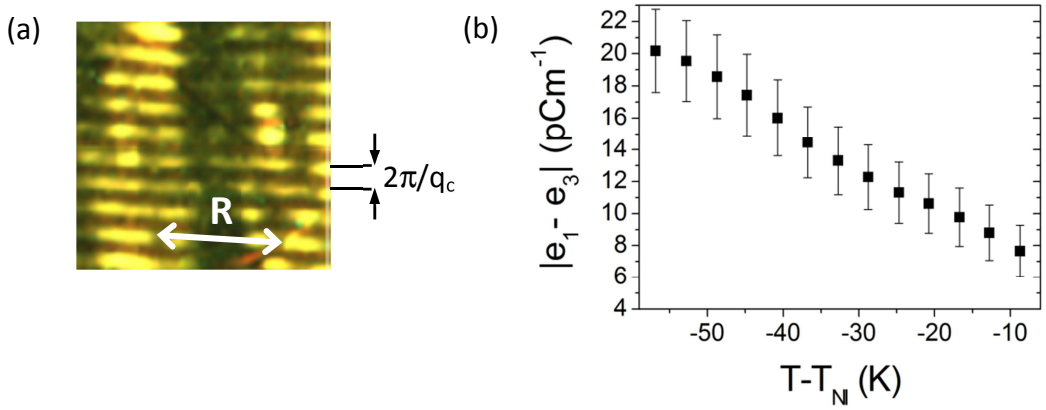

Figure 7.5. (a) Flexodomain patterns formed by the oxadiazole compound **4**, observed between crossed polarizers. The arrow indicates the cell rubbing direction. (b) The experimentally determined value of the flexoelectric difference for the same material, as a function of shifted temperature.

In this work an AC voltage with a low frequency of 10 Hz was applied, to avoid ionic conductivity contributions, in analogy to what commonly done in similar experiments [24]. Measurements were performed across the entire nematic regime. In using Eqs.

(7.3)-(7.4), $K = (K_{11} + K_{22})/2$ was assumed [24]. The elastic constants of the oxadiazole material are reported in paragraph 7.2.1; values of its dielectric anisotropy can be found in Ref. [16]. The results obtained for $|e_1 - e_3|$ from measurements of V_{th} are shown in Figure 7.5(b); similar results were determined from q_c. The flexoelectric difference varies approximately linearly with temperature and more than doubles across the nematic regime, assuming values from ~ 8 pCm^{-1} to ~ 20 pCm^{-1}. These values are 2–3 times higher than those reported for rod-like nematic LCs [11,24-26], in common with other bent-core materials [4,6].

7.3 Computational details

All calculations were made using the IM methodology, as described in Chapter 5. Here only the computational details related to the determination of the molecular structure of the compounds investigated here are presented.

7.3.1 Oxadiazole derivatives

All four compounds have the alkoxy $OC_{12}H_{25}$ chain as one terminal wing. At the other end of the molecule, compounds **2**–**3** are terminated by an alkoxy OC_9H_{19} chain, whereas compound **4** has a shorter alkyl chain (C_5H_{11}). Figure 7.6 shows the molecular structure of compounds **2** and **4**, as obtained from geometry optimization at the DFT/B3LYP/6-31G** level of theory [27]. The arrows indicate the dihedral angles that were allowed to rotate. For all compounds, conformational flexibility was treated within the framework of the RIS approximation [28]. Conformer geometries and energies were defined on the basis of the torsional potentials obtained from quantum mechanical calculations on representative molecular fragments. The torsional profiles were taken from the literature and/or computed by relaxed scan calculations [27] (see Appendix A). According to these data, the following choices were made:

i. Planar geometry of the central three-ring moiety was assumed, in agreement with the results of DFT calculations for 2,5-diphenyl-1,3,4-oxadiazole [29]. The torsional potential reported there for the bond between the phenyl and oxadiazole rings exhibits two minima, corresponding to coplanar configuration of the rings, separated

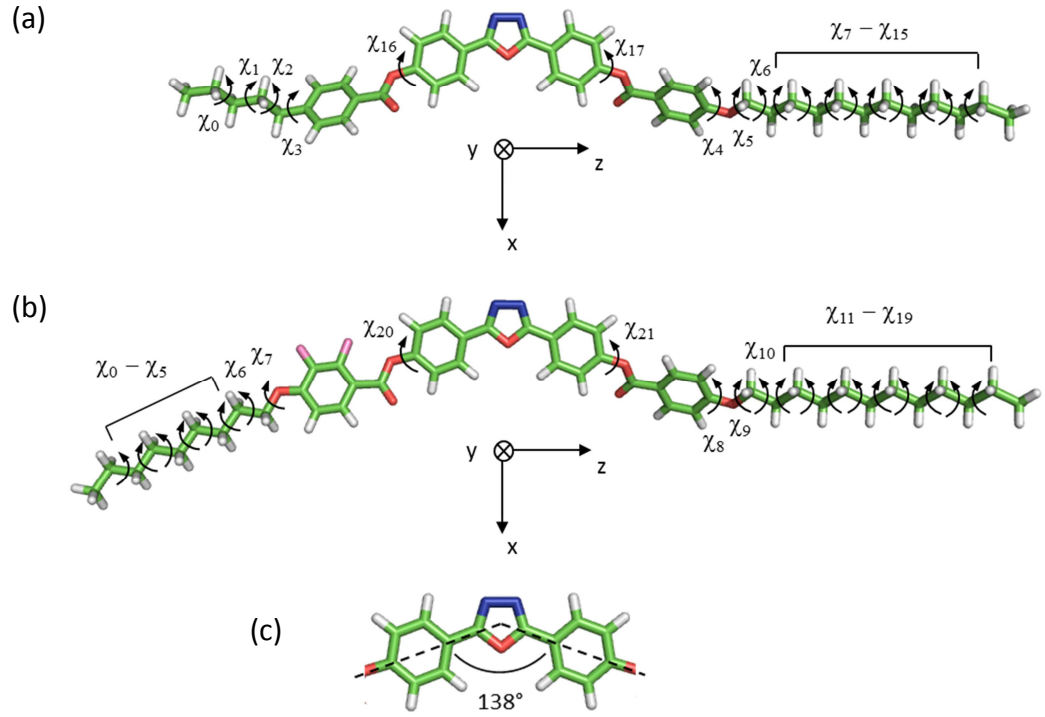

Figure 7.6 The molecular structure of the 1,3,4-oxadiazole derivatives **4** (in (a)) and **2** (in (b)) obtained from geometry optimization (DFT/B3LYP/6-31G**). The arrows show the dihedrals (χ_i) that were allowed to rotate in Monte Carlo conformational sampling. {*x*,*y*,*z*} is the molecular frame, with the *z* axis passing through the carbon atoms of the oxadiazole ring and *y* perpendicular to the plane of this ring. (c) The bend angle of the oxadiazole core is about 138°.

by a high barrier of about 30 kJ/mol, corresponding to perpendicular arrangement of the rings.

ii. In phenyl benzoate, the C_{ar}–COO bond between the aromatic carbon (C_{ar}) and the COO moiety was frozen in the planar geometry, since high barriers oppose the rotation about this bond [30,31] (see Figure A.5(i)). Choice of the geometry of C_{ar}-C_{ar}-O-CO dihedral (χ_{16}-χ_{17} in Figure 7.6(a) and χ_{21} in Figure 7.6(b)) is less obvious. As reported in the literature [30-32], and confirmed by the result of the DFT/M06-2X/6-31+G** calculations carried out here (Figure A.5(j)), the torsional profile for this angle is sensitive to the level of theory used in the calculations, and some discrepancies exist regarding the exact location of the minima and the height of the energy barriers. Despite these uncertainties, all calculations point to a wide distribution in the ranges of ±(30°–150°). For the sake of simplicity, in our calculations the C_{ar}–C_{ar}–O–CO dihedral was allowed to adopt the two values of ±90°, which correspond to the middle of the highest probability region.

iii. The benzoate group of the phenyl fluorobenzoate moiety was also assumed to be planar, with the CO group on the opposite side of the fuorine (F) atoms (as in Figure 7.6 (b)). This assumption was based on torsional potentials computed at the DFT/B3LYP/6-31+G* level of theory (Figure A.6(k)). The profile exhibits two minima, corresponding to planar configurations: the minima are non-equivalent, since the configuration having the CO group on the opposite side of the fluorine atoms is lower in energy than the other by about 3 $kJmol^{-1}$. The torsional potential for the C_{ar}–C_{ar}–O–CO dihedral in phenyl fluorobenzoate (χ_{20} in Figure 7.6(b)) has the same general form as that of phenyl benzoate, as indicated by DFT/B3LYP/6-31+G* calculations (Figure A.6(l)): therefore, also in this case the C_{ar}–C_{ar}–O–CO dihedral was allowed to adopt the values of ±90°.

iv. The CH_2–CH_2 and the O–CH_2 bonds of the alkyl and alkoxy chains were allowed to jump between the *trans* (180°), *gauche*+ (+65°) and *gauche*– (–65°) states. The *trans* state is more stable than the *gauche* state: an energy difference ΔV_{gt} = 2.2 $kJmol^{-1}$ was assumed [33,34]. The only exception is given by the O–CH_2–CH_2–CH_2 dihedral angle (χ_6 in Figure 7.6(a,b) and χ_{10} in Figure 7.6(b)), for which the *gauche* states are more stable than the *trans* state: in this case ΔV_{gt} = -2.85 $kJmol^{-1}$ was used [34]. The energy stabilization associated with the presence of adjacent *gauche*+*gauche*+ (or *gauche*–*gauche*–) pairs was accounted for by adding a correction term $\Delta V'_{g\pm g\pm}$ = – 0.75 $kJmol^{-1}$ to ΔV_{gt} [34]. Conformers with adjacent *gauche*+*gauche*− (or *gauche*−*gauche*+) pairs, which are known to bring a high energy penalty, were simply rejected on the basis of the steric cutoff used in the Monte Carlo conformational sampling (see Section 5.3).

v. Two possible equivalent states were assumed for the C_{ar}–C_{ar}–CH_2–CH_2 dihedral of alkyl chains (χ_3 in Figure 7.6(a)), corresponding to the configuration in which the C_{ar}-CH_2-CH_2 plane lies perpendicular to the phenyl ring (χ_3 =±90°), in agreement with the literature data [35] and with calculations carried out here at DFT/M06-2X/6-31+G** level of the theory (Figure A.3(d)).

vi. The C_{ar}–C_{ar}–O–CH_2 dihedral of alkoxy chains also has two minima, but in this case they are found at 0° and 180°, with the phenyl ring and the C_{ar}–O–CH_2 group lying in the same plane. These two states are equivalent if the aromatic group is a benzene [35], whereas in the presence of fluoro substituents the conformation

having the O–CH_2 bond on the opposite side of the fluorine atoms is found to be more stable (by about 3 $kJmol^{-1}$ at the B3LYP/6-31G** level and 7 $kJmol^{-1}$ at the B3LYP/6-31+G* level, see Figure A.6(m)), in agreement with calculations reported in the literature [36,37].

7.3.2 Thiadiazole derivative

The molecular structure shown in Figure 7.7 was obtained by geometry optimization at the DFT/B3LYP/6-31G* level of theory. For simplicity, the ester group at the end of the alkoxy chain was replaced by two methylene groups in the calculations. We have found that the bend angle in the central core is 164°, in agreement with previous calculations for similar systems at a different level of theory [38].

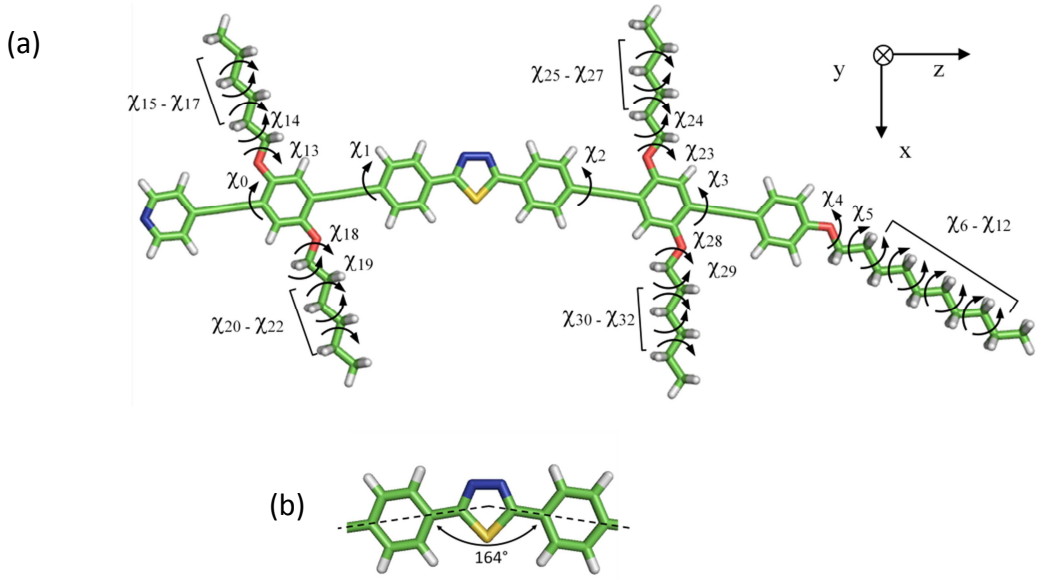

Figure 7.7 (a) The molecular structure of the 1,3,4-thiadiazole derivative obtained from geometry optimization (DFT/B3LYP/6-31G*). The arrows show the dihedrals (χ_i) that were allowed to rotate in Monte Carlo conformational sampling. {*x*,*y*,*z*} is the molecular frame, with the *z* axis passing through the carbon atoms of the thiadiazole ring and *y* perpendicular to the plane of this ring. (b) The bend angle of the thiadiazole core is about 164°.

In generating molecular conformations within Monte Carlo sampling, the following choices have been made:

i. Planar geometry was assumed for the central three-ring core, in agreement with the results of DFT calculations for 2,5-diphenyl-1,3,4-thiadiazole [39].

ii. Free rotation around the C_{ar}–C_{sp^1} bonds was assumed : the dihedral angles χ_0–χ_3 in Figure 7.7 could take any value with the same probability. Indeed, according to experimental and theoretical studies of diphenylacetylene [40], the torsional profile for the C_{ar}–C_{sp^1} bond is rather flat, with the absolute minima corresponding to coplanar phenyl rings and a low energy barrier, not higher than 2.5 kJ mol^{-1}, for the perpendicular configuration. For comparison we have also run calculations of the elastic constants assuming a planar core geometry, obtained by freezing all rotations around C_{ar}–C_{sp^1} bonds. Hereafter, this calculation will be referred to as the "planar-core model".

iii. For the dihedrals in the terminal and lateral alkoxy chains the same choices were made as for the oxadiazole compounds (see points iv and vi in Section 7.3.1), with the only difference that the dihedrals corresponding to the C_{ar}–O bonds were kept fixed in the configuration shown in Figure 7.7, with the O–CH_2 bond pointing away from the phenylethynyl group for reasons of steric hindrance.

7.4 Results and Discussion

7.4.1 Elastic constants

Figure 7.8 (a) shows the results of calculations of the elastic constants of the oxadiazole compound **4**, as a function of the molecular order parameter $S=S_{zz}$ relative to the *z* axis defined in Figure 7.6(a) (see Eq. 1.9). For comparison the experimental data are also included in the plot: here *S* corresponds to the macroscopic order parameter obtained from birefringence measurements (see Eq. 1.20) [13,14]. In agreement with experimental trend, and in contrast to the usual behaviour of rod-like LCs, $K_{11} > K_{33} > K_{22}$ is predicted. Both K_{11} and K_{33} are slightly higher (by 2-3 pN) than the experimental values, but strict quantitative agreement is probably beyond the present capability. Our calculations have shown that the elastic constants are very sensitive to the molecular shape and flexibility, therefore the predictions are affected by a certain error related to unavoidable uncertainties in the geometric parameters.

The trend of the calculated elastic constants as a function of the order parameter is also in agreement with experiment: K_{11} and K_{22} increase with increasing order, whereas K_{33} exhibits only a weak dependence on the order parameter, first increasing and then

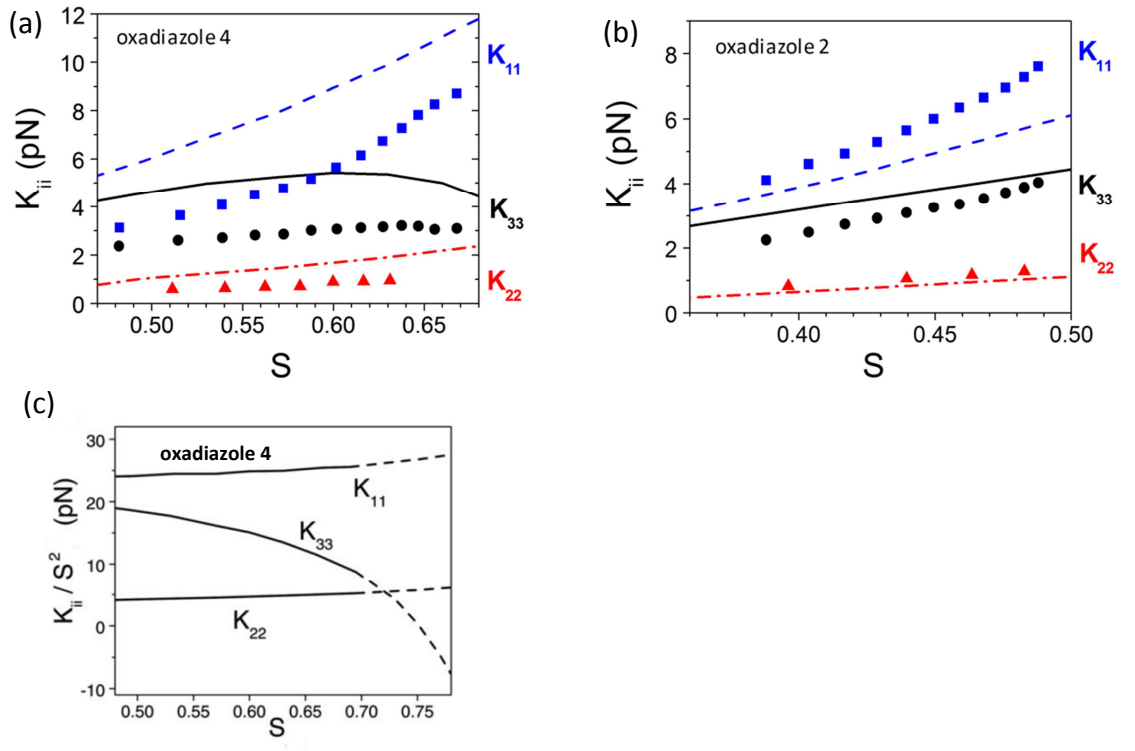

Figure 7.8 The elastic constants of the oxadiazole compounds **4** (in (a)) and **2** (in (b)), as a function of the order parameter *S*. Symbols represent the experimental data and lines the results of the calculations: K_{11} (squares and dashed line), K_{22} (triangles and dash-dotted line) and K_{33} (circles and solid line). In calculations *S* is the molecular order parameter for the molecular *z* axis defined in Figure 7.6; in experiments *S* is the macrosocopic order parameter obtained from birefringence [13,14]. (c) Ratio of elastic constants (K_{ii}) to the squared order parameter *S* for the oxadiazole compound **4**, as obtained from calculations. Dashed lines are used for points beyond the experimental nematic range.

decreasing at high ordering. The latter behaviour is not accounted for by simple theories of elasticity developed for rod-like LCs, which predict $K_{ii} \propto S^2$ (see Section 2.3.1). The theoretical expressions of the elastic constants here used (Eq. 5.13) contain an implicit dependence on all orientational order parameters, without restriction to quadratic terms in *S*. Figure 7.8(c) shows the K_{ii}/S^2 ratios calculated for compound **4**: results obtained for values of the order parameter inside the experimental nematic range are evidenced by solid lines. For illustrative purpose, values predicted beyond this range are also included (dashed lines): they represent the elastic constants of a hypothetical nematic phase extending to very high ordering. One can notice that the splay and twist elastic constants are not strictly proportional to S^2, but deviations are relatively small. On the contrary, a strong dependence on the order parameter is predicted for the ratio K_{33}/S^2, which would diverge to negative values at very high ordering. Negative K_{33} values

would be incompatible with the existence of a uniform nematic phase because they imply spontaneous bending of the director [41]. Calculations of the elastic constants were also carried out for compounds **2** and **3**. Both differ from compound **4** for the replacement of the pentyl with a longer nonyloxy chain. In compound **2** there are also two additional F atoms in the phenyl ring attached to the nonyloxy chain. In the framework of the molecular model used here, the F atoms are expected to affect the elastic constants if they can induce a change of the conformational preferences, and thus a change of the average molecular shape. Quantum chemical calculations show that the main effect of the F atoms is that of stabilizing conformations having both the CO group and the O–CH_2 bond on the opposite side of the F atoms (see Section 7.3.1). We have found that neither this variation, nor those deriving from change of the lateral chain, significantly affect the average molecular shape: the plots of the elastic constants as a function of the order parameter calculated for compounds **2** and **3** are very similar to each other and also not very different from that predicted for compound **4** (see Figure 7.8). The small influence of changes in the lateral arms on the elastic constants is in line with the experimental data.

Figure 7.9(a) shows the experimental and calculated elastic constants for the thiadiazole derivative as a function of the order parameter S. In calculations $S=S_{zz}$ (see Eq. 1.9), with the z axis defined in Figure 7.7; in the experiments S corresponds to the macroscopic order parameter obtained from the birefringence (see Eq. 1.20) [15].

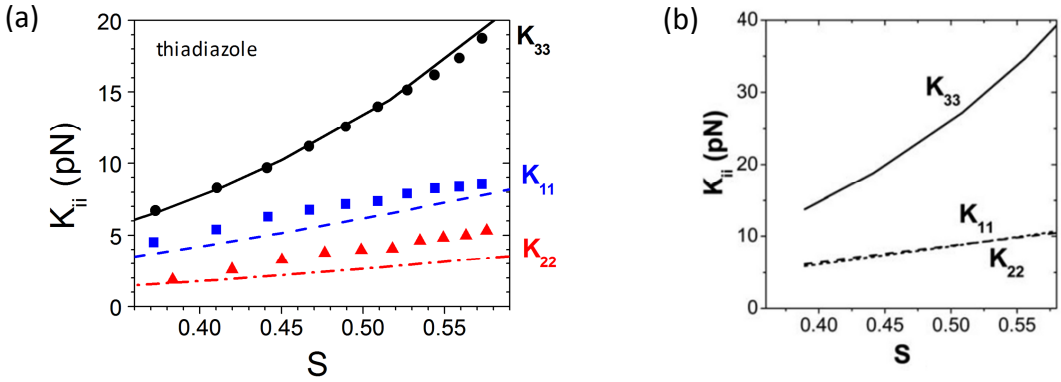

Figure 7.9 (a) The experimental (symbols) and calculated (lines) elastic constants of the thiadiazole material, as a function of the order parameter: K_{11} (squares and dashed line), K_{22} (triangles and dash-dotted line) and K_{33} (circles and solid line). In calculations S is the molecular order parameter S_{zz} for the molecular z axis defined in Figure 7.7; in experiments S is the macroscopic order parameter obtained from birefringence [15]. (b) Elastic constants calculated for the "planar-core model": K_{11} (short dashed line), K_{22} (dashed line) and K_{33} (solid line).

The theoretical predictions are in excellent agreement with the experimental values. Calculations allow us to shed light on the origin of the different bend elasticity of the the thiadiazole and oxadiazole derivatives. Given the nature of the model used, the diversity in the elastic constants must originate from differences in the molecular structure: these are the bend angle in the molecular core, which increases from about 138° to about 164° on going from the oxadiazole to the thiadiazole system, and the presence of the lateral chains in the latter. Our simulations point to the importance of the bend angle; when the angle is sufficiently wide, the behaviour of rod-like LCs is recovered. The sensitivity of K_{33} to the bend angle, especially in the range around 150°, has been also evidenced by calculations we have performed for model systems as a function of the bend angle. Some authors have suggested that the lateral chains could be responsible for the rod-like elasticity of the thiadiazole derivative [42], but this is not confirmed by our calculations. The lateral chains, which may be important to stabilize the nematic phase [43] do not seem to dramatically affect the elastic properties. These chains are highly flexible, so the average molecular shape is elongated, similar to that of rod-like compounds, as shown in Figure 7.10, which displays some configurations randomly extracted from the Monte Carlo trajectories.

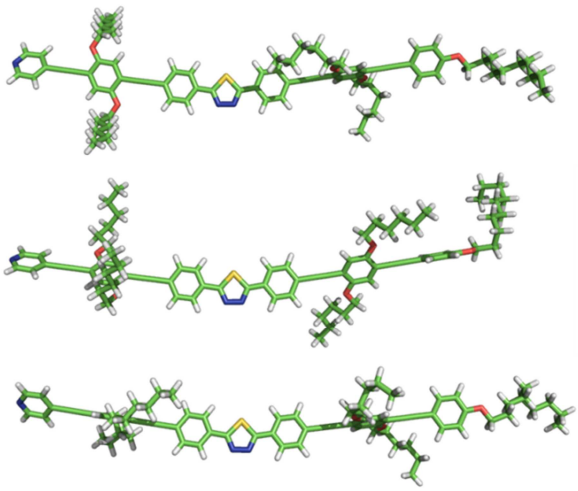

Figure 7.10 Some configurations of the thiadiazole derivative extracted from a Monte Carlo trajectory in the conformational space.

To check whether the flexibility within the core affects the elastic properties, we have also run calculations keeping all rings on the same plane (“planar core model”). The results given in Figure 7.9(b) show that the elastic constants predicted in this way are

very high, especially K_{33} and K_{22}, which are roughly twice as big as the experimental values.

7.4.2 Flexoelectric coefficients

Figure 7.11 (a) shows the flexoelectric difference $(e_1 - e_3)$ calculated for the oxadiazole compound **4** as a function of the order parameter. The experimental data are also included for comparison: since measurements did not allow to determine the sign of $(e_1 - e_3)$, negative values are assumed, as predicted by our calculations. The theoretical results are in very good agreement with the experimental findings.

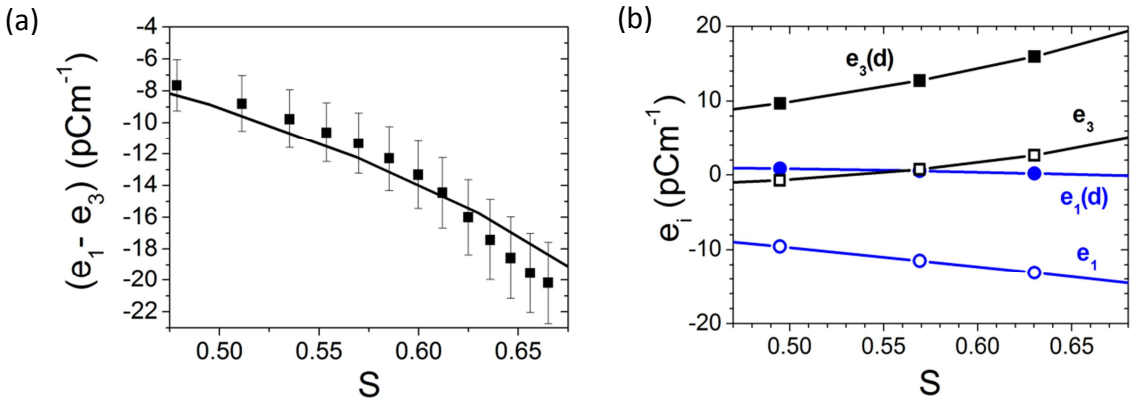

Figure 7.11 (a) The experimental (symbol) and calculated (line) values of (e_1-e_3) for the oxadiazole compound **4**, as a function of order parameter *S*. Following calculations, the experimental values of (e_1-e_3) are assumed to take a negative value. In calculations *S* is the molecular order parameter for the molecular *z* axis defined in Figure 7.6; in experiments *S* is the macrosocopic order parameter obtained from birefringence [13,14]. (b) The calculated flexoelectric coefficients e_i, as a function of *S*: splay (open circles), dipole contribution to the splay (filled circles), bend (open squares), dipole contribution to the bend (filled squares).

Calculations allowed us to determine not only $(e_1 - e_3)$, but also the individual splay (e_1) and bend (e_3) flexoelectric coefficients. As described in Chapter 5, each of them has both a dipolar (*d*) and a quadrupolar (*q*) contribution which result respectively from the molecular electric dipole and quadrupole moments. These contributions can be distinguished with our methodology, which can be useful to connect the flexoelectric behaviour to the molecular structure, also in the light of the models presented in Chapter 2. According to the quantum mechanical calculations performed by us, the oxadiazole

compound **4** has a transverse dipole moment $\mu_\perp$ which, depending on the molecular conformation, varies from ~3.5 D to ~4 D, and which points towards the centre of curvature of the banana-like molecular shape (Figure 7.12). On the contrary, the longitudinal electric dipole $\mu_\parallel$ is very small. The results obtained for the individual flexoelectric coefficients and their dipolar contribution are shown in Figure 7.11(b). The dipolar contribution to the bend flexoelectric coefficient, $e_3(d)$, is large and positive, as expected for a banana-shaped molecule with an inward pointing transverse dipole [44]. On the contrary, $e_1(d)$ is very small, consistent with the small value of $\mu_\parallel$; in any case, the banana-like molecular shape would not allow an effective coupling of a longitudinal dipole to a splay deformation. The quadrupole contribution, which is identical for e_1 and e_3 (see Chapter 5) is comparable in magnitude to the dipole contribution to e_3, but opposite in sign. This leads to a small e_3, lower in magnitude than e_1, apparently in contrast to what one might expect for bent-shaped mesogens. The flexoelectric difference $(e_1 - e_3)$ depends only on the dipolar contributions: $(e_1 - e_3) \sim -e_3(d)$ is found, since $e_1(d) \sim 0$.

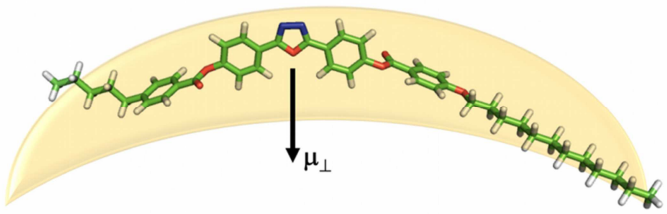

Figure 7.12 Cartoon representing the molecular features of the oxadiazole compound **4** essential to rationalize its flexoelectric behavior: a banana-like shape coupled to a transverse dipole moment ($\mu_\perp$).

It is interesting to consider how the flexolectric coefficients of the oxadiazole compound investigated here compare with the values experimentally determined for other bent-shaped systems. For a 4-cyanoresorcinol bisbenzoate bent-core mesogen, which also has an inward pointing dipole, qualitatively similar results were reported [4]: a negative $(e_1 - e_3)$ which increases in magnitude from ~10 pCm^{-1} to ~17 pCm^{-1} with decreasing temperature. Although the magnitude $|e_1 - e_3|$ is comparable to the values for the

oxadiazole compound **4**, the temperature dependence is larger. In Ref. [12], a value of $|e_3|$ ~ 4 pCm^{-1} (T-T_{NI} = –5K) is reported for another 4-cyanoresorcinol derivate, which is similar in magnitude to $|e_3|$ calculated here for the oxadiazole compound **4**. The higher value, $|e_3|$ ~16 pCm^{-1}, found in Ref. [11] for a 4-chlororesorcinol derivative, is not necessarily in contradiction with what found here and in Ref. [12]. The C–Cl group has a lower dipole moment than the C–CN group: as a consequence a smaller dipolar contribution to e_3 is expected. High values of $|e_1 - e_3|$, even larger than 20 pCm^{-1} at low reduced temperatures, have been reported for odd mesogenic dimers, which have an average bent shape [45,46]. The behaviour of both $(e_1 - e_3)$ and of e_1 and e_3 individually [47] is similar to that found here for bent-core mesogens, provided all signs are reversed. This is explained by a change of sign of the transverse dipole, which points outwards in the case of dimers with terminal cyano or fluorine groups.

7.5 Conclusions

We have characterized the elastic and flexoelectric properties various bent-core nematics by experiments and computation, focusing on the relationship between these properties and the chemical structure of the mesogens. Two kinds of materials were examined: a series of oxadiazole derivatives and a thiadiazole compound.

For what regards the elastic properties, $K_{11} > K_{33} > K_{22}$ was obtained for all oxadiazole compounds, from both experiments and calculations, with low values of the bend elastic constant K_{33}. This behaviour is in contrast to that exhibited by conventional rod-like LCs and in common with other bent-core materials studied to date. Changes in the length of the terminal chains and fluoro-substitution in the outer part of the aromatic core were found to have little influence on the values of the elastic constants. Completely different results were obtained for the thiadiazole material: $K_{33} > K_{11}$ was found in both experiments and calculations, with high values of the bend elastic constant, as would be expected for a rod-like mesogen of relatively big size. Calculations showed that the origin of this difference can be attributed to the value of the core bend angle, which increases from about 138° to 164° on going from the oxadiazole to the thiadiazole systems. These results indicate that the bend angle is the

main molecular parameter governing the elastic behaviour of BCNs, especially in the case of the bend elastic constant K_{33}, which appears to be extremely sensitive to changes in the molecular curvature. It would be interesting to study other bent-core materials with intermediate bend angles to obtain a threshold where K_{33} becomes greater than K_{11}. The theoretical predictions are in very good quantitative agreement with experiments (within ~2 pN), proving that the computational methodology employed by us is sufficiently sensitive to account for the effects of the chemical structure of the elastic properties.

For what regards the flexolectric properties, the difference $|e_1 - e_3|$ between the splay e_1 and bend e_3 flexoelectric coefficients was experimentally determined for one of the oxadiazole compound. Values were obtained which are 2–3 times higher than those typical of conventional rod-like nematic LCs. The theoretical predictions are in very good agreement (within 1-2 pCm^{-1}) with the experimental results. Calculations gave access also to the individual flexoelectric coefficients and to their dipolar and quadrupolar contribution, providing insight into the origin of the experimental behaviour and allowing us to identify some general features of flexoelectricity in bent-core compounds. After more than fourty years from its discovery, the molecular determinants of the flexoelectric effect in liquid crystals remain poorly understood, because of the experimental difficulties and the limits of simple models. The combination of accurate measurements and theoretical predictions presented here appears very promising for developing a molecular-based knowlegde of flexolectricity, which is very important for exploitation of this phenomenon.

7.6 References

1 P. Sathyanarayana, M. Mathews, Q. Li, V. S. S. Sastry, B. Kundu, K. V. Le, H. Takezoe and S. Dhara, *Phys. Rev. E*, 2010, **81**, 010702.

2 P. Tadapatri, U. S. Hiremath, C. V. Yelamaggad and K. S. Krishnamurthy, *J. Phys. Chem. B*, 2010, **114**, 1745 –1750.

3 M. Majumdar, P. Salamon, A. Jákli, J. Gleeson and S. Sprunt, *Phys. Rev.* E, 2011, **83**, 031701.

4 P. S. Salter, C. Tschierske, S. J. Elston and E. P. Raynes, Phys. Rev. E, 2011, **84**, 031708.

5 N. Avci, V. Borshch, D. D. Sarkar, R. Deb, G. Venkatesh, T. Turiv, S. V. Shiyanovskii, N. V. S. Rao and O. D. Lavrentovich, *Soft Matter*, 2013, **9**, 1066 –1075.

6 R. Balachandran, V. P. Panov, J. K. Vij, A. Lehmann and C. Tschierske, *Phys. Rev. E*, 2013, **88**, 032503.

7 A. Chakraborty, M. K. Das, B. Das, A. Lehmann and C. Tschierske, *Soft Matter*, 2013, **9**, 4273 –4283.

8 A. Jákli, *Liq. Cryst. Rev.*, 2013, **1**, 65 –82.

9 (a) F. Castles, S. M. Morris and H. J. Coles, *AIP Advances*, 2011, **1**, 032120. (b) P. Palffy-Muhoray, *AIP Advances*, 2013, **3**, 019101. (c) F. Castles, S. M. Morris and H. J. Coles, *AIP Advances*, 2013, **3**, 019102.

10 J. Harden, B. Mbanga, N. Éber, K. Fodor-Csorba, S. Sprunt, J. T. Gleeson, and A. Jákli, *Phys. Rev. Lett.*, 2006, **97**, 157802.

11 K. V. Le, F. Araoka, K. Fodor-Csorba, K. Ishikawa and H. Takezoe, *Liq. Cryst.* 2009, **36**, 1119-1124.

12 P. Kumar, Y. G. Marinov, H. P. Hinov, U. S. Hiremath, C. V. Yelamaggad, K. S. Krishnamurthy and A. G. Petrov, *J. Phys. Chem. B*, 2009, **113**, 9168-9174.

13 S. Kaur, J. Addis, C. Greco, A. Ferrarini, V. Görtz, J.W. Goodby and H.F. Gleeson., *Phys. Rev. E*, 2012, **86**, 041703.

14 S. Kaur, H. Liu, J. Addis, C. Greco, A. Ferrarini, V. Görtz, J.W. Goodby and H.F. Gleeson, *J. Mater.Chem. C*, 2013, **1**, 6667-6676.

15 S. Kaur, L. Tian, H. Liu, C. Greco, A. Ferrarini, J. Seltmann, M. Lehmann and H.F. Gleeson, *J. Mater. Chem. C*, 2013, **1**, 2416-2425.

16 S. Kaur, V. P. Panov, C. Greco, A. Ferrarini, V. Görtz, J.W. Goodby and H. F. Gleeson, *Appl. Phys. Lett.*, 2014, 105, 223505.

17 R. H. Chen, Liquid Crystal Displays: Fundamental Physics and Technology, Wiley, Hobocken, NJ, 2011.

18 L. M. Blinov and V. G. Chigrinov, *Electrooptic Effects in Liquid Crystal Materials*, Springer-Verlag, New York, 1994.

19 K. Ikeda, H. Okada, H. Onnagawa and S. Sugimor, *J. Appl. Phys.*, 1999, **86**, 5413-5416.

20 Á. Buka, T. Tóth-Katona, N. Éber, A. Krekhov and W. Pesch, in *Flexoelectricity in Liquid Crystals: Theory, Experiments and Applications*, ed. Á. Buka and N. Éber, Imperial College Press, London, 2013, ch. 4.

21 Yu. P. Bobylev and S. A. Pikin, *Sov. Phys. JETP*, 1977, **45**, 195-198.

22 A. Krekhov, W. Pesch, N. Éber, T. Tóth-Katona and Á. Buka, *Phys. Rev. E*, 2008, 77, 021705.

23 A. Krekhov, W. Pesch and Á. Buka, *Phys. Rev. E*, 2011, **83**, 051706 .

24 P. Salamon, N. Éber, A. Krekhov and Á. Buka, *Phys. Rev. E.*, 2013, **87**, 032505.

25 N. Éber, in *Flexoelectricity in Liquid Crystals: Theory, Experiments and Applications*, ed. Á. Buka and N. Éber, Imperial College Press, London, 2013, Appendix A.

26 F. Castles, S. C. Green, D. J. Gardiner, S. M. Morris and H. J. Coles, *AIP Adv.*, 2012, **2**, 022137.

27 Gaussian 09 (Revision B.01), M. J. Frisch et al., Gaussian, Inc., Wallingford CT, 2010.

28 P. W. Flory, *Statistical Mechanics of Chain Molecules*, Wiley-Interscience, New York, 1969.

29 J. P. Laguno, Ph.D Thesis, Durham University, 2007.

30 R. Wrzalik, K. Merkel and A. Kocot, *J. Mol. Model.*, 2003, **9**, 248– 258.

31 G. Cinacchi and G. Prampolini, *J. Phys. Chem. A*, 2005, **109**, 6290 –6293.

32 S. Kawauchi, S.-W. Choi, K. Fukuda, K. Kishikawa, J. Watanabe and H. Takezoe, *Chem. Lett.*, 2007, **36**, 750 –751.

33 J. B. Klauda, R. W. Pastor and B. R. Brooks, *J. Phys. Chem. B*, 2005, **109**, 15684-15686.

34 M. Cestari, PhD Thesis, University of Padova, 2009.

35 G. Cinacchi and G. Prampolini, *J. Phys. Chem. A*, 2003, **107**, 5228-5232.

36 V. P. Novikov, L.V. Vilkov and H. Oberhammer, *J. Phys. Chem. A*, 2003, **107**, 908-913.

37 T. Isozaki, K. Sakeda, T. Suzuki, T. Ichimura, K. Tsuji and K. Shibuya, *Chem. Phys. Lett.*, 2005, **409**, 93–97.

38 J. Seltmann, A. Marini, B. Mennucci, S. Dey, S. Kumar and M. Lehmann, *Chem. Mater.*, 2011, **23**, 2630-2636.

39 J. M. Granadino-Roldán, A. Garzón, G. García, T. Peña-Ruiz, M. Paz Fernández-Liencres, A. Navarro and M. Fernández-Gómez, *J. Chem. Phys.*, 2009, **130**, 234907.

40 D. Xu and A. L. Coosky, *J. Mol. Struct.*, 2007, **815**, 119-125.

41 J. L. Ericksen, *Phys. Fluids*, 1966, **9**, 1205– 1207.

42 P. Salamon, N. Éber, J. Seltmann, M. Lehmann, J. T. Gleeson, S. Sprunt and A. Jákli, *Phys. Rev. E*, 2012, **85**, 061704.

43 Y.-K. Kim, M. Majumdar, B. I. Senyuk, L. Tortora, J. Seltmann, M. Lehmann, A. Jákli, J. T. Gleeson, O. D. Lavrentovich and S. Sprunt, *Soft Matter*, 2012, **8**, 8880-8890.

44 R. B. Meyer, *Phys. Rev. Lett.*, 1969, **22**, 918-921.

45 K. L. Atkinson, S. M. Morris, F. Castles, M. M. Qasim, D. J. Gardiner and H. J. Coles, *Phys. Rev. E*, 2012, **85**, 012701.

46 K. L. Atkinson, S. M. Morris, M. M. Qasim, F. Castles, D. J. Gardiner, P. J. W. Hands, S. S. Choi, W.-S. Kim and H. J. Coles, *Phys. Chem. Chem. Phys.*, 2012, **14**, 16377- 16385.

47 M. Cestari, E. Frezza, A. Ferrarini and G. R. Luckhurst, *J. Mater. Chem.*, 2011, **21**, 12303- 12308.

Chapter 8

Elasticity in liquid crystal dimers: coupling of bent shape and flexibility

8.1 Introduction

Liquid crystalline dimers are molecules containing two terminal mesogenic units joined by a flexible spacer, usually an alkyl chain with functional groups (linkers) at its ends (see Chapter 2) [1]. According to number of atoms in the spacer these systems have been classified as even and odd dimers. The length and parity of the spacer and the nature of the linking group are known to strongly affect the properties of the nematic to isotropic (N-I) phase transition (transition temperatures, entropy of transition, order parameters at the transition), with a characteristic odd-even effect. This happens because the aforementioned geometric features affect the relative orientation of the terminal mesogenic units, and thus the molecular shape. On average even dimers have a linear shape, and are thus better accommodated in the nematic environment than odd dimers [2,3].

More recently it has been recognized that the molecular structure of dimers has a significant influence also on other properties. These include the elastic and flexoelectric properties of their N phase, which appear promising for the development of new display applications based on the flexoelectroptic effect (see Chapter 2) [4] . Indeed, compared to conventional rod-like nematics, liquid crystal dimers have been found to exhibit an enhanced flexoelectroptical response [5]. Here the figure of merit is the flexoelastic ratio, $\bar{e}/\bar{K}$, where $\bar{e}=(e_1-e_3)/2$ is the difference between the splay (e_1) and the bend (e_3) flexoelectric coefficients, and $\bar{K}=(K_{11}+K_{33})/2$ is the average value of the splay

(K_{11}) and bend (K_{33}) elastic constants. Even in this case, differences have been evidenced between odd and even dimers, the first exhibiting higher $\bar{e}/\bar{K}$ values than the latter. In a recent computational investigation of the flexoelectric and elastic properties of some ether-linked dimers [6], the elastic constant K_{33} was predicted to be much smaller in odd dimers than in even dimers; this difference was shown to be at the origin of the higher $\bar{e}/\bar{K}$ values of the odd-membered compounds. The predictions were subsequently confirmed by experiments [7].

The identification of a twist-bend nematic organization (N_{TB}) [8] in the phase diagram of methylene-linked dimers [9-21], together with the observation that this phase is less common in ether-linked dimers [10,18,22,23], has aroused new questions about the relationship between the molecular structure and the phase behaviour in these systems.

In this chapter we present an investigation of the effect of changes in the molecular structure on the elastic properties of some cyanobiphenyl dimers. The work has been carried out in collaboration with Merck Chemicals Ltd. Results for three representative compounds are reported (Figure 8.1): a methylene-linked dimer (CB9CB), an ester-linked dimer (OCO), and a compound with a *cis*-double bond in the middle of the spacer (CIS_4-4). The predicted elastic properties will be rationalized in the light of the molecular structure of the dimers, taking into full account the effect of the conformational flexibility of the spacer. Some considerations will also be drawn about

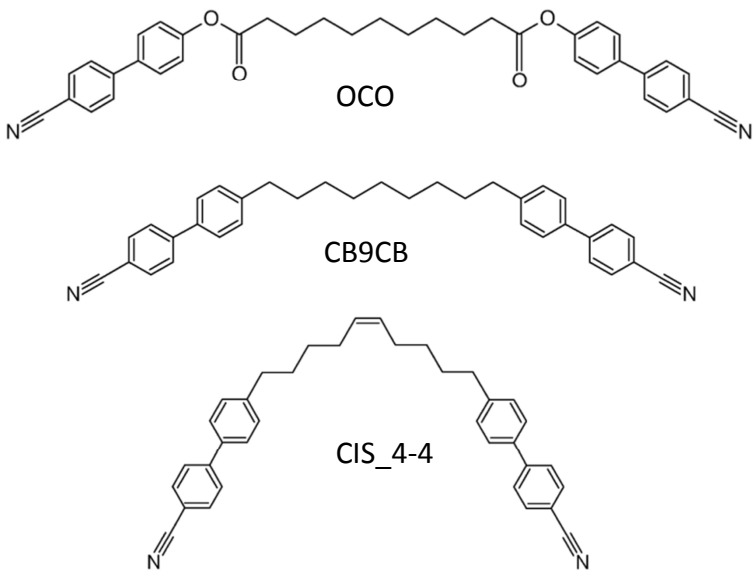

Figure 8.1. Chemical structure of the dimers here investigated. The acronyms here used for each compound are also indicated.

the relation between the molecular structure of the dimers and their propensity to form a N_{TB} phase. In Section 8.2 the computational details will be presented and the results will be reported and discussed in Section 8.3.

8.2 Computational details

Elastic constants were computed according to the IM methodology, as described in Chapter 5. In the following we focus on the modelling aspects specifically related to the systems under investigation, in particular on the determination of the molecular geometry and the conformational distribution. Because of role played by the flexible spacer in determining the average molecular shape, an accurate description of the molecular structure is especially important for liquid crystal dimers, even more than for bent-core systems.

8.2.1 Molecular geometry and torsional potentials

Figure 8.2 shows the molecular structure of the compounds investigated, as obtained from geometry optimization at the DFT/B3LYP/6-31G** level of theory [24]. The bond angle connecting the mesogenic unit to the spacer is found to be $C_{ar}\widehat{C}C \sim 113°$ for a methylene link and $C_{ar}\widehat{O}C \sim 123°$ for an ester link (C_{ar} is the aromatic carbon). The conformation of compound CIS_4-4 shown in Figure 8.2(c) has an elongated shape, at variance with what one may have guessed on the basis of the structural formula shown in Figure 8.1. This is an interesting result, but a complete conformational analysis has to be carried out to determine the average molecular shape.

The arrows in Figure 8.2 indicate the dihedral angles that were allowed to rotate. The torsional potential for the biphenyl twist angle (χ_0 and its analogue in the other mesogenic unit) was deduced form the literature [25]. It is characterized by four equivalent minima located at ~ ±35° and ~ ±145°, and energy barriers of about 8 $kJmol^{-1}$ for planar and perpendicular arrangement of the rings. For all other dihedrals, torsional potentials were obtained by DFT calculations on representative molecular fragments, and are reported in Appendix A. In the following we summarize their main features.

(a) CB9CB:

Three kinds of dihedral angles can be distinguished: χ_1 and χ_{10}, defined by the sequence C_{ar}–C_{ar}–C–C; χ_2 and χ_9, defined by the sequence C_{ar}–C–C–C, and finally the chain dihedrals χ_i (i = 3-8), defined by C–C–C–C. Torsional profiles for these angles were calculated at the M06-2X/6-31+G** level, using as model compounds propylbenzene (χ_1), butylbenzene (χ_2) and hexane (χ_i). The M06-2X functional [26] was chosen to take into account the effect of dispersion interactions on the energy profile: these are expected to be especially important for χ_2, since rotation about this bond controls the relative distance between the aromatic rings and the alkyl chain. The torsional potential for the χ_1 dihedral (Figure A.3(d)) exhibits two equivalent minima at ± 90°, corresponding to perpendicular arrangement of the benzene ring with respect to the C_{ar}–C–C plane; barriers of about 5 kJmol^{-1} are found for nearly-planar configurations. These results are in agreement with what reported in the literature for ethylbenzene at the DFT/B3LYP/6-311G(2d,p) level of theory [27]. Both χ_2 and χ_i exhibit minima for the *trans* (180°), *gauche*+ (~ +60°) and *gauche*– (~ –60°) states, but the stability order of the *trans* and *gauche* states is reversed for the two kinds of angles. For the χ_i dihedrals, the *trans* conformation is more stable than the *gauche* one, with an energy difference $\Delta V_{gt}^{(i)}$ ~ 2.2 kJmol^{-1} (Figure A.1). This value is similar to that predicted by high-level *ab initio* calculations [28], and slightly lower than the value of ~3.5 kJmol^{-1} obtained by DFT/B3LYP calculations with various basis sets [29]. For the χ_2 dihedral the value $\Delta V_{gt}^{(2)}$ ~ –1.1 kJmol^{-1} was found (Figure A.3(e)), as reported in the literature [30] and in line with indications provided by some experiments [31]. This energy difference is very small, and probably within the error of current methods [32]: therefore this result mainly indicates that for the χ_2 dihedral the difference in the population of *trans* and *gauche* states is smaller than for a "normal" C–C–C–C dihedral. Notice that reversal of the *gauche-trans* stability order for χ_2 is not predicted by B3LYP [30]: using this functional and various basis sets, $\Delta V_{gt}^{(2)}$ ~ 2.5 kJmol^{-1} was reported, which is lower than the value $\Delta V_{gt}^{(i)}$ ~ 3.5 kJmol^{-1} obtained with the same functional for the χ_i dihedrals [29], but still in favour of the *trans* conformation. On the one hand, this indicates that dispersion effects might indeed be important to stabilize

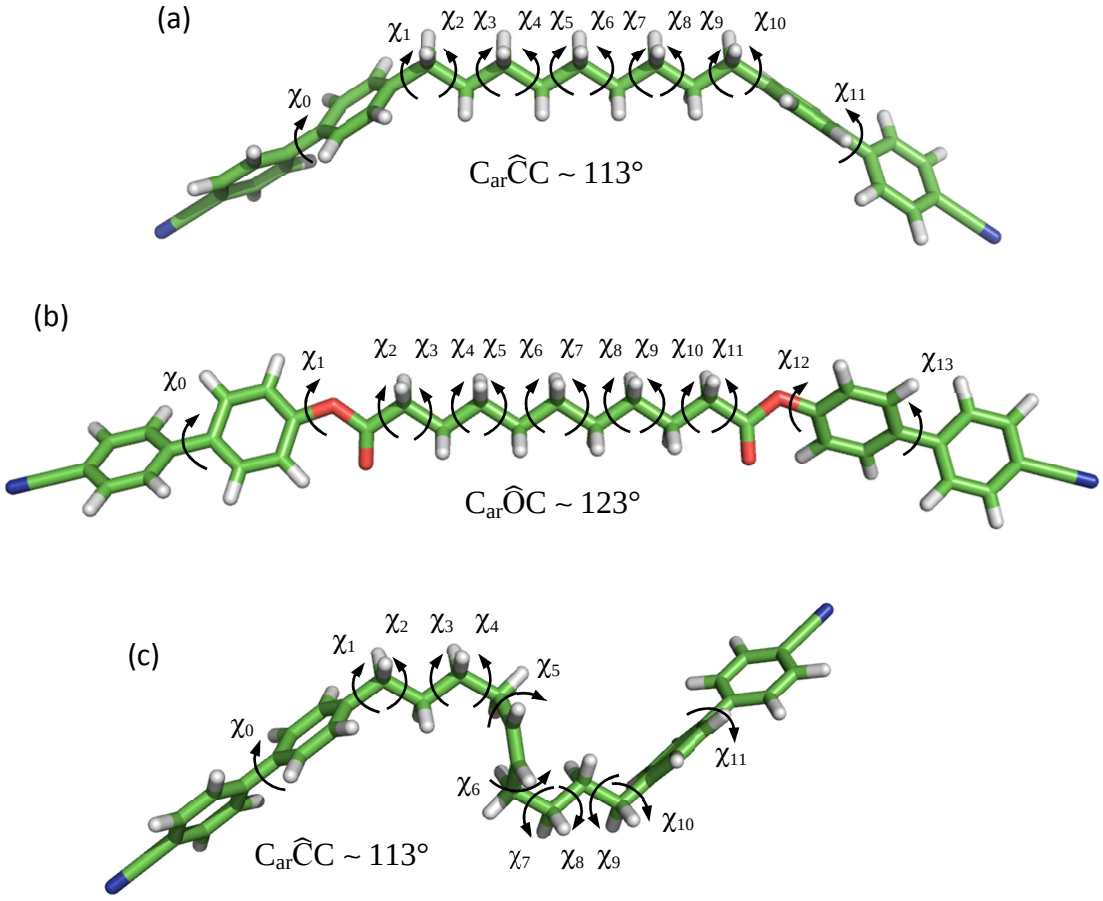

Figure 8.2. Optimized geometry (DFT/B3LYP/6-31G**) of: (a) the all-*trans* conformation of CB9CB; (b) the all-*trans* conformation OCO; (c) the conformation of CIS_4-4 having χ_2, χ_3, χ_8, χ_9 in the *trans* state, χ_5,χ_6 in the *skew*+ state and χ_4, χ_7 in the *gauche*− state. The arrows indicate the dihedral angles that were allowed to rotate in Monte Carlo conformational sampling. Also shown is the value of the bond angle connecting the mesogenic unit to the spacer.

gauche conformations of χ_2; on the other hand it highlights that the conformational preferences of this dihedral angle are quite subtle.

(b) OCO:

For the χ_j dihedral angles of the alkyl chain (j=4-9) the same torsional potentials were used as those adopted for the C–C–C–C dihedrals of CB9CB. According to the literature [33,34], the C_{ar}–O–C(=O)–C dihedral angle exhibit two minima, corresponding to the *trans* and *cis* states: the latter is higher in energy than the first by ~ 30 kJmol^{-1} and is thus negligibly populated at reasonable temperatures. Therefore in our calculations, this dihedral angle was kept frozen in the *trans* conformation. The

torsional profile for the C_{ar}–C_{ar}–O–CO dihedral (χ_1), calculated on the model compound phenyl propanoate at the DFT/B3LYP/6-31G** level, was found to be relatively flat (Figure A.4(f)): the absolute minima, located at ~ ±45° and ~ ±135°, are separated by energy barriers of less than 2 kJmol^{-1}. Torsional potentials for the O–C(=O)–C–C (χ_2) and C(=O)–C–C–C (χ_3) dihedral angles were computed at the DFT/M06-2X/6-31+G** level, using phenyl butanoate and phenyl pentanoate as model compounds, respectively. The dihedral angle χ_2 exhibits an absolute minimum for the *trans* state (χ_2=180°) and very shallow relative minima for *gauche* states (χ_2 ~ ±70°), with small barriers between them (Figure A.4(g)): the complete profile is analogous to that reported for the corresponding dihedral of methyl propanoate at the MP2/aug-cc-pvDZ [33] and DFT/B3LYP/6-311++G** [34] levels. Well-defined *trans* and *gauche* minima were found for χ_3, with the *gauche* states more stable than the *trans* state by about −0.8 kJmol^{-1} (Figure A.4(h)). This preference for *gauche* states was also revealed by MP2/aug-cc-pvDZ level calculations on methyl butanoate [33].

(c) CIS_4-4:

For the χ_1, χ_2 and χ_3 dihedrals, the same torsional potentials were used as those adopted for the corresponding angles of CB9CB. Rotational profiles for the C_{sp2}–C_{sp2}–C–C (χ_5) and C_{sp2}–C–C–C (χ_4) dihedrals were obtained by DFT/M06-2X/6-31+G** calculations respectively on *cis*-2-hexene and *cis*-2-heptene. The torsional profile relative to χ_5 shows two minima around ±105°, corresponding to conformations having a *skew*± geometry (Figure A.2(b)). The minima are rather broad: conformations with χ_5 in the ranges ~ ±(70°-180°) have a torsional energy lower than 3 kJmol^{-1}, and are thus expected to be appreciably populated at room temperature. These results are in agreement with those reported for *cis*-2-pentene at the MP2/6-311G** level of theory [35]. The profile relative to χ_4 exhibits well-defined *trans* and *gauche* energy minima (Figure A.2(c)): the most stable state corresponds to either the *gauche*+ or the *gauche*- configuration depending on the sign of χ_5: if χ_5 ~ +105°, then a *gauche*− state is preferred and vice-versa. The torsional preferences relative to the χ_4 and χ_5 dihedral angles, together with the fact that these angles are correlated, is at the origin of the elongated shape of the conformation of compound CIS_4-4 shown in Figure 8.2(c).

8.2.2 Monte Carlo conformational sampling

Fluctuations within the minima of the torsional potentials are expected to be important in the determining the average molecular shape of LC dimers: the superposition of small rotations around a large number of bonds can produce a significant change in the relative orientation of the terminal mesogenic units. Indeed, full account of the torsional distribution was found to be essential to obtain reliable predictions for the dielectric properties of liquid crystals dimers [36]. Therefore in the present study, conformations were generated using a RIS approach for the biphenyl twist angle, and Monte Carlo sampling of the full torsional potentials for the dihedrals in the spacer (see Chapter 5).

8.2.3 Bend angle and bend elastic constant profiles

In bent-core compounds the bend angle is determined by the shape of the aromatic core: since the latter is fairly rigid, the bend angle can be usually quantified using a single value, as shown in the previous Chapters. In dimers the bend angle θ can be defined as the angle between the *para* axes of the two mesogenic units, as schematically shown in Figure 8.3. Values of $\theta \sim 0°$ correspond to hairpin conformations, having nearly parallel mesogenic units; values of $\theta \sim 180°$ correspond to elongated conformations, having nearly antiparallel mesogenic units. Since the spacer connecting these units is flexible, a distribution of values between these extremes is expected. In this work we calculated the bend angle probability according to:

$$p(\theta)\sin\theta = \frac{\int e^{-V(\chi)/k_B T} Q_\chi \, \delta\left(\theta - \theta(\chi)\right) \, d\chi}{\int e^{-V(\chi)/k_B T} Q_\chi \, d\chi} \quad , \tag{8.1}$$

where χ is the set of dihedral angles which specify a certain conformation, having a bend angle $\theta(\chi)$, an intrinsic torsional energy $V(\chi)$ and an orientational partition function Q_χ (see Eq. 5.3), and $\delta\left(\theta - \theta(\chi)\right)$ is the Dirac delta function. The shape of the bend angle distribution depends therefore on the molecular geometry, on the intrinsic conformational preferences and on the degree of orientational order of the liquid crystalline environment.

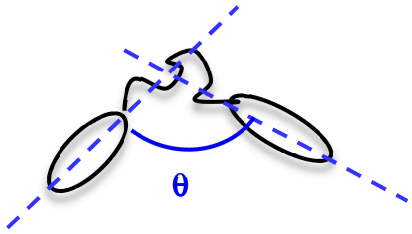

Figure 8.3. Cartoon showing the bend angle θ in liquid crystal dimers. The black ellipses represent the mesogenic units and the black irregular curve the flexible spacer.

The dependence of the bend elastic constant K_{33} on the bend angle θ was also examined. For this purpose the average contribution given to K_{33} by all conformations having a certain value of the bend angle was calculated, according to:

$$K_{33}(\theta) = \frac{\int K_{33}(\boldsymbol{\chi}) e^{-V(\boldsymbol{\chi})/k_B T} Q_{\boldsymbol{\chi}} \delta\left(\theta - \theta(\boldsymbol{\chi})\right) d\boldsymbol{\chi}}{\int e^{-V(\boldsymbol{\chi})/k_B T} Q_{\boldsymbol{\chi}} \delta\left(\theta - \theta(\boldsymbol{\chi})\right) d\boldsymbol{\chi}} \quad , \tag{8.2}$$

where $K_{33}(\boldsymbol{\chi})$ is the bend elastic constant calculated for the conformation specified by the set of torsional angles $\boldsymbol{\chi}$ (see Eq. 5.9).

8.3 Results and discussion

Figure 8.4 shows the splay (K_{11}), twist (K_{22}) and bend (K_{33}) elastic constants calculated for the liquid crystal dimers OCO, CB9CB, and CIS_4-4, as a function of S_{CB}, the order parameter for the *para* axis of the cyanobiphenyl group. Calculations were performed assuming a uniaxial nematic phase in the whole range of order parameter considered. On the basis of the comparison between our predictions and experimental data for other liquid crystal systems, the error on the calculated elastic constants can be estimated to be of the order of a few piconewtons (see for example the results reported in the previous Chapters for bent-core compounds).

For the ester-linked dimer OCO (Figure 8.4(a)) we predict $K_{11} > K_{22} \geq K_{33}$, together with very low values of the bend elastic constant. The splay and twist elastic constant increase with increasing order parameter, whereas the bend elastic constant is almost independent of it, though a slow decrease can be observed at high ordering. Using the same computational methodology employed here, very similar results have been

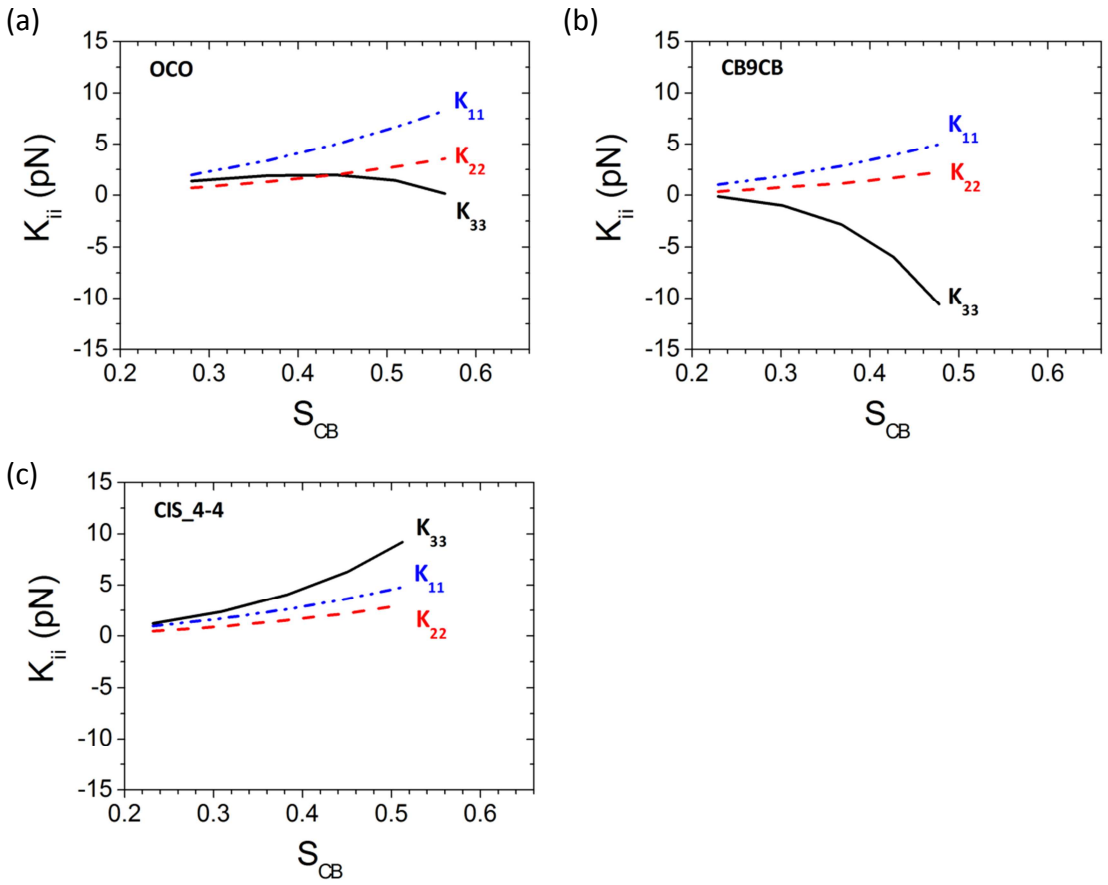

Figure 8.4. Splay (K_{11}, blue dot-dot-dashed line), twist (K_{22}, red dashed line) and bend (K_{33}, black solid line) elastic constants calculated for (a) OCO, (b) CB9CB, (c) CIS_4-4, as a function of the order parameter for the *para* axis of the cyanobiphenyl unit (S_{CB}).

obtained for odd dimers having ether linkages (–O–), instead of ester ones, between the mesogenic units and the spacer [6]. In that work, the unusual elastic behaviour of ether-linked odd dimers was shown to be a consequence of their bent molecular shape.

Also for the methylene-linked CB9CB dimer $K_{11} > K_{33}$ is obtained (see Figure 8.4(b)). However the bend elastic constant is clearly distinct from that of the OCO dimer: negative values are obtained, which decrease steadily as the order parameter increases. The meaning of these negative values has already been discussed in Chapter 3, and we will return on this point later on in the text.

Quite different results were obtained for the dimer having a *cis* double-bond along the spacer (CIS_4-4): as shown in Figure 8.4(c), $K_{33} > K_{11} > K_{22}$ is predicted, with a bend elastic constant which increases with increasing order, in common with conventional rod-like liquid crystals. Qualitatively similar elastic properties were predicted also for ether-linked dimers having an even-membered spacer, and were ascribed to their

average elongated shape [6].

For better comparison the splay, bend and twist elastic constants of the three compounds are plotted together in Figure 8.5, together with the values calculated for a conventional rod-like liquid crystals (8OCB). It is clear that, among the three elastic constants, K_{33} is the most sensitive to the details of the chemical structure.

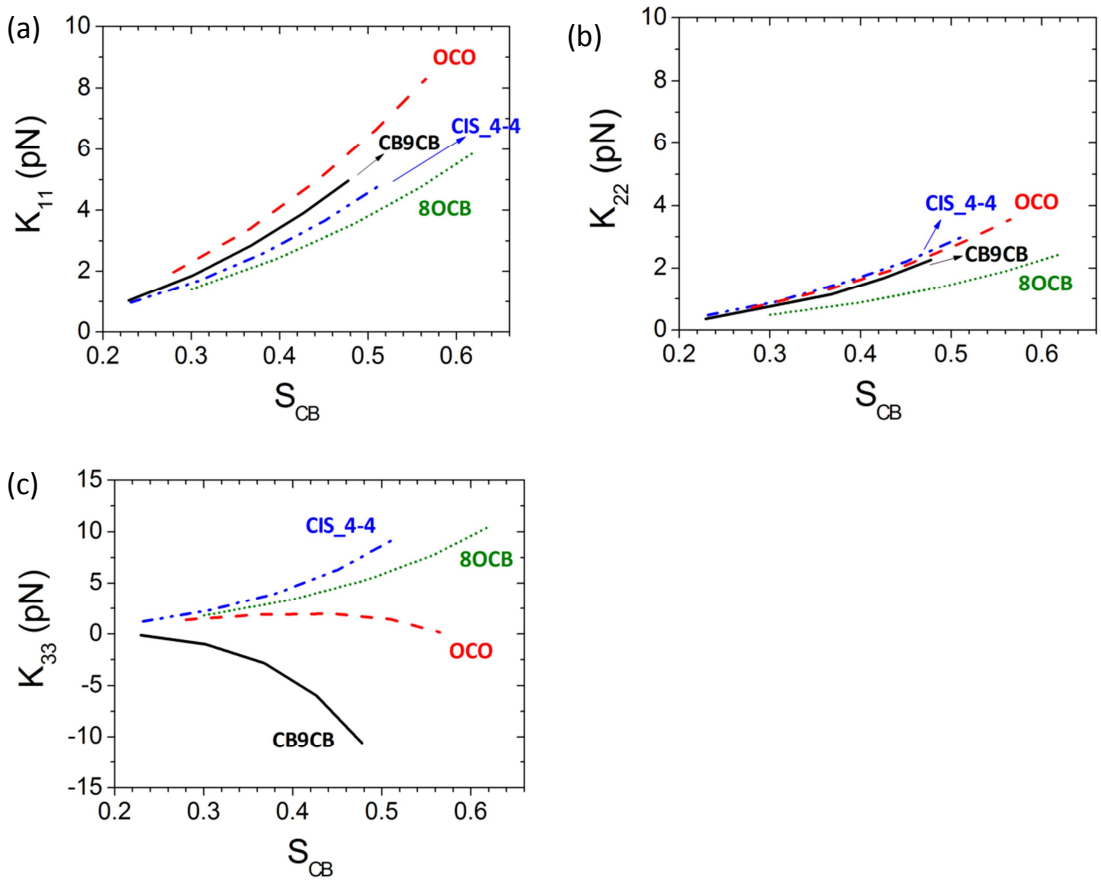

Figure 8.5. (a) Splay (K_{11}) , (b) twist (K_{22}) and (c) bend (K_{33}) elastic constants for the liquid crystal dimers investigated in this work, as function of the order parameter for the *para* axis of the cyanobiphenyl unit (S_{CB}): CB9CB (black solid line) , OCO (red dashed line), CIS_4-4 (blue dot-dot-dashed line). The results obtained for the rod-like liquid crystal 8OCB are also shown for comparison (green dotted line).

In order to understand how the observed differences in bend elasticity are related to the molecular structure, we calculated the bend angle probability distribution for CB9CB, OCO and CIS_4-4, according to Eq. (8.1). The results obtained for a value the order parameter S_{CB} ~ 0.5 are compared in Figure 8.6(a). In spite of the fact that the distributions are broadened by the effect of the conformational freedom, clear differences remain between the three compounds. For CB9CB the highest probability is

found in the range* θ ~ 100°-150°, corresponding, on average, to a bent molecular shape. For OCO the maximum shifts towards higher values of the bend angle, θ ~ 110°-160°, corresponding to slightly less bent conformations. Finally for CIS_4-4 values in the range θ ~ 130°-170° are predicted, with a significant probability for elongated conformations.

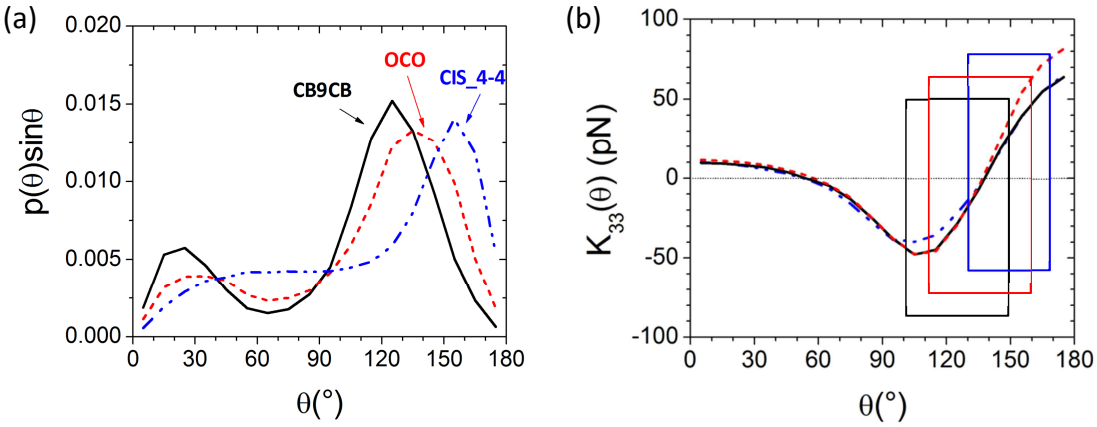

Figure 8.6. (a) Probability distribution for the bend angle θ between the *para* axes of the cyanobiphenyl units calculated for: CB9CB (black solid line), OCO (red dashed line), and CIS_4-4 (blue dot-dot-dashed line). (b) Bend elastic constant (K_{33}) as a function of the bend angle θ for: CB9CB (black solid line), OCO (red dashed line), and CIS_4-4 (blue dot-dot-dashed line). The boxes superposed to the curves highlight the region of highest bend angle probability, as deduced from the curves in (a): CB9CB (black box), OCO (red box), CIS_4-4 (blue box). The results in (a) and (b) were obtained for S_{CB} ~ 0.48 for CB9CB and CIS_4-4, S_{CB} ~ 0.51 for OCO.

These differences can be understood on the basis of the molecular geometric characteristics identified in Section 8.2.1. The bond angle connecting the mesogenic units to spacer is larger for an ester linkage ($C_{ar}\widehat{O}C$ ~ 123°) than for a methylene linkage ($C_{ar}\widehat{C}C$ ~ 113°); considering this difference, it is immediately clear that the bend angle for the dimers in their all-*trans* conformation, $\theta^{all-trans}$, is smaller in CB9CB than in OCO (compare Figure 8.2 (a) and (b)). Indeed we determined $\theta^{all-trans}$ ~ 112° for CB9CB and $\theta^{all-trans}$ ~ 152° for OCO. The results reported in Figure 8.6(a) show that this difference is not entirely washed out by the conformational freedom. For CIS_4-4, the prevalence of elongated, rather than bent, conformations is the result of the torsional preferences for the dihedrals angles flanking the double bond (χ_4, χ_5 and their

* Here and in the following the range is determined as full width at half maximum (FWHM) of the peak of highest probability.

equivalents in Figure 8.2(c)), discussed in Section 8.2.1. As a consequence the molecular shape is well different from the bent structure obtained by simple molecular drawings (Figure 8.1(c)) .

These differences in the degree of molecular bending are qualitatively sufficient to understand the different bend elastic behaviours predicted for CB9CB, OCO and CIS_4-4. To put this relationship on a more quantitative basis, for each compound we calculated the bend elastic constant K_{33} as a function of the bend angle θ, according to Eq. (8.2). The results obtained for a value of the order parameter $S_{CB} \sim 0.5$ are shown in Figure 8.6(b). Very similar profiles are obtained for the three compounds, at variance with what found for the bend angle probability distribution. The latter determines the overall elastic response (Figure 8.5(c)) by preferentially sampling different regions of the $K_{33}(\theta)$ profile, as illustrated schematically by the rectangular boxes in Figure 8.6(b). For example for CB9CB the probability maximum includes a large number of conformations having negative values of the bend elastic constant, whereas for CIS_4-4 most of the $K_{33}(\theta)$ values falling in the angular range of maximum probability are positive.

We can try to compare our predictions for the elastic constants with the experimental data available in literature. Unfortunately measurements of the elastic constants of dimers are scarce, so we will also consider data obtained for compounds different from the ones studied here, but with a closely related structure. In Ref. [37] the splay and bend elastic constants were measured for a series ester-linked dimers having the same number of carbon atoms in the spacer as OCO. It is difficult to make a quantitative comparison, since the authors do not report the individual elastic constants but only their average value, $K = (K_{11}+K_{33})/2$, as a function of temperature rather than of order parameter. However the result obtained in Ref. [37] indicates that the average elastic constant K of ester-linked dimers is similar to that of ether-linked dimers, for which the same authors have reported K_{11} and K_{33} individually [7]. For the latter, results qualitatively similar to the ones reported here for OCO were obtained: K_{11} was found to increase with decreasing temperature (that is with increasing order parameter), whereas K_{33} was found to be low and almost temperature independent. Our predictions for CB9CB can be compared to the results obtained for CBF9CBF [18]: the molecular structure of this compound differs from that of CB9CB only for the presence of fluorine

substituents in the mesogenic units, in a position where they cannot significantly affect the molecular shape. Adding CBF9CBF to a mixture of ether-linked dimers resulted in a significant relative decrease of the bend elastic constant with respect to the pure host; in comparison a smaller relative change was measured for the splay elastic constant. These results suggest that CBF9CBF should have a smaller K_{33} than the host, but a similar K_{11}, in qualitative agreement with our predictions (Figure 8.5(a) and (c)).

The results obtained in this work also allow us to make some considerations about the influence of the linking group on the occurrence of the twist-bend nematic phase (N_{TB}). This new kind of nematic organization has been detected mainly in methylene-linked dimers including CB7CB [9,11-14], CB9CB [16,17], CBF9CBF [18] and CB11CB [17,19,20]. In these systems the transition from the conventional N phase to the N_{TB} phase occurs at temperatures fairly close to the nematic-isotropic (N-I) transition: as a result the nematic phase has a relatively small stability range. The N_{TB} organization appears to be less common in ether-linked dimers: for compound FFO9OCB [22] and for a mixture of ether-liked dimers [18], an N_{TB} phase has been observed at temperatures much below the N-I transition; for another compound, the N_{TB} phase was detected in an extremely narrow temperature interval, of only one degree, between the overlying nematic and underlying smectic A phase [23]. The mesomorphic behaviour of a series of ester-linked dimers with different chain length has also been investigated and none of them was found to form a N_{TB} phase [38].

Recently we have developed a Maier-Saupe-like molecular model for the formation of the N_{TB} phase in a system of idealized rigid V-shaped particles (see Chapter 3) [39]. We showed that the phase behaviour of bent particles is strongly sensitive to the molecular bend angle: the N_{TB} phase was predicted to form only for sufficiently low values of the bend angle (about less than 150°), at temperatures progressively closer to the N-I transition as the bend angle is reduced. The model also allowed us to clarify the relationship between the phase behaviour of bent particles and their bend elasticity. We showed that the bend elastic constant of the N phase gradually softens on approaching the N_{TB}-N phase transition, vanishing at the transition. Combining the predictions of this generic model with the results obtained in this work for real systems, we can give an interpretation of the experimental evidence reported above.The fact that an N_{TB} phase has been observed for methylene-linked but not for ester-linked dimers can be

traced back to the different molecular shape of these dimers, with the first more bent than the latter, as indicated by the bend angle distributions calculated here (Figure 8.6(a)).

The different bend elasticity predicted for the methylene-linked and for the ester-linked compounds (Figure 8.5(c)) is consistent with the observed phase behaviour. The calculated K_{33} of OCO, which is small but positive over a wide range of order parameters, suggests that spontaneous bend deformation should appear only at low temperature. For CB9CB, K_{33} is predicted to be negative over the entire range of order parameters considered, implying that the N_{TB} phase should appear directly from the isotropic phase, in contrast to the experimental findings. However, the uncertainties in the calculated elastic constant, which we can estimate to be of a few piconewtons, can lead to some variability in the value of the order parameter at which the bend elastic constant changes from positive to negative. Taking into account this uncertainty, and considering that the nematic phase of CB9CB is stable only in a relatively narrow range before the N_{TB} phase appears, we can state that the observed discrepancy is not too severe.

8.4 Conclusions

We have calculated the splay (K_{11}), twist (K_{22}) and bend (K_{33}) elastic constants of liquid crystal dimers with different linking groups between the mesogenic units and the spacer: a methylene-linked dimer, an ester-linked dimer and a compound with a *cis*-double bond in the middle of the spacer. On the basis of the results obtained, three main observations can be made: (*i*) among the three elastic constants, K_{33} is the most sensitive to changes in the molecular structure; (*ii*) in liquid crystals dimers, even small details of the chemical structure, such as the nature of the linking group, can have a dramatic effect on K_{33}; (*iii*) three markedly different kinds of elastic behaviours can be distinguished, according to the values and trend with order parameter of the bend elastic constant K_{33}, as summarized in Table 8.1. In addition to the compounds reported here, a large number of other dimers with various chemical structures have been investigated during this thesis: apart from obvious differences in the numerical values of their elastic constants, all of them could be classified into these three groups.

The differences in the bend elastic behaviour of the dimers could be ascribed to their

Behaviour Type	K_{33}	Representative Compound	Molecular Shape
I	Low, decreasing with *S*	CB9CB	Bent
II	Low, almost independent of S	OCO	Fairly bent
III	High, increasing with *S*	CIS_4-4	Elongated

Table 8.1. Classifications of dimers into groups according to their bend elasticity.

different molecular shape, which ranges from bent for CB9CB, to fairly bent for OCO, to elongated for CIS_4-4. These observations about the molecular shape of the dimers were drawn taking into account the full distribution of molecular conformations, and not only the geometry of the all-*trans* conformation, as usually done in the literature. Combining the results obtained in this work with the predictions of a generalized Maier-Saupe model for the phase behaviour of V-shaped particles (Chapter 3)[39], we could discuss the influence of the linking group on the occurrence of the twist-bend nematic phase, thus providing a molecular interpretation of the experimental observations.

8.5 References

1 C. T. Imrie and P. A. Henderson, *Chem. Soc. Rev.*, 2007, **36**, 2096–2124.

2 A. Ferrarini, G. R. Luckhurst , P. L. Nordio and S. J. Roskilly, *J. Chem. Phys.*, 1994, **100**, 1460-1469.

3 G. R. Luckhurst, *Macromol. Symp.*, 1995, **96**, l-26.

4 J. S. Patel and R. B. Meyer, *Phys. Rev. Lett.*, 1987, **58**, 1538-1540.

5 S. M. Morris, M. J. Clarke, A. E. Blatch and H. J. Coles, *Phys. Rev. E.*, 2007, **75**, 041701.

6 M. Cestari, E. Frezza, A. Ferrarini and G. R. Luckhurst, *J. Mater. Chem.*, 2011, **21**, 12303-12308.

7 K. L. Atkinson, S. M. Morris, F. Castles, M. M. Qasim, D. J. Gardiner and Harry J. Coles, *Phys. Rev. E*, 2012, **85**, 012701.

8 I. Dozov, *Europhys. Lett.*, 2001, **56**, 247–253.

9 M. Cestari, S. Diez-Berart, D. A. Dunmur, A. Ferrarini, M. R. de la Fuente, D. J. B. Jackson, D. O. Lopez, G. R. Luckhurst, M. A. Perez-Jubindo, R. M. Richardson, J. Salud, B. A Timimi and H. Zimmermann, *Phys. Rev. E*, 2011, **84**, 031704.

10 P. A. Henderson and C. T. Imrie, *Liq. Cryst.*, 2011, **38**, 1407-1414.

11 L. Beguin, J. W. Emsley, M. Lelli, A. Lesage, G. R. Luckhurst, B. A. Timimi and H. Zimmermann, *J. Phys. Chem. B*, 2012, **116**, 7940–7951.

12 C. Greco, G. R. Luckhurst and A. Ferrarini, *Phys. Chem. Chem. Phys.*, 2013, **15**, 14961-14965.

13 C. Meyer, G. R. Luckhurst and I. Dozov, *Phys. Rev. Lett.*, 2013, **111**, 067801.

14 D. Chen, J. H. Porada, J. B. Hooper, A. Klittnick, Y. Shen, M. R. Tuchband, E. Korblova, D. Bedrov, D. M. Walba, M. A. Glaser, J. E. Maclennan and N. A. Clark, *Proc. Natl. Acad. Sci. U.S.A.*, 2013, **110**, 15931–15936.

15 V. Borshch, Y.-K. Kim, J. Xiang, M. Gao, A. Jakli, V. P. Panov, J. K. Vij, C. T. Imrie, M. G. Tamba, G. H. Mehl and O. D. Lavrentovich, *Nat. Commun.*, 2013, **4**, 2635.

16 C.S.P. Tripathi, P. Losada-Pérez, C. Glorieux, A. Kohlmeier, M.-G.Tamba, G. H. Mehl and J. Leys, *Phys. Rev. E*, 2011, **84**, 041707.

17 R. Balachandran, V. P. Panov, Y. P. Panarin, J. K. Vij, M. G. Tamba, G. H. Mehl and J. K. Song, *J. Mater. Chem. C*, 2014, **2**, 8179–8184.

18 K. Adlem, M. Čopič, G. R. Luckhurst, A. Mertelj, O. Parri, R. M. Richardson, B. D. Snow, B. A. Timimi, R. P. Tuffin and D. Wilkes, *Phys. Rev. E*, 2013, **88**, 022503.

19 V. P. Panov, M. Nagaraj, J. K. Vij, Yu. P. Panarin, A. Kohlmeier, M. G. Tamba, R. A. Lewis and G. H. Mehl, *Phys. Rev. Lett.*, 2010, **105**, 167801.

20 R. J. Mandle, E. J. Davis, C. T. Archbold, S. J. Cowling and J. W. Goodby, *J. Mater. Chem. C*, 2014, **2**, 556.

21 R. J. Mandle, E. J. Davis, C.-C.A. Voll, C. T. Archbold, J. W. Goodby and S.J. Cowling, *Liq. Cryst.*, 2014, doi: 10.1080/02678292.2014.974698.

22 N. Sebastián, D. O. López, B. Robles-Hernández, M. R. de la Fuente, J. Salud, M. A. Pérez-Jubindo, D. A. Dunmur, G. R. Luckhurst and D. J. B. Jackson, *Phys. Chem. Chem. Phys.*, 2014, **16**, 21391

23 R. J. Mandle, E. J. Davis, S. A. Lobato, C. C. A. Voll, S. J. Cowling and J. W. Goodby, *Phys. Chem. Chem. Phys.*, 2014, **16**, 6907–6915.

24 M. J. Frisch *et al.*, Gaussian 09 (Revision B.01), Gaussian, Inc., Wallingford CT, 2010.

25 M. P. Johansson, J. Olsen, *J. Chem. Theory Comput.*, 2008, **4**, 1460-1471.

26 Y. Zhao and D. G. Truhlar, *Theor. Chem. Account*, 2008, **120**, 215-241.

27 G. Cinacchi, G. Prampolini, *J. Phys. Chem. A*, 2003, **107**, 5228-5232.

28 J. B. Klauda, R. W. Pastor, B. R. Brooks, *J. Phys. Chem. B*, 2005, **109**, 15684-15686.

29 A. Salam and M. S. Deleuze, *J. Chem. Phys.*, 2001, **116**, 1296-1302.

30 S. Halbert, C. Clavaguéra, G. Bouchoux, *J. Comput. Chem.*, 2011, **32**, 1550-1560.

31 X.Tong, M. S. Ford, C. E. H. Dessent and K. Muller-Dethlefs, *J. Chem. Phys.*, 2003, **119**, 12908-12913.

32 K. E. Riley, M. Pitoňák, P. Jurečka and P. Hobza, *Chem. Rev.*, 2010, **110**, 5023–5063.

33 G. D. Smith, D. Bedrov, O. Byutner, O. Borodin, C. Ayyagari and T. D. Sewell, *J. Phys. Chem. A*, 2003, **107**, 7552-7560.

34 P. I. Nagy, F. R. Tejada, J. G. Sarver and W. S. Jr. Messer, *J. Phys. Chem. A*, 2004, **108**, 10173-10185.

35 G. D. Smith and W. J. Paul, *J. Phys. Chem. A*, 1998, **102**, 1200-1208.

36 M. Cestari, PhD Thesis, University of Padova, 2009.

37 K. L. Atkinson, S. M. Morris, M. M. Qasim, F. Castles, D. J. Gardiner, P. J. W. Hands, S. S. Choi, W.-S Kim and H. J. Coles, *Phys. Chem. Chem. Phys.*, 2012, **14**, 16377–16385.

38 L. Zhibao, P. A. Henderson, B. J. A. Paterson and C. T. Imrie, *Liq. Cryst.*, 2014, **41**, 471-483.

39 C. Greco, G. R. Luckhurst and A. Ferrarini, *Soft Matter*, 2014, **10**, 9318-9323.

Chapter 9

Enantiotopic discrimination and director organization in the N_{TB} phase*

9.1 Introduction

The odd liquid crystal dimer 1″,7″-bis(4-cyanobiphenyl-4′-yl)heptane (CB7CB), whose structure is shown in Figure 9.1(a), was the first compound for which a twist-bend nematic phase (N_{TB}) was experimentally identified, by Cestari *et al*. [1]. The N_{TB} phase structure has been described in Chapter 2: it is characterized by a heliconical director which precesses in space about an axis with conical angle θ_0 and helical pitch p. Both right- and left- handed helicity are possible, with equal probability (Figure 9.1(c))[2].

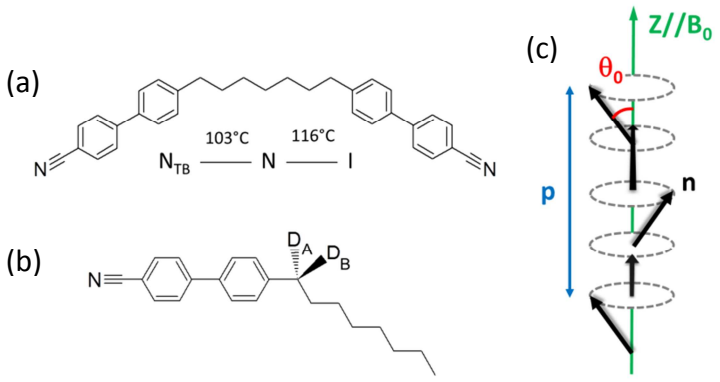

Figure 9.1. (a) Molecular structure and phase sequence of CB7CB: I=Isotropic, N=Nematic, N_{TB}=Twist-Bend Nematic. (b) Molecular structure of 8CB-d_2. The label of the two prochiral deuterons is shown. (c) Scheme of the director organization in the N_{TB} phase: *Z* is the helix axis, **n** is the local director, *p* is the helical pitch and θ_0 is the conical angle. $\mathbf{B}_0$ is the static magnetic field in the NMR spectrometer.

* This Chapter is adapted from: C. Greco, G. R. Luckhurst and A. Ferrarini, *Phys. Chem. Chem. Phys*., 2013, **15**, 14961-14965.

At the time when the experiments were done, the identity of the second nematic phase (N_X) formed by CB7CB and other odd dimers with similar structure [3,4] was completely unknown. Of particular importance for the phase identification were the results provided by ^{2}H-NMR spectroscopy. Experiments were conducted either on deuterated CB7CB-d_4 samples [1] or using deuterated probes, such as 4-octyl-4′-cyanobiphenyl (8CB-d_2, shown in Figure 9.1(b)), dissolved in the CB7CB host [5]. The loss of equivalence of prochiral deuterons in the N_X phase unequivocally demonstrated the chirality of the phase. The formation of a chiral phase from achiral molecules is an intriguing result: inspired by earlier theoretical predictions [2], the authors interpreted it as a sign of an N_{TB} organization[†].

In order to test this interpretation and to get further insight into the director organization, we have developed a molecular model for the long-range orientational order in the N_{TB} phase. A model suitable for this purpose must be able to account for the coupling between the molecular structure and the modulated twist-bend environment. In addition, a high resolution molecular level description is needed for the prediction of NMR observables. We have calculated the quadrupolar splittings of the deuterated probe 8CB-d_2 as a function of the structural parameters (conical angle and pitch) that characterize the twist-bend modulation. Combining our prediction with the experimental data [5] we characterized the structure of the N_{TB} phase of CB7CB. The origin of the enantiotopic discrimination between prochiral sites has also been examined, in relation to the molecular and environmental chirality.

In Section 9.2 the ^{2}H-NMR experimental findings will be summarized. The molecular model will be described in Section 9.3. The results obtained will be presented and discussed in Section 9.4.

9.2 ^{2}H-NMR: experimental findings

As stated in Chapter 1, the ^{2}H-NMR spectrum of a deuterated molecule in an orientationally ordered environment is dominated by the quadrupolar interaction between the electric quadrupole moment of the nucleus and the electric-field-gradient [6,7]. Because of the quadrupolar interaction, deuterons give rise to a doublet of signals

[†] Hereafter the N_X phase will be always referred to as an N_{TB} phase.

in the NMR spectrum (Figure 9.2). The separation between the two components of the doublet is called the quadrupolar splitting $\Delta\nu$ and its magnitude depends on the orientation of the carbon-deuterium (C–D) bond with respect to the direction of the external magnetic field. If the molecular motions are fast on the time scale of the NMR experiment and if the director is homogenously oriented with respect to the magnetic field, narrow spectral lines are observed, with a quadrupolar splitting $\Delta\nu$ given by [7,8]:

$$\Delta\nu = \frac{3}{2} q_{CD} \left| S_{CD} \right| \quad . \tag{9.1}$$

Here q_{CD} is the component, along the C–D bond, of the deuterium quadrupolar coupling tensor (assumed to be axially symmetric) and S_{CD} is the order parameter of the C–D bond with respect to the direction of the magnetic field[‡]:

$$S_{CD} = \frac{3}{2} \left\langle \cos^2 \beta_{CD} \right\rangle - \frac{1}{2} \ , \tag{9.2}$$

where β_{CD} is the angle between the C–D bond and the magnetic field and the angular brackets denotes an orientational average. In principle, for non-uniform systems (such as the N_{TB} phase), time-scale considerations and, if appropriate, averaging should be extended also to the positional variables. However, this is not needed for a periodic twist-bend modulation, since in this case, because of the helical symmetry, molecular translation along the helix axis has the same effect as rotation with respect to the local director. If a molecule contains more than one deuteron, a doublet is obtained for each non-equivalent site, where the equivalence is determined by the molecular and phase symmetries [9].

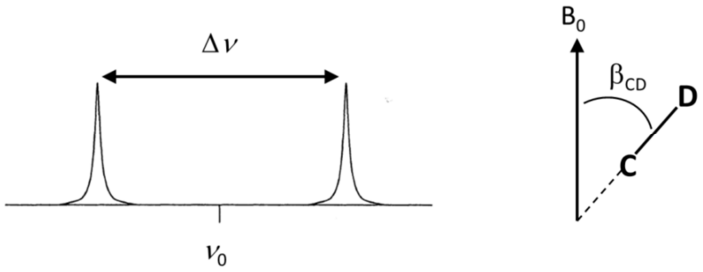

Figure 9.2. ^{2}H-NMR spectrum of a molecule containing a single deuterium site. The quadrupolar splitting $\Delta\nu$ depends on β_{CD}, the angle between the direction of the external magnetic field $\mathbf{B}_0$ and C–D bond.

[‡] Order parameters have been defined in Chapter 1.

Figure 9.3(a)-(b) shows the experimental ^{2}H-NMR spectrum of the achiral deuterated probe 8CB-d_2 dissolved in CB7CB, at two different temperatures above and below the N_{TB}-N phase transition [5].

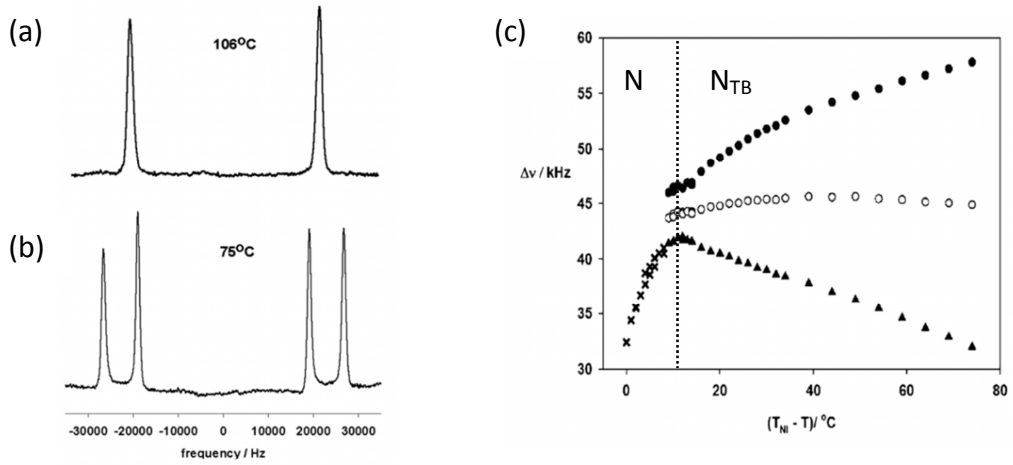

Figure 9.3. ^{2}H-NMR spectrum of 8CB-d_2 in the CB7CB host: (a) N phase, (b) N_{TB} phase. (c) Temperature dependence of the quadrupolar spittings. Data in the N phase are given as ×. Splittings in the N_{TB} phase are indicated as ● and ▲, and their average as ○. The dashed vertical line indicates the N_{TB}-N phase transition. Adapted with permission from [5]. Copyright 2012 American Chemical Society.

In the N phase a single doublet is observed, consistent with the C_s symmetry of the probe and the $D_{\infty h}$ symmetry of the phase. On the contrary two doublets with different quadrupolar splitting are present in the N_{TB} phase, indicating that the deuterons have lost their equivalence: in Ref. [5] this was attributed to a change in the phase symmetry from $D_{\infty h}$ to D_{∞}. The temperature dependence of the quadrupolar splittings in the N and N_{TB} is shown in Figure 9.3(c). In the N phase $\Delta\nu$ increases with decreasing temperature, as a result of the increase in the degree of orientational order. In the N_{TB} phase a striking temperature dependence is observed:

(i) one quadrupolar splitting increases with decreasing temperature, while the other decreases: the splitting difference , $\Delta(\Delta\nu) = \Delta\nu_B - \Delta\nu_A$, increases from about 3 kHz at the N_{TB}–N transition to about 26 kHz at 74 K below the nematic–isotropic transition. These is a very large difference in comparison to those measured in common chiral nematic solvents [10].

(ii) The average value $\overline{\Delta\nu} = (\Delta\nu_A + \Delta\nu_B)/2$, is nearly independent of temperature, being approximately equal to 45 kHz. The jump in the splitting at the N_{TB}-N transition

is in keeping with the first-order character of this transition [1,5].
Analogous features are exhibited by the ^{2}H-NMR spectra of CB7CB-d_4 [1].

9.3 Theoretical and computational methods

Our model for the orientational order in the N_{TB} phase is based on an extension of the the Surface Interaction (SI) model [11], which was originally developed for the conventional N phase. The SI model has been described in Chapter 5; here only the aspects relevant to the extension proposed here are presented.
The starting point is the orienting molecular field potential, Eq. 5.1. This expression is especially suitable for predicting the quadrupolar splittings in the N_{TB} phase, because it couples the specific features of a given molecular structure (through the molecular surface) with the local phase organization (through the positional dependence of the director). In a laboratory frame with the Z axis parallel to the helix axis of the N_{TB} phase, the components of the director **n** are expressed as follows:

$$\mathbf{n} = \left(\sin\theta_0 \cos\phi, \sin\theta_0 \sin\phi, \cos\theta_0\right) \quad , \tag{9.3}$$

where θ_0 is the conical angle and ϕ is the azimuthal angle, defined as $\phi = 2\pi Z/p$, with p being the helical pitch ($p > 0$ for a right-handed helix and $p < 0$ for a left-handed helix). For θ_0 = 0° the conventional nematic and for θ_0 = 90° the chiral nematic director organizations are recovered. If a molecule has a finite number of rapidly interconverting conformers (on the NMR timescale), the S_{CD} order parameter in Eq. (9.2) is defined by the orientational-conformational average:

$$S_{CD} = \sum_J w_J \left(\frac{3}{2} \left\langle \cos^2 \beta_{CD} \right\rangle_J - \frac{1}{2} \right) \quad , \tag{9.4}$$

where the angular bracket denotes the orientational average for the Jth conformer and w_J is the statistical weight of this conformer:

$$w_J = \frac{\exp\left[-V_J / k_B T\right] Q_J}{\sum_M \exp\left[-V_M / k_B T\right] Q_M} . \tag{9.5}$$

The probability w_J is determined by both V_J, the torsional energy of the conformer in the isotropic phase, and U_J^{or}, the potential of mean torque in the liquid crystalline environment, which enters Eq. (9.5) through the orientational partition function Q_J (see Eq. 5.3 of Chapter 5). The S_{CD} order parameters in Eq. (9.4) are defined with respect to the direction of the external magnetic field $\mathbf{B}_0$: this is parallel to the director **n** in the N phase and to the helix axis in the N_{TB} phase [5]. Therefore the partition function Q_J and the average $\left\langle \cos^2 \beta_{CD} \right\rangle_J$ were calculated by integration over the angles $\Omega = \{\alpha, \beta, \gamma\}$ that define the molecular orientation in the laboratory frame with its *Z* axis parallel to $\mathbf{B}_0$ (see Figure 9.4(a)). The quadrupolar splittings for the C–D_A and C–D_B bonds were finally obtained from the corresponding order parameters according to Eq. (9.1), assuming a value of the coupling constant q_{CD}=168kHz.

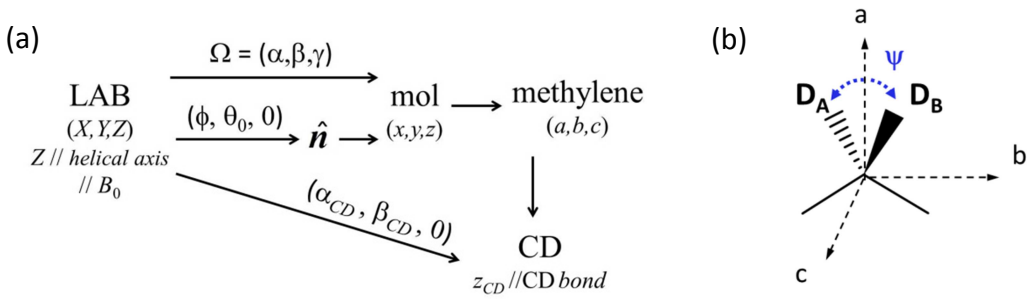

Figure 9.4. (a) Reference frames and the transformations between them. (b) Frame attached to the prochiral fragment.

Twenty-six conformers of 8CB were considered in the calculations: they are listed in Table 9.1. These were selected based on the torsional potentials for the various dihedral angles that define the conformational freedom of 8CB (see Figure 9.5). Two equivalent configuration ($\chi_0 \sim \pm 35°$) were assumed for the biphenyl twist angle [12], together with a single state of the C_{ar}-CH_2 bond ($\chi_1 = 90°$) [13]. Each bond in the alkyl chain (χ_2 - χ_7) has three minima, corresponding to the *trans* (*t*), *gauche*+ (*g*+) and *gauche*– (*g*–) states: we considered only conformers having no more than one *gauche* state in the alkyl chain. The energy difference between the *trans* and *gauche* states was evaluated by quantum mechanical calculations, at the DFT/M06-2X/6-31+G** level of theory [14][§]. For the

[§] Torsional potentials calculated in this thesis can be found in Appendix A.

dihedral angle χ_2, the value ΔV_2 = -1.1 kJ/mol was obtained (Figure A.3(e)), in agreement with the literature [15]. For all the other chain dihedrals ΔV_i = 2.2 kJ/mol was found (Figure A.1), a value in agreement with the results of high-level *ab initio* calculations [16]. The conformational energy of the each conformer was obtained as the sum of these contributions.

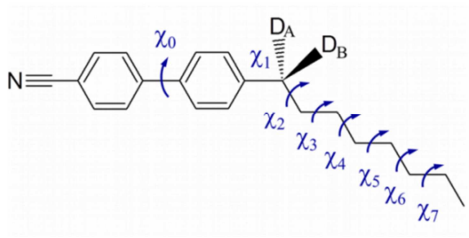

Figure 9.5. Molecular structure of 8CB-d_2 with labelling of the two prochiral deuterons and of the dihedral angles (the rotating dihedrals are indicated by arrows).

n.	Conformer	n.	Conformer	n.	Conformer
1	*Mtttttt*	**10**	*Mtg-tttt*	**19**	*Mttttg+t*
2	*Ptttttt*	**11**	*Mttg+ttt*	**20**	*Ptttg-t*
3	*Mg+ttttt*	**12**	*Pttg-ttt*	**21**	*Ptttg+t*
4	*Pg-ttttt*	**13**	*Pttg+ttt*	**22**	*Mttttg-t*
5	*Pg+ttttt*	**14**	*Mttg-ttt*	**23**	*Mttttg+*
6	*Mg-ttttt*	**15**	*Mttg+tt*	**24**	*Pttttg-*
7	*Mtg+tttt*	**16**	*Ptttg-tt*	**25**	*Pttttg+*
8	*Ptg-tttt*	**17**	*Ptttg+tt*	**26**	*Mttttg-*
9	*Ptg+tttt*	**18**	*Mttg-tt*		

Table 9.1. Conformers of 8CB considered in our calculations. Conformers are labeled by a six letter code: the first letter indicates the state of biphenyl (*P* and *M* for right- and left-handed twist, respectively) and the subsequent letters (*ttttt*, *g+tttt*, etc.) refer to the state of the χ_2 - χ_7 dihedrals .

9.4 Results and Discussion

The quadrupolar splittings were calculated as a function of the orienting strength ε and of the conical angle θ_0 and helical pitch p that characterize the director modulation in the N_{TB} phase. In the N phase (θ_0= 0°, $p \rightarrow\infty$) the splittings depend only on the orienting strength and increase with it. The open symbols in Figure 9.6(c) show the $\Delta\nu$ values corresponding to the experimental range in the N phase as a function of ε; the largest experimental splitting, $\Delta\nu^{max,N}$ ~ 42 kHz, was obtained for $\varepsilon^{max,N}$ ~ 0.023 Å^{-2}. In the N_{TB} phase the quadrupolar splittings necessarily depend on the conical angle, θ_0,

and the helical pitch, *p*. As explained by Beguin *et al*. [5], the S_{CD} order parameters for a pair of prochiral deuterons related by a molecular mirror plane can be expressed as:

$$S_{CD\pm} = S_{aa}\cos^2\frac{\psi}{2} + S_{cc}\sin^2\frac{\psi}{2} \pm S_{ac}\sin\psi \quad , \tag{9.6}$$

where ψ is the angle between the C–D bonds and the signs (+ and –) refer to each of the two enantiotopic sites. S_{ij} are elements of the local Saupe ordering matrix [17] (see Chapter 1) expressed in a reference frame (*a*,*b*,*c*), with *c* perpendicular to the molecular symmetry plane and *a* parallel to the bisector of the angle between the C–D bonds (Figure 9.4(b)). In the achiral nematic phase *c* is a principal axis of the Saupe matrix: consequently $S_{ac} = 0$ and the two quadrupolar splittings are identical. However, the two splittings can become different in a chiral environment in which $S_{ac} \neq 0$. Eq. (9.6) indicates that the quadrupolar splittings in the helical N_{TB} phase can be conveniently analysed in terms of their average value, $\overline{\Delta\nu}$, and their difference, $\Delta(\Delta\nu)$. The latter is a signature of the chirality of the environment and is thus directly related to the helical pitch. The average value $\overline{\Delta\nu}$ is determined only by the diagonal elements of the Saupe matrix, S_{aa} and S_{cc} : these measure the degree of alignment of the *a* and *c* molecular axes to the magnetic field and, for given values of ε and θ_0, are expected to be affected only slightly by the helical distortion of the director. Figure 9.6(a), shows, for a range of orienting strengths, the value of the conical angle θ_0^* that, according to our calculations, yields an average splitting equal to the experimental value in the N_{TB} phase, $\overline{\Delta\nu} = 45$ kHz. Comparison of the results obtained for *p* = 50 Å and 500 Å shows that, as expected, the helical pitch has only a small effect. We can see that the conical angle increases with the orienting strength, reaching a value of about 35°, which remains nearly constant at high ε values. Figure 9.6(b) shows the calculated splitting differences, $\Delta(\Delta\nu)$, plotted as a function of the parameters *p* and ε. Calculations were performed assuming for each (p,ε) pair the conical angle θ_0^* that yields $\overline{\Delta\nu}$ of 45 kHz (Figure 9.6(a)). Pitch values ranging from 50 to 500 Å and orienting strength values from ε = 0.0325 $Å^{-2}$ to 0.075 $Å^{-2}$ were assumed, suitable to cover the range of measured splittings

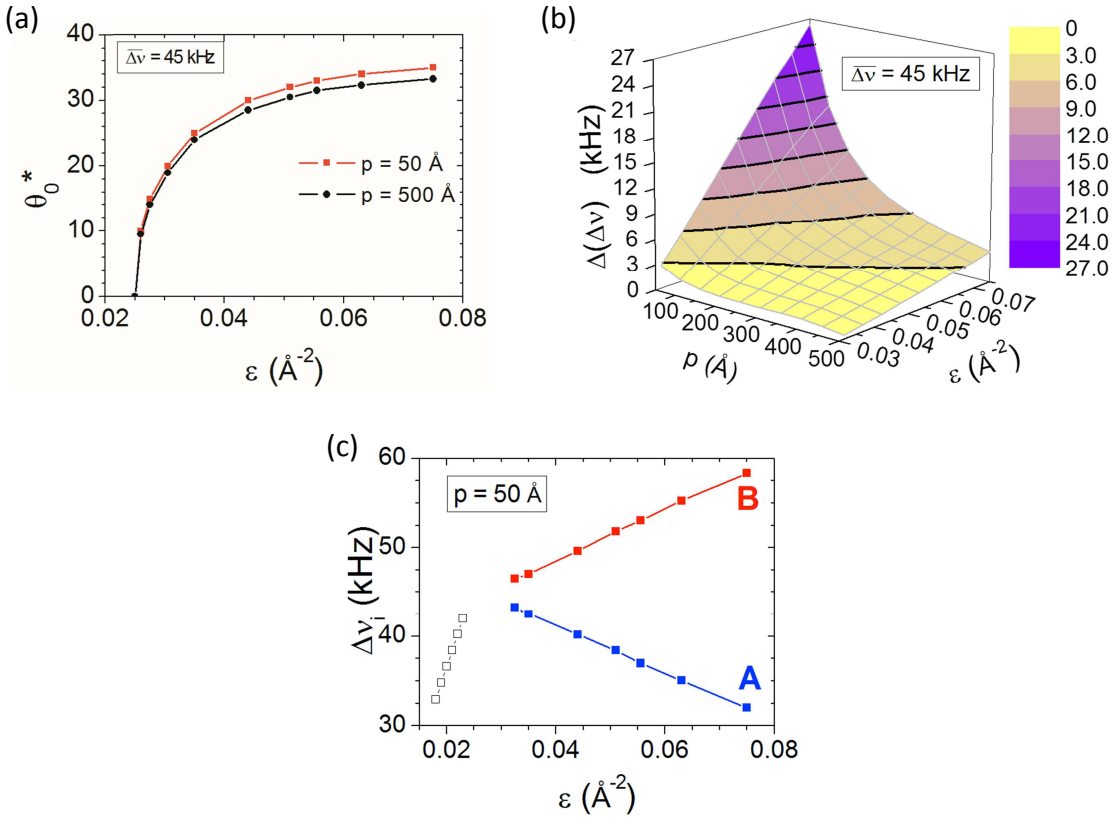

Figure 9.6. (a) The predicted values of the conical angle θ_0^* that yield a mean quadrupolar splitting $\overline{\Delta\nu}$ of 45 kHz, as a function of the orienting strength ε. The results obtained for two significantly different values of the helical pitch p are shown. (b) Difference in the quadrupolar splittings, $\Delta(\Delta\nu)$, calculated in the N_{TB} phase, as a function of the helical pitch, p, and of the orienting strength, ε. The color map identifies regions of different $\Delta(\Delta\nu)$ values with 3 kHz resolution, with black lines highlighting the boundaries between the regions. (c) Calculated quadrupolar splittings in the N phase (open symbols), and in the N_{TB} phase along a path of constant pitch p = 50 Å (closed symbols). The jump in ε appearing in the plot corresponds to the discontinuity in the degree of order at the N_{TB}–N transition.

in the N_{TB} phase, from $\Delta(\Delta\nu)^{\min,N_{TB}} \sim 3$ kHz found at the experimental N_{TB}–N transition to $\Delta(\Delta\nu)^{\max,N_{TB}} \sim 26$ kHz at about 60°C below this transition. The lower bound of pitch values is approximately twice as large as the length of a CB7CB molecule. There are several (p,ε) pairs that give a particular quadrupolar splitting difference; to guide the eye, lines of constant $\Delta(\Delta\nu)$ are shown the plot. Every path that starts at a point on the lowest boundary line (where $\Delta(\Delta\nu)$=3 kHz) and ends at the point where $\Delta(\Delta\nu)$= 26 kHz (*i.e.* p = 50 Å and ε = 0.075 Å^{-2}) represents, in principle, a possible evolution of the pitch and of the conical angle in the N_{TB} phase upon cooling. At the present stage of the model's development we are not able to identify the real

path. However our results clearly show that a very small pitch, of the order of a few molecular length (50-100 Å) is needed to give rise to the large difference in quadrupolar splitting measured experimentally. As an example, the closed symbols in Figure 9.6(c) show the quadrupolar splittings calculated in the N_{TB} phase along the path of constant pitch p = 50 Å. At the N_{TB}–N transition both the pitch and the conical angle undergo a discontinuous change (from $p \to \infty$ to p = 50 Å and from θ_0^* = 0° to θ_0^* ~ 22.5°), and upon further cooling the conical angle increases continuously. These results compare fairly well with various experimental evidences relative to the structure of N_{TB} phase of CB7CB. From measurements of an electronic effect, a helical pitch of 70 Å and a conical angle of about 11° at the N_{TB}–N transition were estimated [18]. Recent optical-birefringence experiments revealed that the conical angle increases significantly deep into the twist-bend nematic phase [19]. FFTEM allowed direct observation of the nanoscale periodicity, giving a pitch of about 80 Å and weakly temperature dependent [20].

Unlike the NMR experiments, we can distinguish which quadrupolar splitting corresponds to which deuteron. Here calculations were performed for a director forming a right-handed helix; for a left-handed helix the splittings for the two prochiral sites would be exchanged. Due to the impossibility of assigning the prochiral nuclei in the ^{2}H-NMR spectra, the analysis of experimental data for 8CB-d_2 does not allow us to distinguish between a homochiral organization and the coexistence of oppositely-handed domains in the N_{TB} phase. However, recent ^{2}H-NMR experiments using a deuterated chiral dopant dissolved in CB7CB together with a non-racemic mixture of the protonated dopant have confirmed the coexistence of chiral domains [21].

A common question in this context is whether the discrimination between prochiral sites is driven by the chirality of single conformers. Flexible molecules like 8CB, though being achiral, possess chiral conformers. However, these are present as enantiomorphic pairs, so a sample can be viewed as a racemic mixture. Net chirality could emerge from an imbalance in the population of enantiomorphic pairs due to a chiral environment. This has been a subject of long-standing interest and environment-induced deracemization has been invoked in different cases in liquid crystals [22-26]. Figure 9.7 shows the conformational distribution, calculated using Eq. (9.5), in the isotropic phase, in the nematic phase close to the N_{TB}-N transition (ε = 0.023 Å^{-2}) and in the N_{TB} phase (

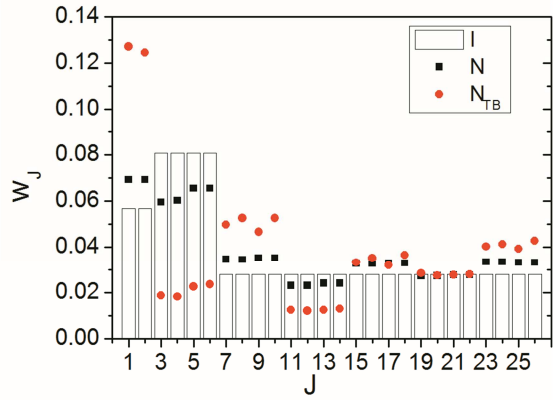

Figure 9.7. Conformer distribution calculated for 8CB in the isotropic (ε =0, bars), in the nematic (ε = 0.023 Å^{-2}, black squares) and in the N_{TB} phases (ε = 0.075 Å^{-2}, red circles). *J* is the conformer index, as reported in Table 9.1.

θ_0^*=35°, p = 50 Å, ε = 0.075Å^{-2}). A temperature of 376 K, comparable to the experimental N_{TB}-N transition temperature of the CB7CB liquid crystal host, was assumed in the Boltzmann exponent. The conformer probability in the isotropic phase is determined solely by the torsional potential, thus it reflects the *trans*/*gauche* energy difference. On the basis of the quantum mechanical data reported in Section 9.3, the most stable, and thus most probable, conformers are those having a *gauche* state in the first CH_2-CH_2 bond of the alkyl chain. The next most probable conformers are those with an all-*trans* chain; finally there are the conformers having a *gauche* state in a CH_2-CH_2 bond different from the first one, which all have the same probability. In the liquid crystal phases the statistical weight of conformers also depends on how well they are accommodated in the ordered environment. All-*trans* conformers, which are the most elongated, become the most stable, and some difference is introduced between conformers having a gauche in even (χ_2, χ_4, χ_6) or odd (χ_3, χ_5, χ_7) positions along the chain, the first less elongated than the last. The changes observed on moving from the isotropic to the N phase are magnified when the N_{TB} phase is considered, but this is only due to the higher ordering (larger ε-value in the calculations). There is a further effect that is peculiar to the chiral N_{TB} phase, that is the different probability of enantiomeric conformers (such as *Mtttttt* and *Pttttt* in Table 9.1). According to our calculations, this imbalance is very small for 8CB, clearly insufficient to yield the large splitting difference, $\Delta(\Delta\nu)$, observed experimentally. The enantiotopic discrimination originates from the interplay of molecular and local phase symmetry and does not necessarily

require molecular chirality [9]. To test the effect of the chiral environment alone, model calculations were carried out for a single, fictitious achiral conformers of 8CB-d_2, having an all-*trans* chain and perpendicular rings in the biphenyl moiety; this structure has C_s point symmetry. The result are reported in Figure 9.8. For each ε-value, the quadrupolar splittings were obtained assuming the same p and θ_0 values used for the calculations shown in Figure 9.6(c)[**]. In spite of the achirality of the fictious conformer, the predicted splitting differences are even larger than those reported in Figure 9.6(c), demonstrating the strong effect of the chiral N_{TB} environment, resulting from an extremely small helical pitch.

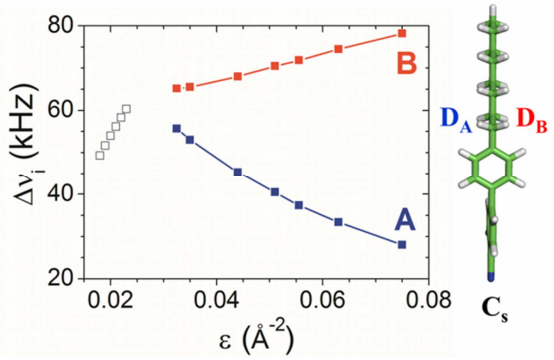

Figure 9.8. Quadrupolar splittings calculated for the achiral conformation of 8CB-d_2 shown on the right, in the nematic phase (open symbols) and in the N_{TB} phase along a path of constant helical pitch, p=50 Å (closed symbols).

9.5 Conclusions

In this work we have provided a molecular interpretation of the striking features of the ^{2}H-NMR spectra of 8CB-d_2 dissolved in the low-temperature nematic phase of the liquid crystal dimer CB7CB. This has been achieved using a model that combines an atomic-level description of the probe with a mean field description of orientational order. Our results support a N_{TB} organization for the low temperature phase, as originally proposed in Ref. [1]. From the comparison of calculated and experimental NMR data we have obtained quantitative estimates for the characteristic parameters, helical pitch p and conical angle θ_0, of the N_{TB} phase formed by CB7CB: our predictions have been confirmed by a number of experimental evidences [18-20].

[**] The results reported in Figure 9.8 are intended only to highlight the role of the molecular and environment chirality and should not be compared with the experimental data.

We have demonstrated that the enantiotopic discrimination observed in the ^{2}H-NMR spectra of 8CB-d_2 is determined by the interplay of molecular geometry and phase symmetry, and cannot be ascribed to the chirality of some conformers or to the population imbalance between enantiomorphic pairs of conformers, induced by the chiral environment. The approach we have proposed here allows us to assign the prochiral sites in deuterium spectra. Enantiomer assignment by NMR spectroscopy is a long-standing challenge [27]: it is certainly of value to explore whether the analysis of ^{2}H-NMR of chiral solutes in the N_{TB} phase [21] along the lines outlined here can be used for this purpose.

9.6 References

1 M. Cestari, S. Diez-Berart, D. A. Dunmur, A. Ferrarini, M. R. de la Fuente, D. J. B. Jackson, D. O. Lopez, G. R. Luckhurst, M. A. Perez-Jubindo, R. M. Richardson, J. Salud, B. A Timimi and H. Zimmermann, *Phys. Rev. E*, 2011, **84**, 031704.

2 I. Dozov, *Europhys. Lett.*, 2001, **56**, 247–253.

3 V. P. Panov, M. Nagaraj, J. K. Vij, Yu. P. Panarin, A. Kohlmeier, M. G. Tamba, R. A. Lewis and G. H. Mehl, *Phys. Rev. Lett.*, 2010,**105**, 167801.

4 P. A. Henderson and C. T. Imrie, *Liq. Cryst.*, 2011, **38**, 1407–1414.

5 L. Beguin, J. W. Emsley, M. Lelli, A. Lesage, G. R. Luckhurst, B. A. Timimi and H. Zimmermann, *J. Phys. Chem. B*, 2012, **116**, 7940–7951.

6 J. Chravolin and B. Deloche, in *The Molecular Physics of Liquid Crystals*, ed. G. R. Luckhurst and G. W. Gray, Academic Press, 1979, ch. 15.

7 C. A. Veracini, *Nuclear Magnetic Resonance of Liquid Crystals*, ed. J. W. Emsley, Kluwer, Dordrecht, 1985, ch. 5.

8 P. Lesot and J. Courtieu, *Prog. Nucl. Mag. Res. Sp.*, 2009, **55**, 128-159.

9 D. Merlet, J. W. Emsley, P. Lesot and J. Courtieu, *J. Chem.Phys.*, 1999, **111**, 6890–6896.

10 J. W. Emsley, P. Lesot, J. Courtieu and D. Merlet, *Phys. Chem. Chem. Phys.*, 2004, **6**, 5331-5337.

11 A. Ferrarini, G. J. Moro, P. L. Nordio and G. R. Luckhurst, *Mol. Phys.*, 1992, **77**, 1-15.

12 M. P. Johansson, J. Olsen, *J. Chem. Theory Comput.*, 2008, **4**, 1460-1471.

13 G. Cinacchi, G. Prampolini, *J. Phys. Chem. A*, 2003, **107**, 5228-5232.

14 M. J. Frisch *et al.*, Gaussian 09 (Revision B.01), Gaussian, Inc., Wallingford CT, 2010.

15 S. Halbert, C. Clavaguéra, G. Bouchoux, *J. Comput. Chem.*, 2011, **32**, 1550-1560.

16 J. B. Klauda, R. W. Pastor, B. R. Brooks, *J. Phys. Chem. B*, 2005, **109**, 15684-15686.

17 C. Zannoni, in *The Molecular Physics of Liquid Crystals*, ed. G. R. Luckhurst and G. W. Gray, Academic Press, 1979, ch. 3.

18 C. Meyer, G. R. Luckhurst and I. Dozov, *Phys. Rev. Lett.*, 2013, **111**, 067801.

19 C. Meyer, G. R. Luckhurst and I. Dozov, *J. Mater. Chem. C*, 2015, **3**, 318-328.

20 D. Chen, J. H. Porada, J. B. Hooper, A. Klittnick, Y. Shen, M. R. Tuchband, E. Korblova, D. Bedrov, D. M. Walba, M. A. Glaser, J. E. Maclennan and N. A. Clark, *Proc. Natl. Acad. Sci. U.S.A.*, 2013, **110**, 15931–15936.

21 J. W. Emsley, P. Lesot, G. R. Luckhurst, A. Meddour and D. Merlet, *Phys. Rev. E*, 2013, **87**, 040501(R).

22 J. Thisayukta, H. Niwano, H. Takezoe and J. Watanabe, *J. Am. Chem. Soc.*, 2002, **124**, 3354–3358.

23 D. J. Earl, M. A. Osipov, H. Takezoe, Y. Takanishi and M. R. Wilson, *Phys. Rev. E*, 2005, **71**, 021706.

24 V. Görtz and J. W. Goodby, *Chem. Commun.*, 2005, 3262–3264; V. Görtz, C. Southern, N. W. Roberts, H. F. Gleeson and J. W. Goodby, *Soft Matter*, 2009, **5**, 463–471.

25 R. A. Reddy and C. Tschierske, *J. Mater. Chem.*, 2006, **16**, 907-961.

26 R. Basu, J. S. Pendery, R. G. Petschek, R. P. Lemieux and C. Rosenblatt, *Phys. Rev. Lett.*, 2011, **107**, 237804.

27 R. Berger, J. Courtieu, R. R. Gil, C. Griesinger, M. Köck, P. Lesot, B. Luy, D. Merlet, A. Navarro-Vázquez, M. Reggelin,U. M. Reinscheid, C. M. Thiele and M. Zweckstetter, *Angew. Chem., Int. Ed.*, 2012, **51**, 8388–8391.

Appendix A

Torsional Potentials from quantum mechanical calculations

Torsional potentials for the compounds investigated in this thesis were taken from the literature or computed by quantum mechanical DFT calculations, at various levels of theory [1]. The latter are reported below, grouped according to the chemical nature of the model compound to which they refer. All profiles were obtained by relaxed scan: at each scan point, all internal coordinates different from the dihedral of interest were optimized. In the plots below, symbols represent the quantum mechanical data and lines correspond to fitting of these data according to the expression reported in Eq. 5.20 of Chapter 5.

Alkyl chains

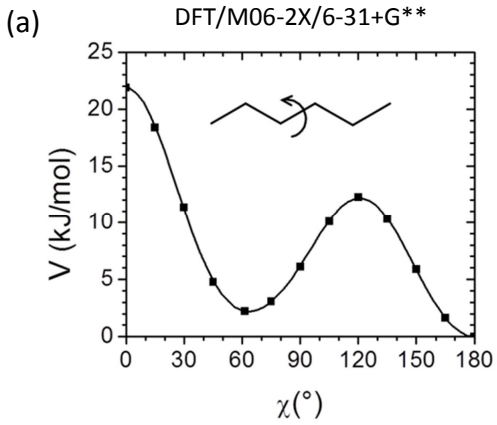

Figure A.1 Torsional potential (squares, DFT/M06-2X/6-31+G**) and fitting curve (line) for the central bond of hexane. The rotating dihedral is indicated by an arrow. The energy difference between *gauche* and *trans* states is ΔV_{gt} = +2.2 kJmol^{-1}.

Alkenyl chains

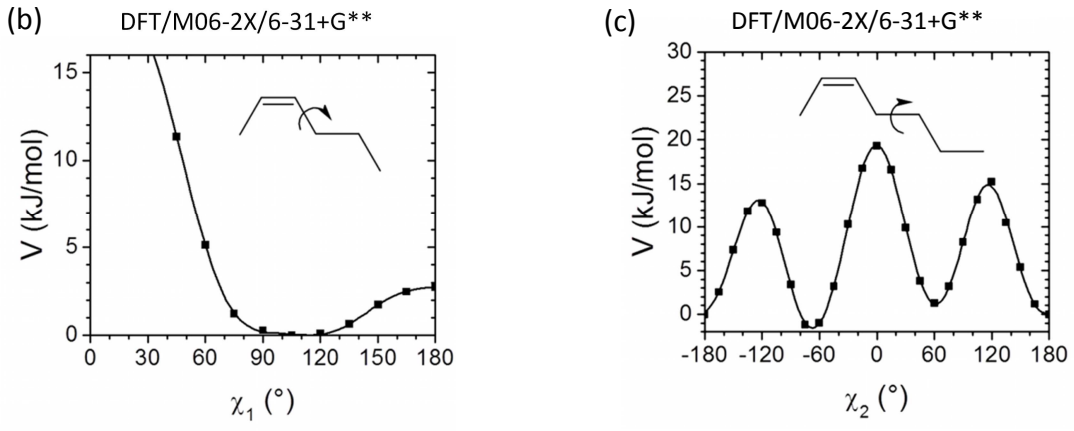

Figure A.2 Torsional potentials (squares, DFT/M06-2X/6-31+G**) and fitting curves (lines) for (b) *cis*-2-hexene, (c) *cis*-2-heptene. The rotating dihedrals are indicated by arrows. During the scan of χ_2 the dihedral angle χ_1 takes a value of ~ +105°; the energy difference between the *gauche*− and *trans* states is ΔV_{g-t} ~ −1.5 kJmol^{-1}, and that between the *gauche*+ and *trans* states is ΔV_{g+t} ~ +1.2 kJmol$^{-1.}$

Alkylbenzenes

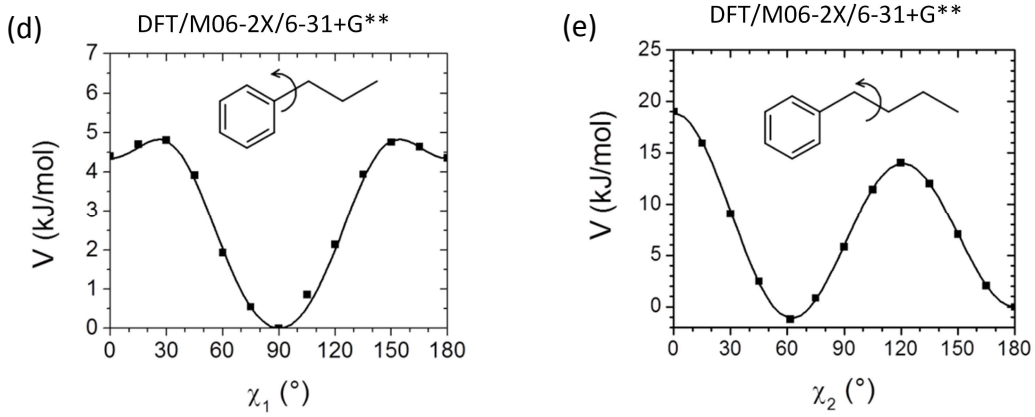

Figure A.3. Torsional potentials (squares, DFT/M06-2X/6-31+G**) and fitting curve (lines) for (d) propylbenzene, (e) butylbenzene. The rotating dihedrals are indicated by arrows. For χ_2 the energy difference between the *gauche* and *trans* states is ΔV_{gt} ~ −1.1 kJmol^{-1}.

Phenyl esters

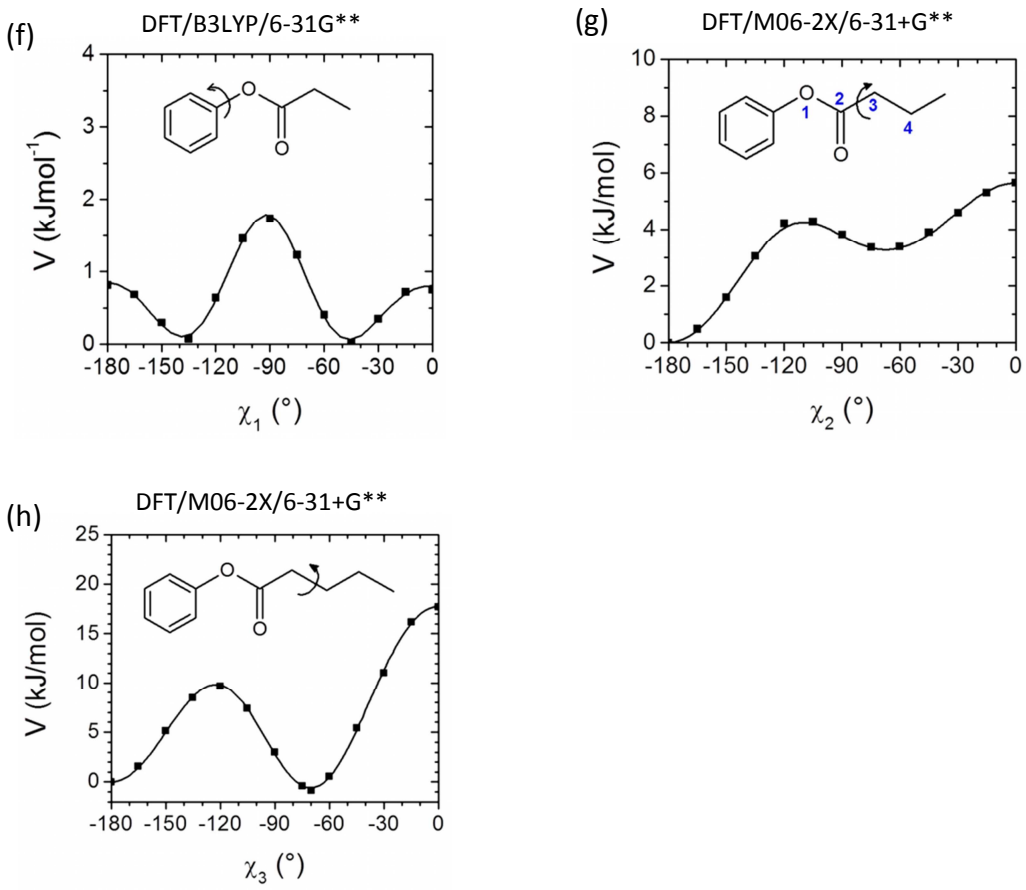

Figure A.4. Torsional potentials (squares, DFT/B3LYP/6-31G** for χ_1 and DFT/M06-2X/6-31+G** for χ_2 and χ_3) and fitting curves (lines) for (f) phenyl propanoate, (g) phenyl butanoate, (h) phenyl pentanoate. The rotating dihedrals are indicated by arrows and by atom numbering when needed. For χ_3 the energy difference between the *gauche* and *trans* states is $\Delta V_{gt} \sim -0.8$ kJmol^{-1}.

Phenyl Benzoates

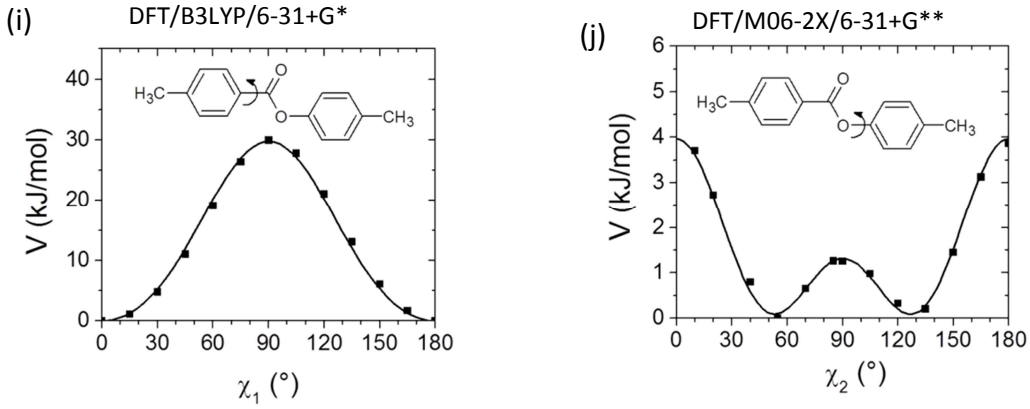

Figure A.5. Torsional potentials (squares, DFT/B3LYP/6-31+G* for χ_1 and DFT/M06-2X/6-31+G** for χ_2) and fitting curves (lines) for 4-methylphenyl 4-methylbenzoate.The rotating dihedrals are indicated by arrows.

Phenyl Fluorobenzoates

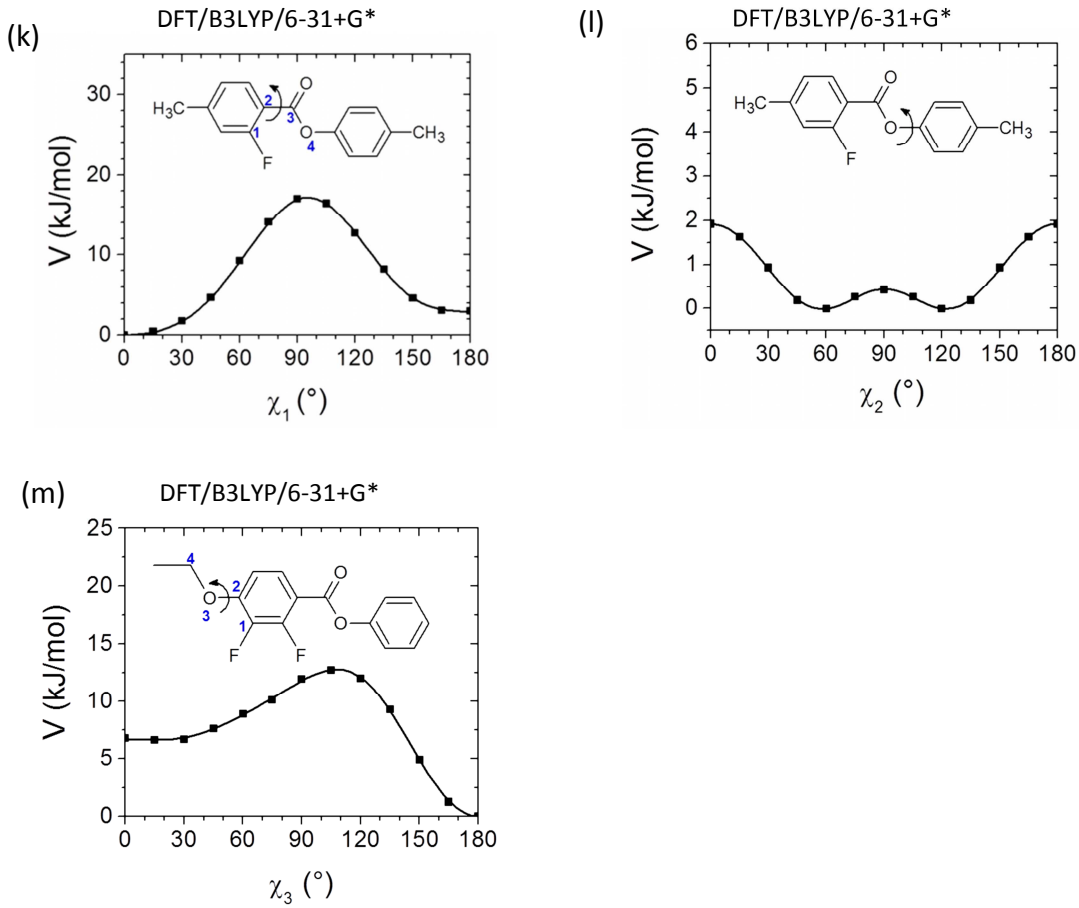

Figure A.6. Torsional potentials (squares**,** DFT/B3LYP/6-31+G*) and fitting curves (lines) for (k,l) 4-methylphenyl 2-fluoro-4-methylbenzoate, (m) phenyl 2,3-difluoro-4-ethoxybenzoate. The rotating dihedrals are indicated by arrows and by atom numbering when needed. During the torsional scan of χ_2 and χ_3, the dihedral angle χ_1 takes a value of ~ 0°.

Benzilideneanilines

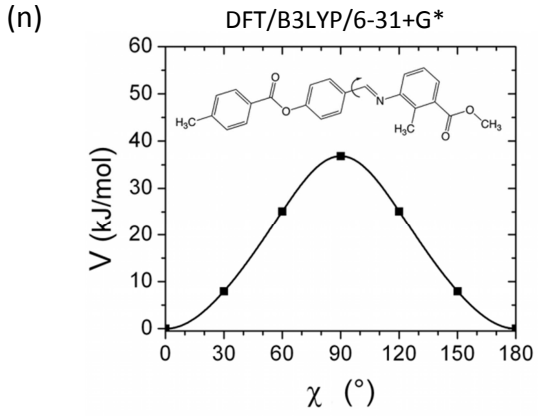

Figure A.7. Torsional potentials (squares, DFT/B3LYP/6-31+G*) and fitting curve (line) for a derivative of benzilideneaniline. The rotating dihedral is indicated by an arrow.

Azobenzenes

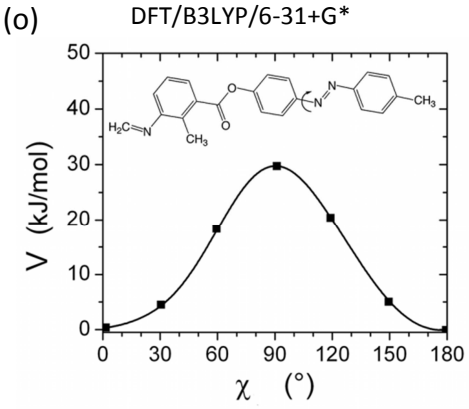

Figure A.8. Torsional potentials (squares, DFT/B3LYP/6-31+G*) and fitting curve (line) for a derivative of azobenzene. The rotating dihedral is indicated by an arrow. Quantum mechanical data were kindly provided by Dr. A. Marini, University of Pisa.

References

1 Gaussian 09, Revision B.01. M. J. Frish, G. W. Trucks, H. B. Schlegel, G. E. Scuseria, M. A. Robb, J. R. Cheeseman, G. Scalmani, V. Barone, B. Mennucci, G. A. Petersson, H. Nakatsuji, M. Caricato, X. Li, H. P. Hratchian, A. F. Izmaylov, J. Bloino, G. Zheng, J. L. Sonnenberg, M. Hada, M. Ehara, K. Toyota, R. Fukuda, J. Hasegawa, M. Ishida, T. Nakajima, Y. Honda, O. Kitao, H. Nakai, T. Vreven, J. A. Montgomery, Jr., J. E. Peralta, F. Ogliaro, M. Bearpark, J. J. Heyd, E. Brothers, K. N. Kudin, V. N. Staroverov, R. Kobayashi, J. Normand, K. Raghavachari, A. Rendell, J. C. Burant, S. S. Iyengar, J. Tomasi, M. Cossi, N. Rega, J. M. Millam, M. Klene, J. E. Knox, J. B. Cross, V. Bakken, C. Adamo, J. Jaramillo, R. Gomperts, R. E. Stratmann, O. Yazyev, A. J. Austin, R. Cammi, C. Pomelli, J. W. Ochterski, R. L. Martin, K. Morokuma, V. G. Zakrzewski, G. A. Voth, P. Salvador, J. J. Dannenberg, S. Dapprich, A. D. Daniels, Ö. Farkas, J. B. Foresman, J. V. Ortiz, J. Cioslowski and D. J. Fox, Gaussian, Inc., Wallingford CT, 2009.

Conclusions

In this thesis the behaviour of liquid crystals of bent-shaped molecules has been investigated using theoretical and computational methods. Two kinds of problems have been addressed: (***i***) phase behaviour, with focus on the recently discovered twist-bend nematic (N_{TB}) phase; (***ii***) material properties, with focus on elastic and flexoelectric properties in the nematic (N) phase.

(***i***) Using different theoretical and computational methods we could obtain major insights into the molecular origin and the structure of the N_{TB} phase, addressing the validity of various controversial hypotheses proposed in the literature.

To investigate the molecular origin of the N_{TB} phase, we developed a generalized Maier–Saupe theory for apolar V-shaped particles (Chapter 3) and performed some preliminary Molecular Dynamics (MD) simulations of rigid, achiral, apolar, purely repulsive bent-shaped particles (Chapter 4). The existence of a nematic (N) to N_{TB} phase transition is clearly evidenced by the generalized Maier-Saupe model. The results of the MD simulations are also in line with the formation of a twist-bend nematic organization. These findings show that the key molecular feature at the origin of the N_{TB} phase is the bent molecular shape, and that flexoelectric coupling and conformational chirality are not essential.

Using the generalized Maier-Saupe model, we examined particles with different molecular bend angle, and showed that the phase behaviour is extremely sensitive to this molecular parameter, with the N_{TB}-N phase transition occurring only for a limited range of bend angle values. This result allowed us to elucidate the experimentally observed sensitivity of the N_{TB} phase formation to changes in the molecular structure. The model also allowed us to make some general predictions about the elastic behaviour and to clarify the relationship between the formation of the N_{TB} phase and the elastic properties of the nematic phase, showing that the N-N_{TB} transition is accompanied by softening of the bend elastic mode in the N phase.

An interesting result of the MD simulations is the formation of a N_{TB} organization in a system of “hard” particles. Experimentally the twist-bend phase has been observed in

thermotropic liquid crystals: it would be of interest to check whether bent-shaped colloids can also exhibit this organization.

The generalized Maier-Saupe model also provided important information on the characteristic structural parameters (pitch p and conical angle θ_0) of the N_{TB} phase and their temperature dependence. Remarkably, a pitch of the order of just a few molecular lengths was predicted, in agreement with the experimental evidences.

Quantitative estimates of the pitch and conical angle starting from the chemical structure were obtained from the analysis of the experimental ^{2}H-NMR splittings, using a model that combines an atomistic representation of molecules with a molecular field description of the orientational distribution in the N_{TB} phase (Chapter 9). In this study we also discussed the origin of the strong enantiotopic discrimination observed in the N_{TB} phase. Our results indicate that this is not related to presence of chiral molecular conformations, but it is a direct consequence of the high chirality of the N_{TB} environment, resulting from its extremely small pitch.

(*ii*) An Integrated Methodology was set up (by combining DFT calculations, Monte Carlo conformational sampling, and a molecular field model with atomistic resolution, Chapter 5) to predict a variety of properties of nematic liquid crystals starting from the molecular level. In particular we focussed on the elastic and flexoelectric properties of bent-core compounds and liquid crystals dimers. Collaboration with experimental groups allowed us to validate the methodology on a large number of systems with different molecular structures. Very good agreement was obtained between our predictions and the experimental findings, showing the sensitivity of our methodology to details of the chemical structure and thus its usefulness as a tool for materials design for applications. The variety of chemical structures investigated allowed us to build a library of molecular parameters (geometry, torsional potential, atomic charges) for the most common mesogenic groups, which can be reused and incremented in the future.

Modelling allowed us to identify the molecular origin of the small bend elastic constant K_{33} exhibited by nematics of bent-shaped molecules and also to explain apparent exceptions to this behaviour.

We showed that the main molecular parameter governing the elastic behaviour of bent-core compounds is the core bend angle (Chapters 6 and 7). Low values of K_{33} and

weakly dependent on the order parameter are obtained for sufficiently small values of the bend angle, such as in the case oxadiazole derivatives; when the bend angle is larger, as in thiadiazole derivatives, the conventional behaviour of rod-like liquid crystals (high K_{33}, increasing with increasing order) is recovered.

The molecular curvature was found to be crucial also for the elastic properties of liquid crystals dimers (Chapter 8). In these systems, definition of the bend angle, taken as the angle between the terminal mesogenic units, is not as straightforward as in bent-core compounds: because of the conformational flexibility of the spacer, the bend angle is characterized by a distribution of values. We showed that the bend angle distribution exhibits a subtle dependence on the chemical structure, being in particular sensitive to the nature of the linking group connecting the mesogenic units and the spacer. Even small changes in the bend angle distribution were found to have a dramatic effect on the bend elastic constants K_{33}: according to the values and trend with the order parameter of K_{33}, three kinds of elastic behaviours could be distinguished. In Type I behaviour, K_{33} is low and decreases with increasing order; in Type II behaviour, K_{33} is low and almost independent of order; in Type III behaviour, K_{33} is high and increases with increasing order, as in conventional rod-like nematics. Finally, combining these results with our generalized Maier-Saupe model for the N_{TB}-N phase transition, we could discuss the influence of the linking group on the occurrence of the N_{TB} phase in liquid crystals dimers.

The results presented here for the flexoelectric properties are especially important: because of the experimental difficulties and the limits of simple models developed for rigid, idealized particles, the molecular determinants of the flexoelectric effect in liquid crystals still remain poorly understood. Our methodology allowed us to obtain quantitative estimates of the flexoelectric coefficients, and to distinguish their dipolar and contribution, which proved useful to connect the flexoelectric behaviour to the molecular structure. In this way we could identify some general features in the flexoelectric properties of bent-core compounds, offering new insights into the origin of the experimentally observed behaviour and allowing a molecular-based understanding of flexolectricity, which is very important for exploitation of this phenomenon.

Based on the results obtained in this thesis, we envisage the following developments.

First it would be important to extend the Molecular Dynamics simulations performed here to particles with a different bent shape (such as particles with different bend angles, or with conformationally flexibility), to further characterize the effect of the molecular features on the phase organization. A topic of major interest which could be investigated by MD simulations is the effect of the bent shape on the dynamical properties.

The second perspective regards the investigation of modulated liquid crystal phases by molecular field models. In particular the work presented here for the twist-bend organization could be extended to explore the stability and structure of phases with 2D or 3D director modulations. This would be particularly interesting in view of the difficulties of molecular simulations in handling non-uniform systems.

For what regards the material properties, extension of the modelling activity to other systems, combined with new experimental measurements, could be helpful to further characterize the behaviour of bent-shaped mesogens, in particular with respect to their flexoelectric properties.

Acknowledgments

During my PhD studies I had the pleasure to collaborate with many people: all of them gave an important contribution to this work, and I am truly grateful for that.

First, I would like to thank all people from Merck Chemicals for the opportunity to work together, for believing in our collaboration and also for the free moments spent together. I really had a good time.

I am grateful to Prof. Helen Gleeson and Dr. Sarabjot Kaur for sharing with me their experimental studies on elasticity and flexoelectricity in bent-core systems, and for their enthusiasm in our collaboration.

I would also like to thank Dr. Alberto Marini for his contributions to the study of A131.

A special thank goes to Prof. Geoffrey Luckhurst, whose contribution has been invaluable. He's one of the nicest and most clever people I've ever met, and I will always recall with pleasure the stimulating discussions we had together.